Chem Soc Rev

REVIEW ARTICLE

View Article Online
View Journal | View Issue

Cite this: *Chem. Soc. Rev.*, 2024, **53**, 11462

Nano-rods in Ni-rich layered cathodes for practical batteries

Geon-Tae Park, †[a] Nam-Yung Park,†[a] Hoon-Hee Ryu, †‡[a] H. Hohyun Sun,[b] Jang-Yeon Hwang [ac] and Yang-Kook Sun *[ac]

Lithium transition metal oxide layers, $Li[Ni_{1-x-y}Co_x(Mn\ and/or\ Al)_y]O_2$, are widely used and mass-produced for current rechargeable battery cathodes. Development of cathode materials has focused on increasing the Ni content by simply controlling the chemical composition, but as the Ni content has almost reached its limit, a new breakthrough is required. In this regard, microstructural modification is rapidly emerging as a prospective approach, namely in the production of nano-rod layered cathode materials. A comprehensive review of the physicochemical properties and electrochemical performances of cathodes bearing the nano-rod microstructure is provided herein. A detailed discussion is regarding the structural stability of the cathode, which should be maximized to suppress microcrack formation, the main cause of capacity fading in Ni-rich cathode materials. In addition, the morphological features required to achieve optimal performance are examined. Following a discussion of the initial nano-rod cathodes, which were based on compositional concentration gradients, the preparation of nano-rod cathodes without the inclusion of a concentration gradient is reviewed, highlighting the importance of the precursor. Subsequently, the challenges and advances associated with the nano-rod structure are discussed, including considerations for synthesizing nano-rod cathodes and surface shielding of the nano-rod structure. It goes on to cover nano-rod cathode materials for next-generation batteries (*e.g.*, all-solid-state, lithium-metal, and sodium-ion batteries), inspiring the battery community and other materials scientists looking for clues to the solution of the challenges that they encounter.

Received 6th June 2024

DOI: 10.1039/d3cs01110k

rsc.li/chem-soc-rev

[a] *Department of Energy Engineering, Hanyang University, Seoul, 04763, South Korea. E-mail: yksun@hanyang.ac.kr*
[b] *Department of Chemical and Biological Engineering, The University of Alabama, Alabama 35487, USA*
[c] *Department of Battery Engineering, Hanyang University, Seoul, 04763, South Korea*
† These authors contributed equally to this work.
‡ Present address: Department of Chemical Engineering and Applied Chemistry, Chungnam National University, Daejeon, 34134, South Korea.

Geon-Tae Park

Geon-Tae Park received his PhD degree from Hanyang University in South Korea. He is currently a post-doctoral researcher in the Department of Energy Engineering at Hanyang University. His research interests are developing advanced cathode materials for lithium-ion and next-generation batteries.

Nam-Yung Park

Nam-Yung Park received his PhD degree from Hanyang University in South Korea. He is currently a postdoctoral researcher in the Department of Energy Engineering at Hanyang University. His research focuses on cathode materials for Li-ion batteries and all-solid-state batteries.

1. Introduction

1.1. Developing trends for cathodes in industry

Since their debut in the consumer market by Sony in 1991, lithium-ion batteries (LIBs) have become one of the primary choices for energy storage, evolving from powering small portable electronics to fueling electric vehicles (EVs).[1–4] Of the four major components present in LIBs, the cathode stands out as the costliest and heaviest component, exerting a significant impact on both the cost and performance aspects of LIBs.[5–7] Consequently, the development of superior cathode materials has consistently been pivotal for the advancement of LIBs since their introduction.

In the academic field, various types of cathode materials have been proposed over recent decades, although only a few have been commercially adopted since the initial commercialization of the $LiCoO_2$ (LCO) cathode material.[8–19] Even among these, the spinel-structured $LiMn_2O_4$, which does not offer significant performance advantages, is rarely used, and the layered $Li[Ni_{1-x-y-z}Co_x(Mn_y \text{ or } Al_z)]O_2$ (NCM, NCA, and/or NCMA) cathode materials and olivine-structured $LiFePO_4$ cathode materials dominate the current cathode market share.[20–22] New materials are constantly being researched and developed as candidates for next-generation cathode materials, with the ultimate goals of commercialization and deployment. Examples include Li-rich cathode materials and disordered rock-salt (DRX) cathode materials, which are considered to have significant potential for complementing the drawbacks associated with current NCM/NCA and LFP cathode materials while reducing their dependence on specific resources.[23,24] However, the ability of these materials to reach the commercialization stage remains uncertain.

Layered NCM/NCA cathode materials have significant advantages in that their performances and stabilities can be easily modified by simply changing their compositional chemistries.[6,25,26] The NCM333 cathode material was one of

Hoon-Hee Ryu

Hoon-Hee Ryu is currently an assistant professor in Department of Chemical Engineering and Applied Chemistry at Chungnam National University. He received his PhD from the Hanyang University in 2022. Afterwards, he joined the Lawrence Berkeley National Laboratory as a postdoctoral researcher. His research interests are developing novel cathode materials for next-generation batteries.

H. Hohyun Sun

H. Hohyun Sun is currently an assistant professor in the Department of Chemical and Biological Engineering at the University of Alabama. He received his BS from Northwestern University in 2015 and his PhD from the University of Texas at Austin in 2020, with both degrees in chemical engineering. Afterwards, he joined the Army Research Laboratory as a Harry Diamond Distinguished Postdoctoral Fellow where he studied energy materials. His research interest is at the intersection of chemical engineering and materials science with a focus on battery materials as a medium to establish a renewable energy landscape.

Jang-Yeon Hwang

Jang-Yeon Hwang received his PhD degree (2018) at the Hanyang University in South Korea. He is an Associate Professor in the Department of Energy Engineering & Battery Engineering at the Hanyang University. His research is focused on the development of novel electrode materials for the high-energy alkali-ion and alkali-metal batteries.

Yang-Kook Sun

Yang-Kook Sun received his PhD degree from Seoul National University, Korea. He has worked at the Hanyang University in Korea as a professor since 2000. His research interests are the synthesis of new battery materials for lithium-ion batteries, Na-ion batteries, Li–S batteries, and all-solid-state batteries. His innovative concentration gradient cathode materials for lithium-ion batteries have been commercialized since 2009 and have been used in electric vehicles such as Kia's NIRO EV (2018), Hyundai's KONA EV for Europe (2020), and Ford's F-150 Lightning (2022).

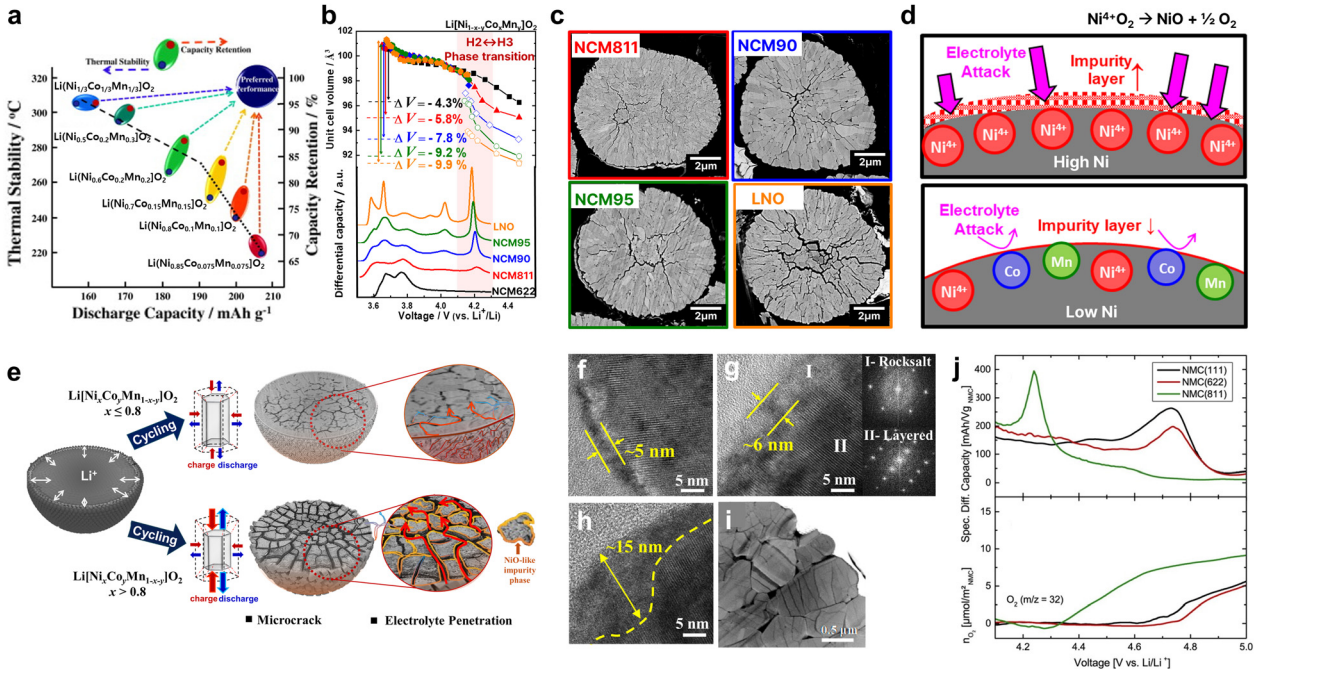

Fig. 1 (a) Map showing the relationship between the discharge capacity, thermal stability, and capacity retention in Li/Li[$Ni_xCo_yMn_{1-x-y}$]O_2 (x = 1/3, 0.5, 0.6, 0.7, 0.8, and 0.85). (b) Unit cell volume changes and dQ dV^{-1} curves for NCM622, NCM811, NCM90, NCM95 and LNO cathodes upon charging. (c) Cross-sectional SEM images of NCM811, NCM90, NCM95 and LNO cathodes charged to 4.3 V. (d) Schematic illustration of surface reaction between cathode and electrolyte for cathodes with high and low Ni content. (e) Capacity fading scheme of Ni-rich Li[$Ni_xCo_yMn_{1-x-y}$]O_2 cathodes. High-resolution TEM image of the discharged Li[$Ni_xCo_yMn_{1-x-y}$]O_2 cathode after 100 cycles, (f) x = 0.6 and (g) x = 0.8, with Fourier transforms from the marked regions of I and II, and (h) x = 0.95. (i) TEM image of the primary particles showing numerous intragranular cracks in the cycled Li[$Ni_{0.9}Co_{0.05}Mn_{0.05}$]$O_2$ cathode. (j) Specific differential capacity *vs.* cell voltage and evolution of O_2 as a function of the cell voltage for the NMC-Li cells. (a) is reproduced with permission,[31] Copyright 2013, Elsevier. (e)–(i) are reproduced with permission,[36] Copyright 2018, American Chemical Society. (j) is reproduced under Creative Commons CC-BY license,[37] Copyright 2017, IOP Publishing.

the first to appear in early applications, followed by the LCO cathode material, wherein the equal concentrations of the constituent elements ensured a balance between energy density, conductivity, stability, and cost.[27,28] This material was initially employed in hybrid EV batteries in 2009.[29] However, due to the rapidly increasing demand for higher energy densities, the NCM622 cathode material (containing 60% Ni) was commercialized in 2016.[30] Currently, the Ni contents of such materials have been increased to reach even 100% in some cases.[6,31,32] Although increasing Ni content is an effective strategy for increasing the energy density, inherent trade-off between capacity and stability leads to challenges in handling such materials owing to the high reactivity of Ni^{4+} (Fig. 1a).[31–35]

Particularly in Ni-rich cathodes above 80% Ni, the abrupt anisotropic lattice volume change that occurs at high state of charge (Fig. 1b) induces strain within the particles and leads to the formation of microcracks (Fig. 1c).[36,38,39] This can be attributed to mechanical stress generated during the charge/discharge process exceeding the tolerance of materials, leading to the development of physical fractures throughout individual particles. The fractures exponentially increase the cathode surface area exposed to the electrolyte to induce undesirable side reactions and associated rapid capacity fading.[40–44] At the cathode-electrolyte interface exposed to electrolyte, unstable Ni^{4+} ions undergo side reactions to degrade the layered cathode surface into a NiO-like rocksalt phase resulting in increased resistance and capacity fading (Fig. 1d). This degradation mechanism is limited to the surface in NCM/NCA cathodes with less than 80% Ni but amplifies to the bulk along interparticle boundaries in those with greater than 80% Ni (Fig. 1e). Note that the thickness of the impurity increases with increasing Ni content (Fig. 1f–h) and further extends. In addition to the microcracks observed along the interparticle boundaries, numerous intraparticle cracks generated by internal stress arising from the anisotropic volume change (Fig. 1i). This chemo-mechanical degradation not only impedes the facile (de)intercalation of Li^+ ions, but also promotes gas generation to jeopardize battery safety (Fig. 1j).[37] Naturally, both the scientific community and industry have devoted enormous efforts to overcoming this challenge, with doping and coating post-treatment methods being the most prevalent.

Among the various treatments reported to date, concentration gradient (CG) cathode materials are examples that have been successfully commercialized and applied in EVs.[45] It has been estimated that these materials will be produced by >45 kton per year after 2026, which could support the production of up to 225 000 EVs annually. The original concept of concentration gradient cathodes aimed to achieve a high-energy density from the Ni-enriched core simultaneously and an exceptional safety originating from the Mn-rich shell.[46,47]

Besides compositional protection, surprisingly, concentration gradient cathode materials possess a characteristic microstructure comprising elongated primary particles that are radially aligned outward.[46,48] This unique spatial configuration has been proven to be particularly effective in relieving the mechanical stress accumulated within the cathode particles, thereby effectively suppressing the formation of microcracks.[49] The synergistic effects of these features ultimately result in an excellent cycling ability and superior thermal stability, even in cathodes containing ≥90% Ni.[50] Consequently, this approach can be considered an optimal design strategy for extremely high-Ni cathode materials.

1.2. History of nano-rod cathodes

Unique cathode microsphere particles, whose microstructure consists of rod-shaped primary particles with radial alignment (hereafter referred to as nano-rods), were first observed in the CG Li[$Ni_{0.75}Co_{0.10}Mn_{0.15}$]$O_2$ cathode material by Sun *et al.* in 2012.[46] A follow-up study by Noh *et al.* in 2013[48] placed significant emphasis on the nano-rod structure present in a full-concentration gradient Li[$Ni_{0.60}Co_{0.15}Mn_{0.25}$]$O_2$ material, highlighting its contribution to several key performance aspects. Inspired by these characteristics, research has intensified in the context of microstructure engineering aimed at achieving elongated rod-shaped primary particles exhibiting radial alignment, even in the absence of concentration gradients. The first such report was published by Park *et al.*,[51] who demonstrated that boron doping can alter the shape of the primary particles. Following this study, various dopants were investigated for the development of nano-rod structures, and the number of related studies has rapidly increased in line with strong interest from both the academic and industrial fields.

Thus, this review evaluates and discusses the nano-rod microstructure's physicochemical properties and related electrochemical features (Fig. 2). In addition, this review introduces various concepts developed to overcome the challenges encountered in implementing nano-rods. It also explores the potential application of nano-rod cathode materials in next-generation secondary batteries, such as all-solid-state, Li-metal, and Na-ion batteries.

2. Physicochemical characteristics and electrochemical performances

2.1. Geometric characteristics

Traditionally, the microstructural features of layered-oxide cathode grains have been broadly classified into two categories, namely polygonal- and rod-shaped primary particles. Due to the absence of advanced characterization technologies in the early stages of the cathode development, specification of the microstructural features of nano-rod cathodes was limited. With the recent development of novel and superior analytical methods, various parameters have been proposed for distinguishing the morphological features of nano-rod particles, including the dimensions, population density, and degree of orientation. Representative morphologic parameters reported to date include the width, length, area, square root size, aspect ratio, number density, alignment angle, and surface faceting. This section introduces the various distinguishing microstructural characteristics of nano-rod cathodes and provides the respective numerical distribution ranges required to obtain outstanding electrochemical performances. In addition, the conditions responsible for altering these morphology determinants are briefly introduced, and the exceptional relationships between the microstructural parameters and the electrochemical performance are discussed.

2.1.1. Size factors. In many publications, the term "size" is used to represent a variety of parameters, including the

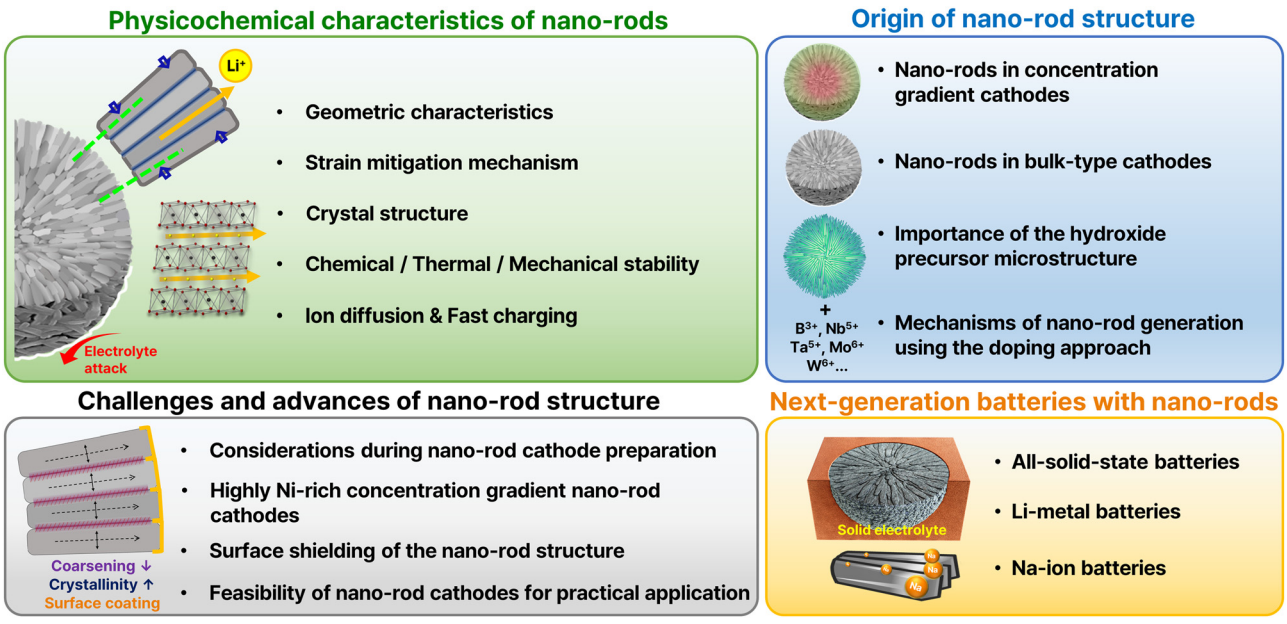

Fig. 2 Schematic illustration of the nano-rod cathode themes covered in this review.

width (nm), length (nm), area (nm^2), and square root size (nm). The width and length are defined as the transverse axis and the longitudinal axis of the nano-rod primary particle, respectively,[52–54] while the area refers to the grain area directly measured by a cathode particle's cross-section.[55] Thus, if the morphology of a nano-rod grain is close to a rectangular shape, the area can be calculated by multiplying the width by the length. In addition, the square root size corresponds to the square root of the grain area.[56,57] At the same time, and the number density is a parameter that indicates the number of primary particles within a cathode secondary particle.[55,58,59] Measuring such size factors can be easily achieved using image processing software, such as the ImageJ, CellProfiler, and MIPAR software packages.[60–62] However, obtaining a clean cross-section of the cathode material is necessary to measure these size factors accurately. For this purpose, a high-performance cross-section polisher or focused-ion beam should be employed. Furthermore, the electron backscatter diffraction (EBSD) technique is useful when measuring these size factors since it clearly distinguishes between the cathode grain boundaries.

Conventional layered-oxide cathodes consist of relatively thick, bulky, and irregular-shaped primary particles typical of ceramic materials.[63] In contrast, nano-rod cathodes feature a rod-like morphology characterized by a lengthy longitudinal axis and a narrow width.[46,64–66] In one study, Ryu *et al.*[66] measured the widths and lengths of the primary particles of the bulk-structured $Li[Ni_{0.901}Co_{0.044}Mn_{0.045}Al_{0.01}]O_2$ (BS-NCMA89) and the hybrid-structured $Li[Ni_{0.899}Co_{0.045}Mn_{0.046}Al_{0.01}]O_2$ (HS-NCMA89) (Fig. 3a). They reported average widths of 371 and 158 nm for the BS-NCMA89 and HS-NCMA89 materials, respectively, and average lengths of 587 and 630 nm, respectively. The adoption of compositional partitioning in the NCMA90 cathode produced tightly packed nano-rod primary particles in HS-NCMA89, which are both long and narrow. Heteroelemental doping can also be used to tune the widths and lengths of the primary particles, wherein the introduction of B, Al, Ti, Mn, Sn, Zr, Te, Nb, W, Ta, Mo, and Sb provides narrower and longer primary particles.[53,67–96] It should be noted here that the chemical composition of the cathode does not limit such size modification effects, with size engineering effects also being confirmed in NCA85, NCA88, NCM90, NM90, and LNO materials. Studies have also demonstrated that the width of the primary particles is unequivocally correlated with the electrochemical cycling stability of the cathode material. For example, Park *et al.*[79] demonstrated an approximately linear relationship between the primary particle width and the capacity retention of $Li[Ni_{0.95}Co_{0.04}X_{0.01}]O_2$ (X = dopant) cathode (Fig. 3b). More specifically, the capacity retention increased with a reduced particle width, thereby suggesting that the chemistry of the dopant has a relatively small effect on the cycling performance, which appears to be primarily governed by the mechanical properties of the cathode. A notable feature of the grain size is that the distribution range of the particle width in conventional cathodes is broader than in nano-rod cathodes. For example, the width of the NCA89 particles ranges from 150 to 300 nm, whereas that of the W-NCA89 particles ranges from 50 to 100 nm.[97] The same trend has also been observed in other studies.[66,68,76] As will be discussed in the following section, the microstructure of the cathode active material is principally determined by its hydroxide precursor and the subsequent calcination conditions. More specifically, during high-temperature calcination, the high thermal energy input leads to coarsening of the primary particles, ultimately determining the cathode's microstructure. Since grain agglomeration mainly occurs between the lateral sides of adjacent primary particles, where the contact area between grains is large, the random coarsening of conventional primary particles yields an irregular width distribution.[98] In contrast, introducing a concentration gradient or hetero-elemental doping mitigates vigorous sintering of the primary particles, thereby producing tightly packed nano-rod grains with a uniform width distribution. This difference can ultimately affect the microstructural stability of the cathode, thereby defining its mechanical and electrochemical properties, as discussed later.

Although the area, square root size, and number density are different ways the grain size can be expressed, their intrinsic meanings are similar. As described above, the square root size corresponds to the square root of the grain area. Therefore, the two factors have the same physical meaning. In addition, since the number density is calculated by the number of grains per unit area, a decrease in the square root size indicates an increase in the number density. In this context, Ju *et al.*[55] reported that increasing the oxygen partial pressure stimulated the formation of nano-rod primary particles, decreasing the average grain area and increasing the number density. More specifically, they reported the average grain areas of NCM90 and DS-NCM90 to be 0.243 and 0.065 μm^2, respectively, whereas their corresponding number densities were 4 and 16 ea μm^{-2}, respectively (Fig. 3c). This increase in the grain number density concomitantly led to an increase the density of the cathode active material due to a reduction in the pore volume. As shown in Fig. 3d, the total pore percentages in NCM90 and D5-NCM90 were 1.91 and 0.63%, respectively. As in the case of the grain size, the nano-rod grains exhibited a relatively uniform grain area distribution, with standard deviations of 0.220 and 0.063 μm^2 for the NCM90 and DS-NCM90 cathodes, respectively (Fig. 3e). The number density of the primary particle can be further refined by adopting a multi-stage engineering approach. For example, Park *et al.*[58] reported that the introduction of Ti during the synthesis of $Ni(OH)_2$, followed by the addition of excess Al doping during the calcination step produced nanosized primary particles with exceptionally high number densities, *i.e.*, 7.9, 13.4, 17.8, and 22.4 ea μm^{-2} for the LNO, Ti0.75-LNO, LNO-Al4, and NTA cathodes, respectively (Fig. 3f). Interestingly, correlations were found between the number density of the primary particles and several performance indicators. More specifically, an approximately linear relationship was observed between the areal fraction of microcracks and the number density of the primary particles, demonstrating the effectiveness of particle size refinement in suppressing microcrack formation and propagation (Fig. 3g). As a result, the cycling stability and rate characteristics were improved, and the cathode performance exhibited an approximate linear relationship with the particle number density

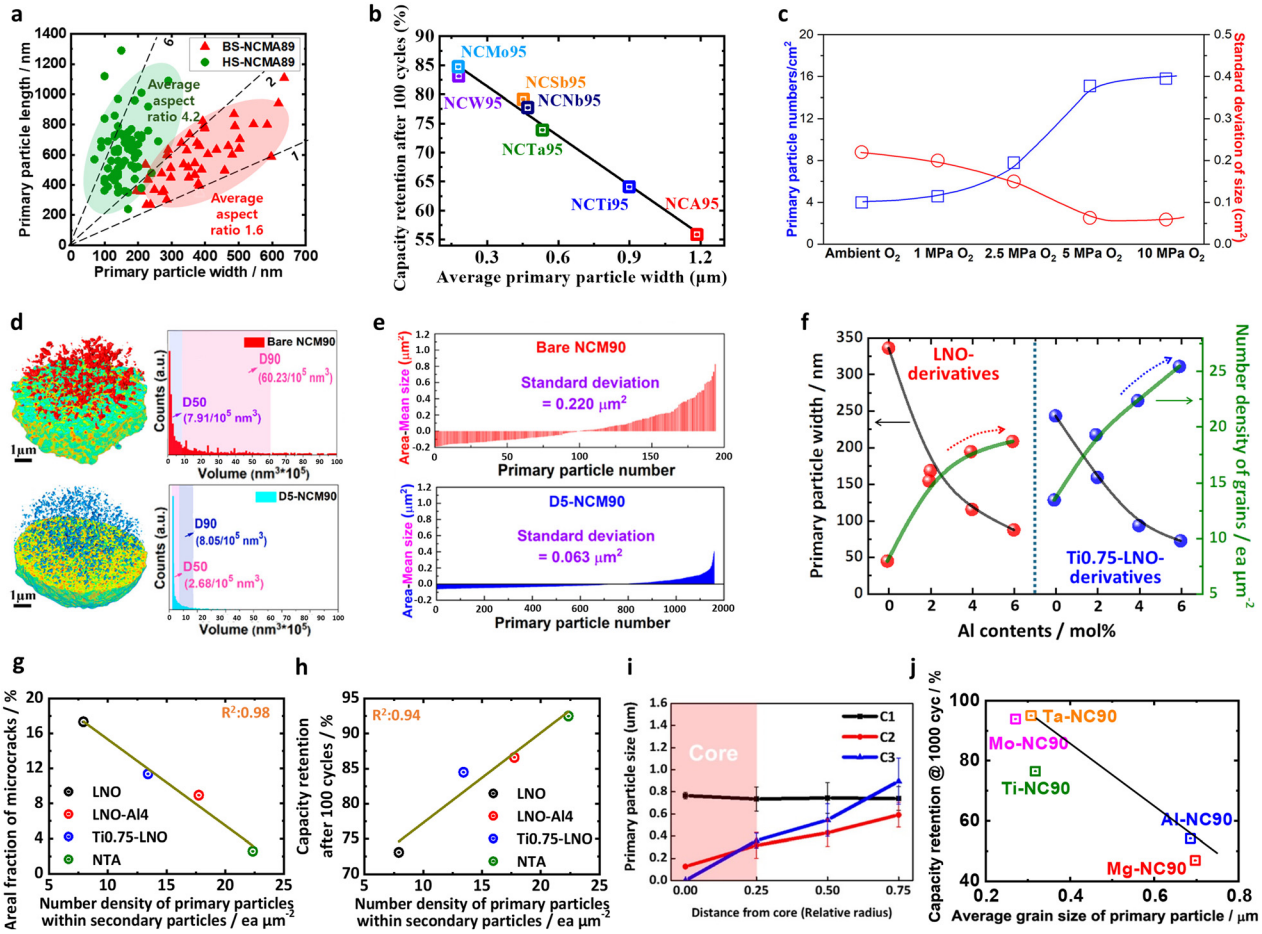

Fig. 3 (a) Quantitative comparisons of the microstructures of the BS-NCMA89 and HS-NCMA89 cathodes: primary particle widths and lengths. (b) Capacity retention after 100 cycles for cells featuring various cathodes lithiated at 800 °C, as a function of the average primary particle width, reflecting the relationship between the primary particle width and the cycle life. (c) Number of primary particles per μm^2 and standard deviation of the primary particle size for the bare NCM90 cathode materials sintered under O_2 at ambient pressure and 1–10 MPa. (d) 3D distributions and statistical analyses of the pore volumes of the bare NCM90 and D5-NCM90 cathode particles. (e) Standard deviations of the sizes of the bare NCM90 and D5-NCM90 cathode materials. (f) Plots of the primary particle widths and the grain number densities of the LNO- and Ti0.75-LNO-derivative cathodes as functions of the Al doping contents. Linear regression plots between the number density of the primary particles and (g) the areal fraction of microcracks after 100 cycles and (h) the capacity retention after 100 cycles. (i) Plot showing the change in the primary particle size measured as a function of the relative radius [from the center (0) to the radius (*R*)]. (j) Summaries of the capacity retention values after 1000 cycles as a function of the average grain size of the primary particles. (a) is reproduced with permission,[99] Copyright 2020, American Chemical Society. (b) is reproduced with permission,[79] Copyright 2021, Royal Society of Chemistry. (c)–(e) are reproduced with permission,[55] Copyright 2023, American Chemical Society. (f)–(h) are reproduced with permission,[58] Copyright 2023, Elsevier. (i) is reproduced with permission,[56] Copyright 2019, American Chemical Society. (j) is reproduced under Creative Commons CC-BY license,[57] Copyright 2021, The Authors, Springer Nature.

(Fig. 3h). In the context of layered-oxide cathodes, the preparation of such an ultrafine-grained cathode is not a trivial matter. Because the conventional method for synthesizing cathodes involves the preparation of a hydroxide precursor and subsequent lithiation at high temperatures (>700 °C), the primary particles of the hydroxide precursor invariably coarsen such that the grain size of the final cathode active material routinely exceeds 500 nm. In addition, Shim *et al.*[56] measured the locally varying square root size of the hollow-structured nano-rod NCM622 and reported that the size increases from the core to the shell of the cathode (*i.e.*, 0.25 μm near the center and 0.8 μm at the surface; Fig. 3i). This remarkable decrease in the square root size of the nano-rods was also observed by Sun *et al.*[57] More specifically, by doping high-valence elements, the square root size of the peripheral grains decreased to the ultrafine scale (<500 nm), *i.e.*, 308 and 271 nm for Ta-NC90 and Mo-NC90, respectively, thereby highlighting the effectiveness of high-valence ion doping in reducing the grain size (Fig. 3j).

2.1.2. Orientation angle. A series of phase map analyses can determine the crystal orientation angle of the nano-rod primary particles. For example, Skvortsova *et al.*[100] employed EBSD and folded inverse pole figure maps to demonstrate the strongly textured primary particles in B-doped NCM811. Each color of the segmented particles of different orientation colors represents a specific crystallographic direction in the hexagonal unit cell with a certain [*hkl*] (Fig. 4a). The nano-rods in the B-doped NCM811 were found to be mainly aligned to the [0001] direction, in contrast to the pristine NCM811 cathode,

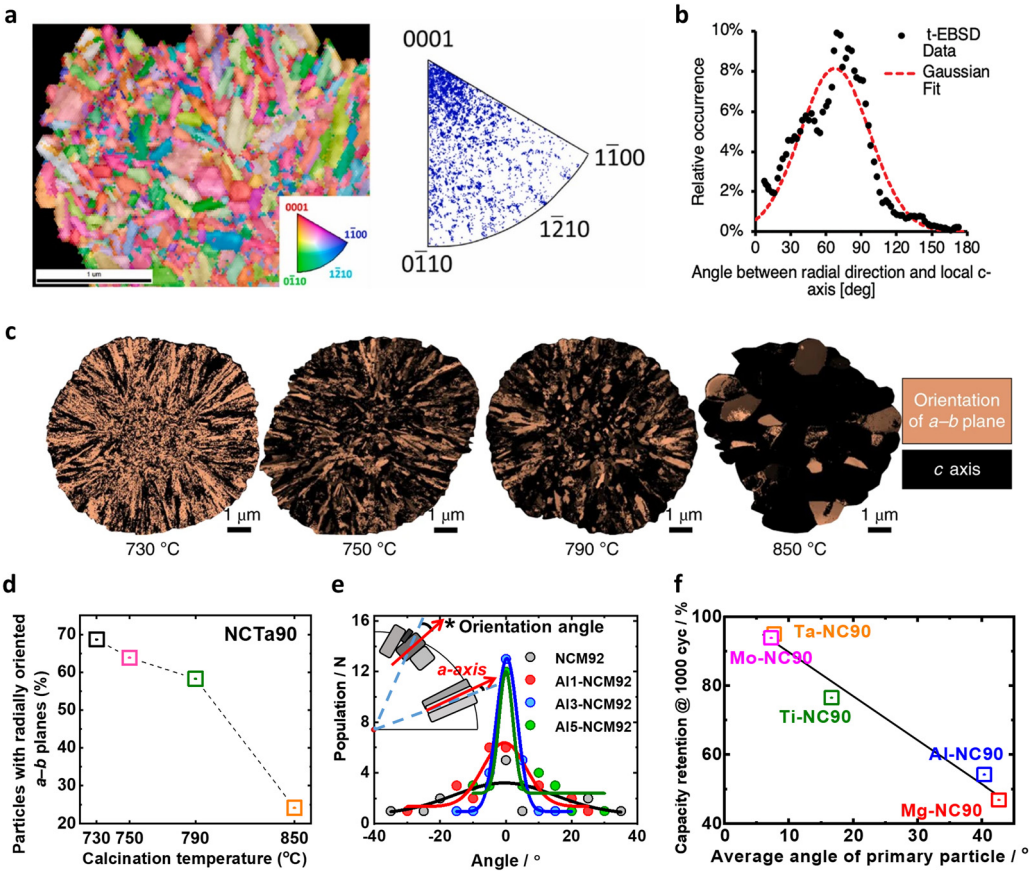

Fig. 4 (a) Surface normal-projected orientation t-EBSD maps of the CP_2B_5ex species. Lamellas with the corresponding color-coded inverse pole legends are shown, which correspond to a hexagonal unit cell, and indicate the specific crystallographic orientation for each grain color. The folded inverse pole figure discrete maps show the orientation of the surface normal for all measured grains in each sample. (b) Distribution of angles between the *c*-axis of the hexagonal primary particle lattice in the particle shell and the particle radial direction. Red: Gaussian fit. (c) ASTAR images of the NCTa90 cathodes highlighting the tendency of the *a*–*b* planes of the primary particles to point to the radial direction as the lithiation temperature is lowered. (d) Estimated percentage of primary particles with *a*–*b* planes pointing in the radial direction for NCTa90. (e) Orientation angles of the primary particles of the NCM92 (grey), Al1-NCM92 (red), Al3-NCM92 (blue), and Al5-NCM92 (green) particles. (f) Summary of the capacity retention values after 1000 cycles as a function of the average angle of the primary particles. (a) is reproduced with permission,[100] Copyright 2020, Royal Society of Chemistry. (b) is reproduced with permission,[101] Copyright 2023, Elsevier. (c) and (d) are reproduced with permission,[53] Copyright 2020, The Authors, Springer Nature. (e) is reproduced with permission,[106] Copyright 2023, Elsevier. (f) is reproduced under Creative Commons CC-BY license,[57] Copyright 2021, The Authors, Springer Nature.

suggesting rearrangement of the nano-rod grain orientation. Quantification of the grain orientation of the nano-rod NCM811 was performed by Brandt *et al.*[101] They reported that the transmission EBSD (t-EBSD) map with color-coded Euler angles was normalized concerning the statistical frequency of angle occurrence within a sphere, and the resulting quantitative plot matched well with the Gaussian fit (Fig. 4b). In addition, elongated, radially oriented grains were observed at the particle surface, while smaller and randomly aligned grains were found in the particle center.[101,102] In another study, Jung *et al.*[69,103] adopted ASTAR (automatic crystal orientation and phase mapping analysis for transmission electron microscopy, TEM) to map the crystal orientations of the primary particles. Most P-LNCM and B-LNCM primary particles exhibited similar crystallographic orientations, whereas the U-LNCM primary particles demonstrated a randomly distributed color index, indicating irregular orientation of the primary particles. A quantitative assessment of the radial texture of the NCTa90 cathode as a function of the calcination temperatures showed that a major portion of the nano-rod particles was radially oriented, with longitudinal axes parallel to the *a* direction (Fig. 4c).[53] However, upon increasing the calcination temperature, gradual weakening of the crystallographic texture was observed at higher lithiation temperatures (Fig. 4d). This change in the radial orientation of the primary particles results from coarsening caused by energy-induced grain rotation during high-temperature calcination.[104,105] Most frequently, the crystallographic orientation of primary particles can be directly measured by the angle between the longitudinal axis (parallel to the *a*-axis) of a primary particle and the diametric line passing through the center of the secondary particle. The angular distribution for the Al3- and Al5-NCM92 ranged from −10 to 10°, unlike the primary particles of NCM92, which exhibited no preferred orientation (Fig. 4e).[106] If the primary particles are randomly oriented, the orientation angle distribution is expected to range from 0 to 90° broadly. In comparison,

if the nano-rods are radially aligned, the angle should be close to 0°. Low relative primary particle angles are strongly related to a high capacity retention, giving an R^2 (coefficient of determination) value close to 0.98 (Fig. 4f).[57] By reshaping the primary particles into radially aligned rod- or needle-like grains, the strain during electrochemical cycling can be homogeneously distributed to inhibit microcracking, thereby improving the cycle life.[107] In addition, because the Li^+ and transition metal (TM) layer planes of the layered oxide cathode are parallel to the longitudinal axes of its primary particles, the formation of such radially aligned nano-rod primary particles can expedite Li migration during electrochemical (dis)charging.[52]

2.1.3. Shape-distinguishing factors. Depending on its longitudinal axis and thickness, the primary particle's geometric aspect ratio (expressed by the length divided by the width) can be determined. In most cases, the aspect ratios of the conventional NCM and NCA cathode materials are close to 1–2.[76,108,109] In this context, Park *et al.*[79] investigated the variation of anisotropy in the cathode primary particle as a function of the calcination time. The aspect ratio of the hydroxide precursor before calcination was approximately 5; however, the equaxiality of the NCA95 cathode continually increased during calcination, reaching 1.9 and 1.5 after 10 and 20 h of calcination, respectively (Fig. 5a). In addition, for the same calcination

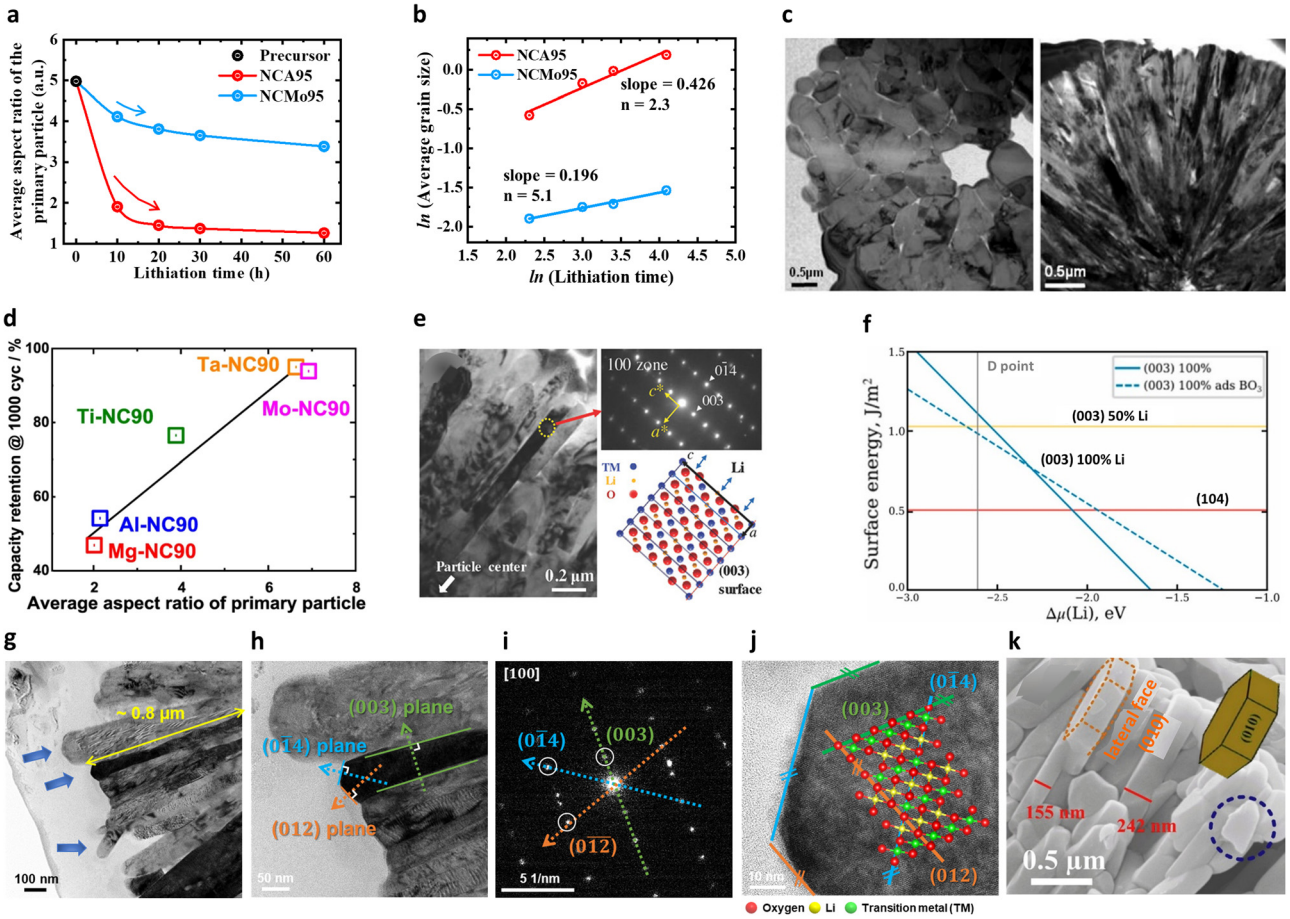

Fig. 5 (a) Average primary particle aspect ratios (expressed as length/width) of the hydroxide precursor, NCA95 cathode, and NCMo95 cathode particles as a function of the lithiation time. (b) Grain growth exponents for the NCA95 and NCMo95 cathodes calculated using the grain growth equation. (c) Cross-sectional TEM images of the cathode particles: (left) fixed composition of $Li[Ni_{0.5}Co_{0.2}Mn_{0.3}]O_2$ without the compositional gradient, and (right) FCG cathode wherein the core composition of $Li[Ni_{0.86}Co_{0.07}Mn_{0.07}]O_2$ is continuously varied to $Li[Ni_{0.67}Co_{0.09}Mn_{0.24}]O_2$ at the surface. (d) Summary of the capacity retention values after 1000 cycles as a function of the average primary particle aspect ratio. (e) Magnified TEM image of the B1.0-NCM90 primary particles, electron diffraction pattern of the region marked by a yellow circle, and schematic drawing of the crystal structure of the oriented primary particle. (f) Surface energy as a function of the Li chemical potential $\Delta\mu$(Li) at a fixed $\Delta\mu$(O) = −1.06 eV. The (104) and (003) surfaces with 50/100% Li and the (003) surface with the adsorption of a single BO_3 group are shown. The vertical gray line corresponds to the Li chemical potential at point *D*. (g) Bright-field cross-sectional scanning STEM images of the 4% Mn-doped CG NCA92 cathode primary particles. Blue arrows highlight the surface shapes of the primary particles. (h) High-magnification TEM images of the 4% Mn-doped CG NCA92 cathode primary particles. (i) SAED and (j) HRTEM images of the 4% Mn-doped CG NCA92 cathode obtained from the grains identified in part (h). (k) SEM image of the NCA-Urea-NMP specimen. (a) and (b) are reproduced under Creative Commons CC-BY license,[79] Copyright 2021, Royal Society of Chemistry. (c) is reproduced with permission,[48] Copyright 2013, American Chemical Society. (d) is reproduced under Creative Commons CC-BY license,[57] Copyright 2021, Springer Nature. (e) is reproduced with permission,[51] Copyright 2018, John Wiley and Sons. (f) is reproduced with permission,[100] Copyright 2023, Elsevier. (g)–(j) are reproduced with permission,[72] Copyright 2024, John Wiley and Sons. (k) is reproduced with permission,[115] Copyright 2020, Elsevier.

time, the anisotropy of the hydroxide precursor remained relatively unchanged in the presence of Mo. Furthermore, the NCMo95 cathode calcined for 10 and 60 h exhibited aspect ratios of 4.1 and 3.4, demonstrating the different grain growth mechanisms between the NCA95 and NCMo95 cathodes. Generally, grain growth depends solely on the curvature of the particle boundary, and no hindrance force arises from the secondary particles or solutes. This leads to a grain growth exponent (n) close to 2 and the formation of equiaxed primary particles (Fig. 5b).[110,111] However, the n value for NCMo95 was closer to 5, suggesting that particle growth is effectively inhibited by external drag forces, forming nano-rods with high aspect ratios.[112,113] The construction of such an elongated nano-rod primary particle promotes tight packing of the cathode particle, reducing the pore volume and increasing the particle density (Fig. 5c).[48,114] The aspect ratios of nano-rod primary particles are also known to depend on the doping element. For example, Sun *et al.*[57] reported that dopants with high oxidation states are prone to produce elongated grains; Al-NC90, Ti-NC90, Ta-NC90, and Mo-NC90 exhibited geometric aspect ratios of 2.1, 3.9, 6.6, and 6.9, respectively. Although a higher aspect ratio improved electrochemical cycling stability at the cathode (Fig. 5d), B doping produced the most elongated nano-rod particles and did not produce a particularly high cycling performance.[53] Furthermore, despite the low oxidation state of Al, the incorporation of excess Al (*i.e.*, >3 mol%) produced anisotropic primary particles, suggesting that both the choice of doping element and the doping amount are key to modifying the particle aspect ratio.[68]

In some cases, the addition of certain dopants can promote crystallographic facets on the surfaces of the nano-rod particles. For example, B is a well-known element that produces angular and highly faceted nano-rod primary particles. In this context, Park *et al.*[51] suggested that introducing B doping into the NCM90 cathode could potentially construct flat hexagonal-like primary particles, wherein most of the surface was enclosed at the sides by the (003) plane (Fig. 5e). Boron significantly decreases the energy of the (003) surface, thereby leading to the anisotropic plate-like shape observed for the primary particles of the NCM cathode (Fig. 5f).[100] In the B-doped NCA89 cathode, such surface faceting was more pronounced. In another study, Ryu *et al.*[52] demonstrated that B doping not only attenuated the surface energy of the (003) plane but also those of the $(01\bar{2})$ and (014) planes. The sides of the B-NCA89 nano-rod particles developed zigzag surfaces so that the side surfaces were terminated with (003) and $(01\bar{2})$ planes. Such zigzag-like surfaces induced by crystallographic faceting was also confirmed in the B-NCA95 cathode.[116] Recently, Park *et al.*[72] demonstrated that adding Mn during calcination could stimulate nano-scale surface faceting in the NCA cathode. This was accounted for by considering that the near-surface introduction of Mn spatially refined the microstructure by capping the nano-rod particles with the (003), $(0\bar{1}4)$, and (012) crystal planes (Fig. 5g–j). Notably, such nano-scale surface faceting is not observed in general NCM cathodes that use a hydroxide precursor to which Mn is added during the co-precipitation step, thereby confirming that subsurface Mn doping is key to attenuating the cathode surface energy. Although the degree of surface faceting is not as pronounced as that observed upon B or Mn doping, the cathodes prepared using NMP or PVP as a capping agent also demonstrated enhance exposure of the (010) planes (Fig. 5k).[115,117] Since the (003) facets parallel to the Li^+ and TM layers are more resistant to irreversible structural degradation than the non-(003) facets, highly faceted nano-rod primary particles contribute to improving the electrochemical cycling stability of the cathode.[66]

2.2. Strain mitigation mechanism

The degradation of Ni-rich cathodes is largely caused by the high proportion of labile Ni^{4+} species combined with the mechanical instability originating from intergranular crack formation.[36,118,119] One of the beneficial effects of constructing nano-rod primary particles is that the cathode can mitigate any degradation arising from the microcracks. The following subsections discuss the various microcrack mitigation mechanisms associated with nano-rod primary particles. In addition to theoretical calculations, experimental demonstrations of the mechanical stabilities of the nano-rod particles under different states of charge (SoC) are also presented.

2.2.1. Computational simulations. The strain relaxation mechanism of the nano-rod-grained cathode has been theoretically demonstrated using a range of computational simulations. For example, finite element modeling (FEM) elucidated the different spatial distributions of the tensile and compressive stresses within the cathode particles according to the different microstructures and SoC.[52,120–122] Fig. 6a and b compare the FEM results obtained for the P-NCA89 and B-NCA88 cathodes, which feature randomly oriented polygonal-shaped grains and highly textured rod-like grains, respectively.[52] Since the difference between the crystallographic strains along the a- and c-axes becomes more severe as the SoC increases, the magnitude associated with the computed spatial stress distribution continually increased up to x = 0.6 in $Li_{1-x}TMO_2$ for both the P-NCA89 and B-NCA88 cathodes. However, different crystallographic orientations between the P-NCA89 and B-NCA88 particles led to dissimilar behavior in terms of the stress distribution. It was demonstrated that the tensile and compressive stress were concentrated at the center and the shell region of the B-NCA88 cathode, respectively, whereas those of the P-NCA89 were irregularly dispersed throughout each cathode particle. During delithiation, the radially aligned grains at the particle surfaces contracted consistently, providing a uniform compressive stress distribution along the particle surface region, thereby mitigating microcrack propagation.[109,123] However, the randomly oriented grains in the P-NCA89 cathode led to irregular distributions of the tensile and compressive stresses throughout each cathode particle, thereby promoting microcrack growth and plastic deformation in most regions of the material. The balance between the hoop and radial stresses in the nano-rod-grained cathode can also explain the microcrack suppression mechanism of the cathode. More specifically, the lattice parameter variation along the c-axis of the nano-rod grains led to the generation of compressive hoop stress at the

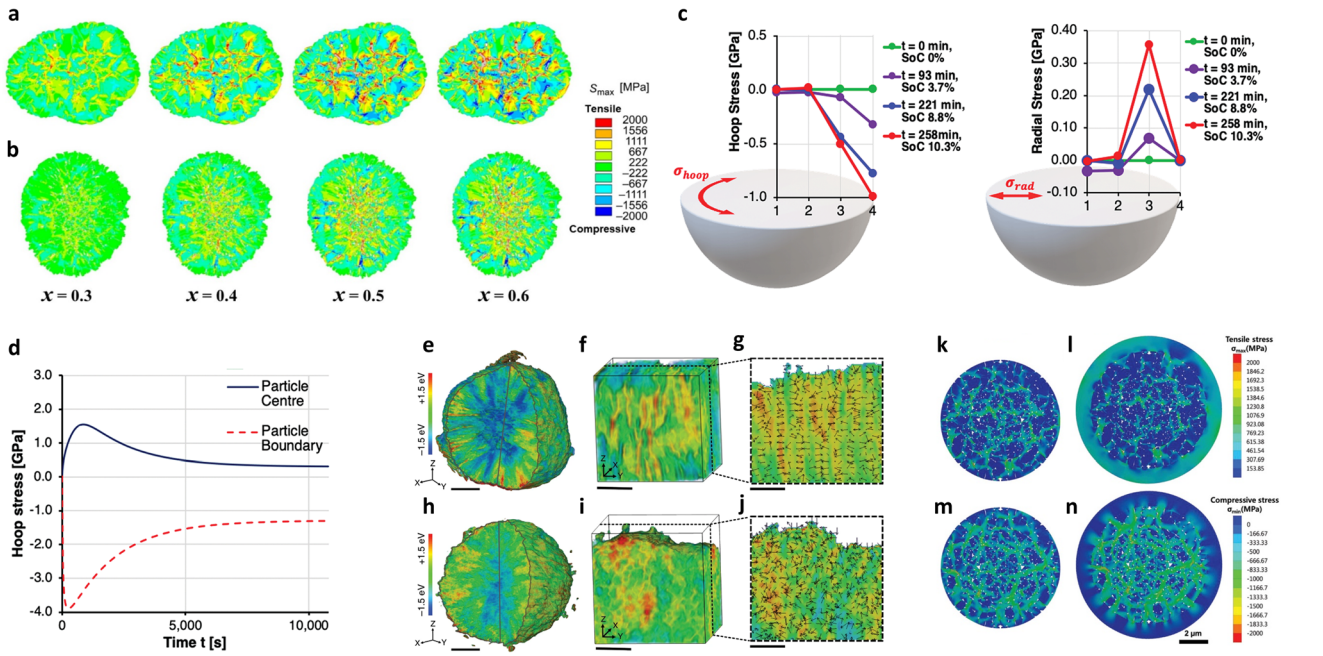

Fig. 6 Calculated stress distribution (maximum principal stress) as a function of the state of charge inside the (a) P-NCA89 and (b) B-NCA88 particles. (c) Reconstructed stress state along the particle radius *vs.* time and SoC; hoop stress and radial stress. (d) Simulated hoop stress evolution *versus* time during charging in the core and shell of a secondary particle. (e) 3D Ni valence state distribution, (f) representative region of the 3D Ni valence state distribution, and (g) 2D nanodomain valence gradient of the rod-NMC. (h) 3D Ni valence state distribution, (i) representative region of the 3D Ni valence state distribution, and (j) 2D nanodomain valence gradient of the gravel-NMC. The nanodomain valence gradient vectors are represented by black arrows, wherein the vector direction and magnitude are represented by the arrow direction and arrow length, respectively. The scale bars in parts (e) and (h) are 3 μm, while the scale bars in parts (f,g) and (i,j) are 1 μm. The Ni K-edge absorption energies are color-coded, in which blue stands for a lower edge energy and red reflects a higher edge energy. Tensile stress distributions (maximum principal stress) for the (k) CC90 and (l) CSG90 particles, along with the compressive stress distributions (minimum principal stress) for the (m) CC90 and (n) CSG90 particles in the fully charged state. (a) and (b) are reproduced with permission,[52] Copyright 2020, Elsevier. (c) and (d) are reproduced under Creative Commons CC-BY license,[101] Copyright 2020, Royal Society of Chemistry. (e)–(j) are reproduced under Creative Commons CC-BY license,[122] Copyright 2020, The Authors, Springer Nature. (k)–(n) are reproduced with permission,[49] Copyright 2019, John Wiley and Sons.

particle shell region, while the central grains generated tensile stress in the radial direction (Fig. 6c).[101] As shown in Fig. 6d, the simultaneous generation of peak compressive hoop stress in the particle shell and peak tensile stress in the particle core was observed. As the tensile stress tends to promote the nucleation of intergranular cracks and the compressive stress tends to suppress the opening of grain borders, the peripheral nano-rod grains featuring a high concentration of compressive stress can mitigate microcrack propagation. Another suggested mechanism for the microstrain alleviation effect observed in the nano-rod-grained cathodes is the charge distribution homogeneity. For example, Xu *et al.*[122] statistically quantified the charge distribution of over 20 million nanodomains in the gravel-NMC (with randomly oriented grains) and rod-NMC (with radially aligned grains) cathodes. Owing to the radial alignment of the grains and the less tortuous Li^+ pathways, the rod-NMC produced a relatively lower degree of charge heterogeneity than the gravel-NMC, generating a lower internal stress between the adjacent grains and enhancing the electrochemical performance of the cathode (Fig. 6e–j). It was also found that incorporating a concentration gradient into nano-rod-grained cathodes provided additional sturdiness for alleviating microcrack propagation. The particle interior of the Ni-rich cathode experienced compressive stress, while the outer layer containing a lower Ni content experienced tensile stress (Fig. 6k–n).[49,99] These differential stress states ultimately toughen the particle against microcrack propagation.

2.2.2. Experimental investigations. The microcrack mitigation effects of nano-rod primary particles were initially demonstrated experimentally upon variation in the concentration gradient of the nano-rod grains. After 100 cycles, the cathode without a concentration gradient underwent severe particle cracking, rupturing the spherical morphology of the cathode active material. In contrast, the NCMA85 particles with a two-sloped full concentration gradient (TSFCG) remained intact following the same cycle sequence (Fig. 7a–d).[124] However, because the chemical composition at the surface of the TSFCG NCMA85 was $Li[Ni_{0.79}Co_{0.05}Mn_{0.15}Al_{0.01}]O_2$, wherein the Ni fraction was relatively lower than that at the center, the crack alleviation effect attributed to a different chemical composition could not be ruled out. Park *et al.*[51] demonstrated that nano-rod particles without a concentration gradient could also decrease microcrack formation in a Ni-rich cathode. Although microcracks mainly form in the center of a particle,[125–128] the directionally confined nano-rod grains present in B1.0-NCM90 were able to avoid the microcrack development induced by an anisotropic volume change. In contrast, the undoped NCM90

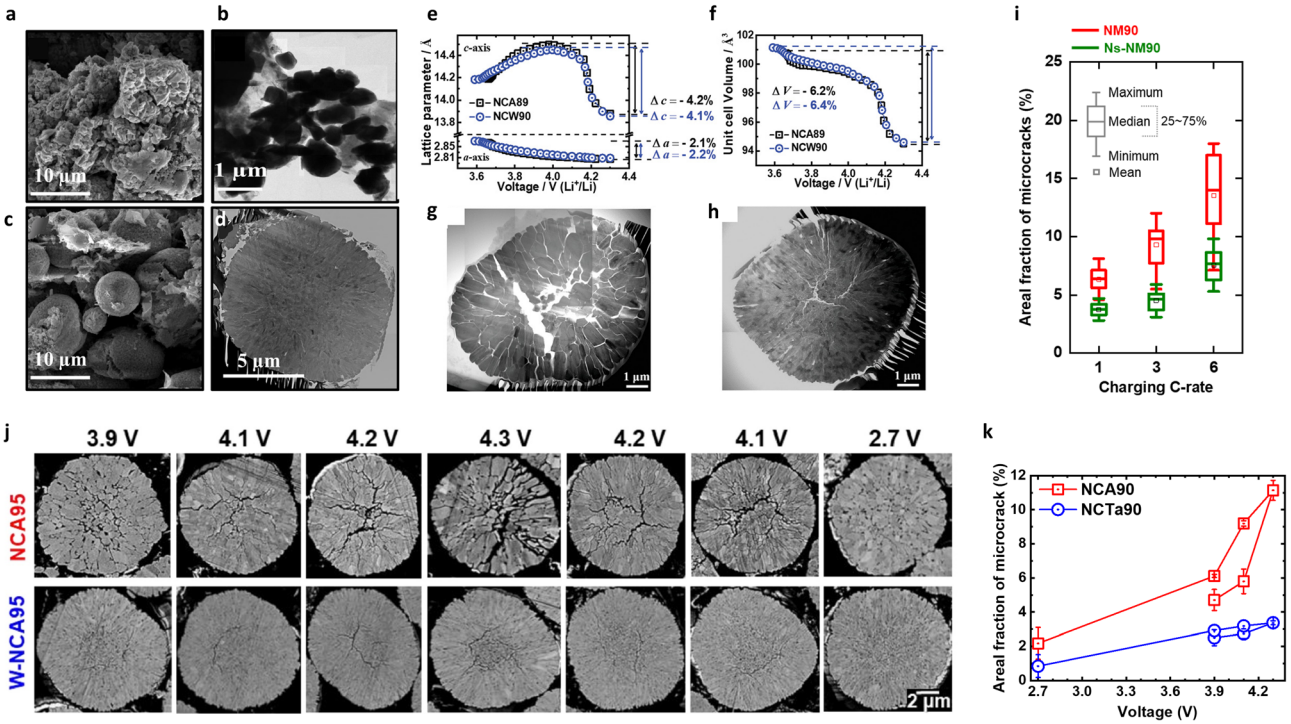

Fig. 7 (a) SEM image and (b) TEM image of the $Li[Ni_{0.85}Co_{0.11}Al_{0.04}]O_2$ NCA electrode after 100 cycles with an upper cut-off voltage of 4.5 V. (c) SEM image and (d) TEM images in the [100] zone of the $Li[Ni_{0.84}Co_{0.06}Mn_{0.09}Al_{0.01}]O_2$ TSFCG-Al electrode after 100 cycles with an upper cut-off voltage of 4.5 V. Changes in (e) the *a*- and *c*-axes lattice parameters and (f) the unit cell volumes for NCA89 and NCW90 as a function of the cell voltage. Bright-field STEM mosaic image of cross-sections of the (g) NCA89 and (h) NCW90 cathodes charged to 4.3 V. (i) Areal fractions of microcracks in the cathode secondary particles as a function of the charge C-rate determined from cross-sectional SEM images. The bars represent the distribution of results. (j) Comparison of the cross-sectional SEM images of the NCA95 and W-NCA95 cathodes in various charged and discharged states (charged to 3.9, 4.1, 4.2, and 4.3 V; discharged to 4.2, 4.1, and 2.7 V in the 1st cycle). (k) Areal fractions of the microcracks in the NCA90 and NCTa90 cathodes as a function of the cut-off voltage. (a)–(d) are reproduced with permission,[124] Copyright 2016, American Chemical Society. (e)–(h) are reproduced under Creative Commons CC-BY license,[129] Copyright 2019, The Authors, John Wiley and Sons. (i) is reproduced with permission,[132] Copyright 2022, John Wiley and Sons. (j) is reproduced with permission,[97] Copyright 2020, Elsevier. (k) is reproduced with permission,[53] Copyright 2020, Springer Nature.

suffered from severe microcracks traversing the entire secondary particle. Notably, the magnitude of unit cell contraction during electrochemical delithiation did not change upon the formation of nano-rods (Fig. 7e and f).[129] Furthermore, it has been reported that grain size refinement helps negate the deleterious effect of the H2 → H3 phase transition during electrochemical charging, thereby significantly enhancing the mechanical properties of the cathode (Fig. 7g and h).[130] It is also known that increasing the charging C-rate can cause more irreversible particle cracking, which is one of the main causes of rapid capacity fading at high cycling rates (Fig. 7i).[131] For instance, Co-free NM90 charged at 3 and 6C contained microcracks that propagated along the interparticle boundaries and almost separated the primary particles into individual secondary particles.[132] This mechanical disintegration can be attributed to the accumulation of internal strain caused by the SoC heterogeneity or the spatial inhomogeneity in the Li concentration.[133–135] It was found that the nano-rod primary particles constituting the Ns-NM90 cathode were more effective in promoting the uniform de-intercalation of Li^+ than the randomly oriented grains, thereby alleviating microcrack propagation and performance deterioration even under high C-rate charging.[132] To investigate the ability of nano-rod grains to mitigate microcrack formation in more detail, the cross-sections of equiaxed and nano-rod cathodes were systematically compared by progressively increasing the charging cut-off voltage followed by a full discharge (Fig. 7j).[97] The microcracks began to develop close to the peak of the H2 → H3 phase transition and gradually closed again during discharge. The areal fractions of microcracks in the equiaxed cathodes during discharge were larger than those during charging at the same voltage (Fig. 7k),[53] suggesting that the microcracks do not reversibly close even after 1st cycle. The repetitive opening and closing of these intergranular cracks therefore gradually builds up a cathode–electrolyte decomposition layer, leading to capacity fading in the equiaxed primary particles.[119,136,137] In contrast, the extent of microcracking was significantly alleviated over the entire SoC ranges in the nano-rod cathode, demonstrating the superior mechanical stability of the radially oriented nano-rod primary particles.

2.3. Crystal structure & ordering

It is generally considered ideal that a layered oxide cathode consists of a rhombohedral crystal structure with the $R\bar{3}m$ space group and without impurity phases. However, in some cases, nano-rod primary particles contain crystal structural characteristics different from the layered structures that are typical of

equiaxed grains. The disordered rock-salt, spinel, cation-ordered, and twinned crystals are representative crystal structures in the nano-rod cathodes. These crystal structures are different from the impurity phases observed in cycled or damaged Ni-rich cathodes. The following subsections will address the origins of these unexpected nano-scale crystal structures and their roles in determining the electrochemical performances of the nano-rod cathodes.

2.3.1. Rock-salt and disordered spinel structures. Formation of the rock-salt structure in the nano-rod cathode was observed for the first time by Kim *et al.*,[138] who reported that the introduction of W doping into a $LiNiO_2$ (LNO) cathode produced a major hexagonal layered phase ($R\bar{3}m$) and a minor rock-salt phase ($Fm\bar{3}m$) (Fig. 8a). Structural analyses confirmed that the percentage of the rock-salt phase increased with the amount of W. Theoretical calculations suggested that these W-doped rock-salt surfaces are energetically favored over the bare rocksalt surfaces and the layered surfaces. It is generally accepted that the rock-salt phase is typically observed in cycled or damaged Ni-rich cathodes, wherein the electrochemical performance is extremely poor.[139–145] However, the cycling performance of the rock-salt-containing W-doped LNO was unexpectedly superior to that of the undoped LNO cathode (Fig. 8b). Although W doping slightly decreased the initial discharge capacity, the W-doped LNO cathode exhibited remarkable stabilization, reflected by impressive cycling stability. It was therefore considered that the rocksalt phase segregated at the cathode surface protected the cathode active material from detrimental reactions with the electrolyte species and enhanced the cycling stability of the cathode.[67,138] In contrast, the introduction of W doping in NCM cathodes led to a disordered spinel phase formation. More specifically, Park *et al.*[146] demonstrated that the addition of W into the NCM90 cathode produced a 20 nm-thick spinel phase on the surfaces of the nano-rod grains (Fig. 8c). Similarly, the introduction of 0.5 mol% W doping in NCM940501 produced $Fd\bar{3}m$ spinel structures.[71] Such disordered spinel phases are considered to be an intermediate state between the layered and rock-salt structures.[64] Owing to the high oxidation state of W^{6+}, the Ni^{3+} species present in the TM layer are likely to be reduced to Ni^{2+} for maintenance of the charge neutrality, thereby promoting the migration of Ni^{2+} into the Li slabs to generate a cation-disordered spinel structure. The spinel structure formed at the surface of the nano-rod cathode protects the particle from electrolyte attack, thereby minimizing the formation of the NiO-like impurity phase observed after electrochemical cycling of the unmodified cathode.[147] The fraction of the resulting cation-intermixed structure depends on the Li stoichiometry and the calcination temperature. In this context, Chen *et al.*[148] determined the relative fractions of the rock-salt and layered structures by systematically varying the nominal Li ratio during calcination. Consequently, small primary particles consisting of intergrown rock-salt and layered phases were formed in the Li-deficient cathode active materials. Increasing the Li ratio led

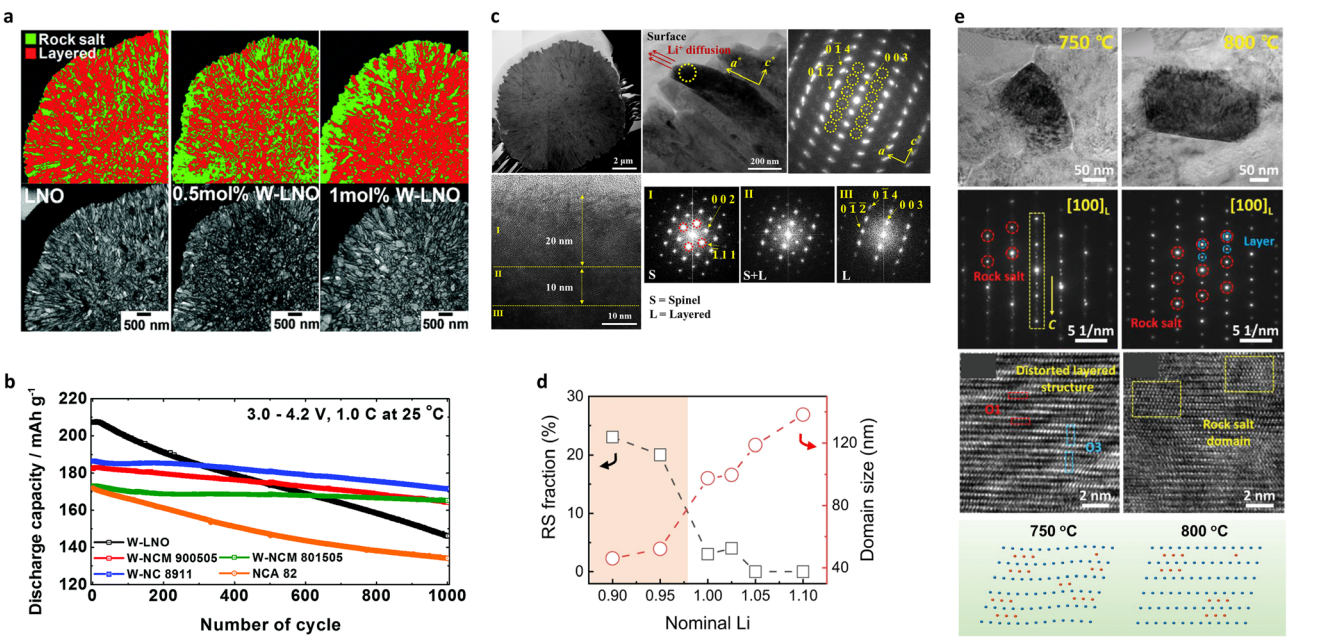

Fig. 8 (a) ASTAR TEM phase mapping and corresponding bright field images of the LNO, 0.5 mol% W-LNO, and 1 mol% W-LNO species, showing distribution of the rocksalt phases in the respective cathodes. (b) Long term cycling of the 1 mol% W-doped $Li[Ni_xCo_yMn_{1-x-y}]O_2$ cathodes (x = 0.8, 0.89, 0.9, and 1.0; y = 0.15, 0.11, 0.05, and 0) and the $Li[Ni_{0.82}Co_{0.14}Al_{0.04}]O_2$ cathode (NCA 82, commercial Ni rich benchmark cathode), tested using pouch cells at 1.0C (180 mA g^{-1}) and 25 °C within a voltage range of 3.0–4.2 V against graphite anodes. (c) Bright-field STEM, magnified TEM, SAED, HRTEM, and corresponding FT images of the W1.0-NCM90 cathode. (d) Calculated rock-salt phase fractions and domain sizes of the layered phase as a function of the nominal Li amount. (e) Low-magnification TEM, corresponding SAED, and HRTEM images, along with a schematic diagram of the microstructures of the NM85 cathodes synthesized at different temperatures. (a) and (b) are reproduced with permission,[138] Copyright 2018, Royal Society of Chemistry. (c) is reproduced with permission,[146] Copyright 2019, Elsevier. (d) is reproduced under Creative Commons CC-BY license,[148] Copyright 2024, Springer Nature. (e) is reproduced with permission,[150] Copyright 2022, John Wiley and Sons.

to a larger grain size but a decrease in the relative fraction of the rock-salt structure (Fig. 8d). It was found that the electrochemical performance of the 5% Li-deficient NM95 cathode featuring the layered-rock-salt composite structure was among the best in a series of Li-varying NM95 cathodes. Increasing the Li content and maximizing the calcination temperature increased the average crystallite size, signifying that mitigating crystal growth corresponds to a more disordered cation structure.[149] Similar findings were observed by Yu *et al.*,[150] who found that increasing the calcination temperature (*i.e.*, promoting crystallite growth) led to a reduction in the number of stacking faults (lattice bending and distortion) and in the rock-salt structure fraction while increasing the relative fraction of the layered structure (Fig. 8e). Considering the structural variation owing to hetero-elemental doping, the Li stoichiometry, and the calcination temperature, it is possible that methods to alleviate grain coarsening suppress crystallite growth, thereby promoting the formation of cation intermixed intermediate structures (*e.g.*, disordered spinel and rock-salt structures) prior to generating a perfect layered crystal structure through the formation of equiaxed primary particles.

2.3.2. Cation-ordered structure. In normal cases, site exchange between the Li^+ and TM species occurs randomly to produce rock-salt and disordered spinel structures, as described in the preceding subsection. However, in some cases, cations do not mix in a random manner but intermix in a regular pattern to produce periodical Li^+ occupation in the TM layer or TM ions in the Li^+ layer. In this context, Yoon *et al.*[77] demonstrated the formation of a cation-ordered phase in a Zr-doped nano-rod LNO cathode. A cation-ordered structure refers to the alternating occupation of Li^+ in the TM layer, which produces a regular oscillation in contrast to that of the TM layer since half of the TM ions in every second TM row are replaced by Li^+ (and *vice versa* in the Li layer) (Fig. 9a and b).[77,151,152]

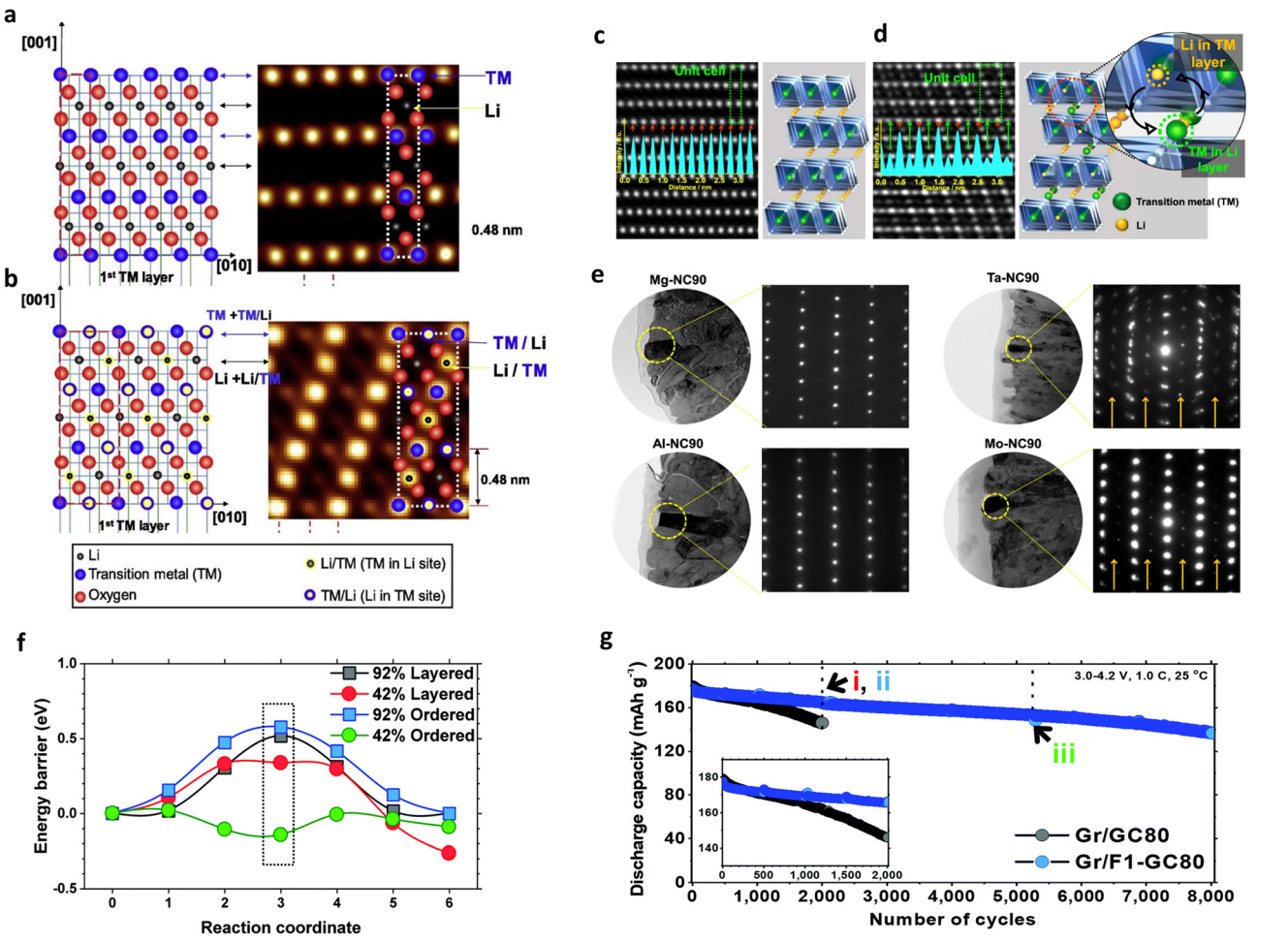

Fig. 9 Schematic diagrams and HAADF TEM images of the (a) normal and (b) cation-ordered (Li/TM) structures. HAADF TEM images and derived structural models of the (c) Al-NC90 and (d) Ta-NC90 cathodes. (e) Bright-field images and corresponding SAED patterns of single primary particles of the Mg-NC90, Al-NC90, Ta-NC90, and Mo-NC90 cathodes. (f) Li-ion diffusion between adjacent octahedral sites (reaction coordinates 0 and 6) in the layered and ordered polymorphs of Li_xNiO_2. The intermediate position (reaction coordinate 3) is the tetrahedral site representing the energetic barrier in all compositions except the delithiated ordered composition. (g) Long term cycling performances of the GC80 and F1-GC80 cathodes using pouch-type full cells at 25 °C. (a) and (b) are reproduced with permission,[151] Copyright 2019, Elsevier. (c)–(e) are reproduced under Creative Commons CC-BY license,[57] Copyright 2021, Springer Nature. (f) and (g) are reproduced under Creative Commons CC-BY license,[154] Copyright 2021, Royal Society of Chemistry.

As shown in Fig. 9c and d, the periodicity of the alternating contrast variation of the cation-ordered structure is twice as large as that of the normal layered structure. Cation ordering is often found when a Ni-rich layered cathode is doped with ions possessing high oxidation states ($\geq$4+). Indeed, the introduction of Ti^{4+}, Ta^{5+}, and Mo^{6+} into the Ni-rich cathode triggered the formation of a cation-ordered structure whilst introducing Al^{3+}, Ga^{3+}, and Mg^{2+} produced an ordinary layered crystal structure (Fig. 9e).[53,57,58,78,153] The doping of F^- into the layered oxide cathode also induced a cation-ordered structure during cathode formation.[154] If the TM ions randomly occupy Li slabs, Li^+ migration can be hindered by the presence of TM ions. However, the cation-ordered state lowered the delithiation energy, *i.e.*, the energy required to remove a Li^+ ion from the structure, thereby facilitating Li migration (Fig. 9f).[154] Consequently, the presence of TM ions in the Li^+ layer prevented the local collapse of the layered structure and preserved the structural framework even in a highly delithiated state, thereby enhancing the reversibility of Li^+ (de)intercalation.[78] Moreover, the ordered presence of Ni ions in the Li slabs restricted the random migration of Ni ions into the Li sites, thereby delaying the structural transformation into a cation-disordered state (*e.g.*, the rock-salt structure). A combination of such compositional partitioning, the nano-rod microstructure, and the cation-ordered structure in an 80% Ni-NCM cathode led to a full cell capacity retention of 78% after 8000 cycles, which explicitly outperformed the conventional NCM cathode containing an identical Ni content (Fig. 9g).[154]

2.3.3. Twinned crystal structure. The twin crystal structure develops when the atoms constituting a single primary particle form a symmetrical mirror relationship along the crystal plane (Fig. 10a and b).[53,77] Conventionally, the presence of twinned crystal structures in cathode active materials was regarded as a structural defect, since these structures lead to a deterioration in the crystallinity of the layered oxide cathode, impeding smooth Li^+ (de)intercalation during electrochemical (dis)charge.[155–158] However, several recent studies have suggested that the formation of twinned crystals in nano-rod primary particles can improve the electrochemical performances of the cathodes (Fig. 10c).[53,72,77,159] For example, in a full concentration gradient (FCG) NCM75 cathode featuring nano-rod primary particles, the construction of numerous twins helped to improve the cycling stability of the cathode.[160] The twinned crystals present in the FCG NCM75 were driven by the lattice mismatch between MnOOH and $Ni(OH)_2$ in the cathode calcined at 790 °C, featuring a concentration gradient and nano-rod twins. In contrast, the cathode calcined at 820 °C and featured a lesser concentration gradient along with thick primary particles containing no twinned crystals (Fig. 10d). The twinning crystal structure was predominantly observed at the surface of the FCG NCM75 calcined at 790 °C and gradually disappeared upon moving toward the particle center, where the Mn fraction progressively decreased. This result supported the observed formation twinning upon Mn-enrichment of the cathode surface in the presence of a concentration gradient. The performance improvement achieved by constructing twinned crystals was also demonstrated in nano-rod cathodes without a concentration gradient. For example, Zr-doped LNO developed twinned crystals with the (001) plane as its twin boundary and exhibited an improved electrochemical performance compared to the undoped LNO.[77] In the Mn-doped NCA92 cathode, bonding between the two well-ordered layered domains led to an atomically sharp twin boundary along the (010) plane (Fig. 10e and f).[72] Because the two symmetrical domains shared the same twin boundary, the atomic stacking sequence was well-preserved on both sides of the twin boundary, and so construction of the twinned crystal structure did not impede Li^+ diffusion. In addition, because Li^+ migration across the twin boundaries requires a much higher activation energy than migration along the twin boundaries, the presence of twins helped promote the migration of Li^+ along the *a*–*b* planes, fostering the kinetics of (de)lithiation.[72,161] Furthermore, the twinning of the two-layered structures began to disappear as the calcination temperature or duration increased. In the NCTa89 cathode, the cathode calcined at 730 °C contained numerous twinned crystals; however, upon increasing the calcination temperature, the electron diffraction spots corresponding to the twins eventually faded out after calcination at 790 °C.[53] In addition, B-doped NCA95 calcined at 700 °C for 30 min contained a myriad of twins, while the cathodes calcined at 700 °C for 5 and 10 h were free of twins (Fig. 10g).[116] The electrochemical performances of these cathodes were found to be optimal in the presence of twinned crystal structures. Based on a series of TEM results, the twinned crystal structure likely originated from the hydroxide precursor. The subsequent mitigation of random coarsening of the primary particles *via* the concentration gradient or hetero-elemental doping produced radially aligned nano-rod grains, which then inherited the twinned feature of the hydroxide precursor.

2.4. Chemical and structural stability

The degradation of NCM and NCA cathodes is largely caused by the presence of unstable Ni^{4+} in their highly delithiated states. During cell operation, Ni^{4+} ions can readily react with the electrolyte solution to produce Ni^{2+}, thereby forming the NiO-like rock-salt structure, which increases the resistance and deteriorates the electrochemical performance of the cathode.[162–165] Moreover, such side reactions can cause gas evolution, which leads to pressure buildup, potentially causing leaks or explosions in extreme cases, ultimately jeopardizing the safety of the battery.[37,166–169] Such degradation becomes more severe as the Ni fraction of the cathode increases.[31,36,37] As the degradation primarily occurs at the surface of the cathode that is in contact with the electrolyte, the rate of degradation is largely determined by the area exposed to the electrolyte. In the following subsections, the chemical stability and the extent of chemical degradation of the nano-rod cathodes will be addressed, both on the outer surfaces of the particles and on the interior surfaces of the cathode particles.

2.4.1. Outer surface degradation. Since the degree of surface degradation varies considerably depending on the exposed facets of the primary particles, the construction of nano-rod grains can affect the chemical and structural degradation of the cathode secondary particles. Nano-rod grains have much thinner plates than equiaxed primary particles, and they also

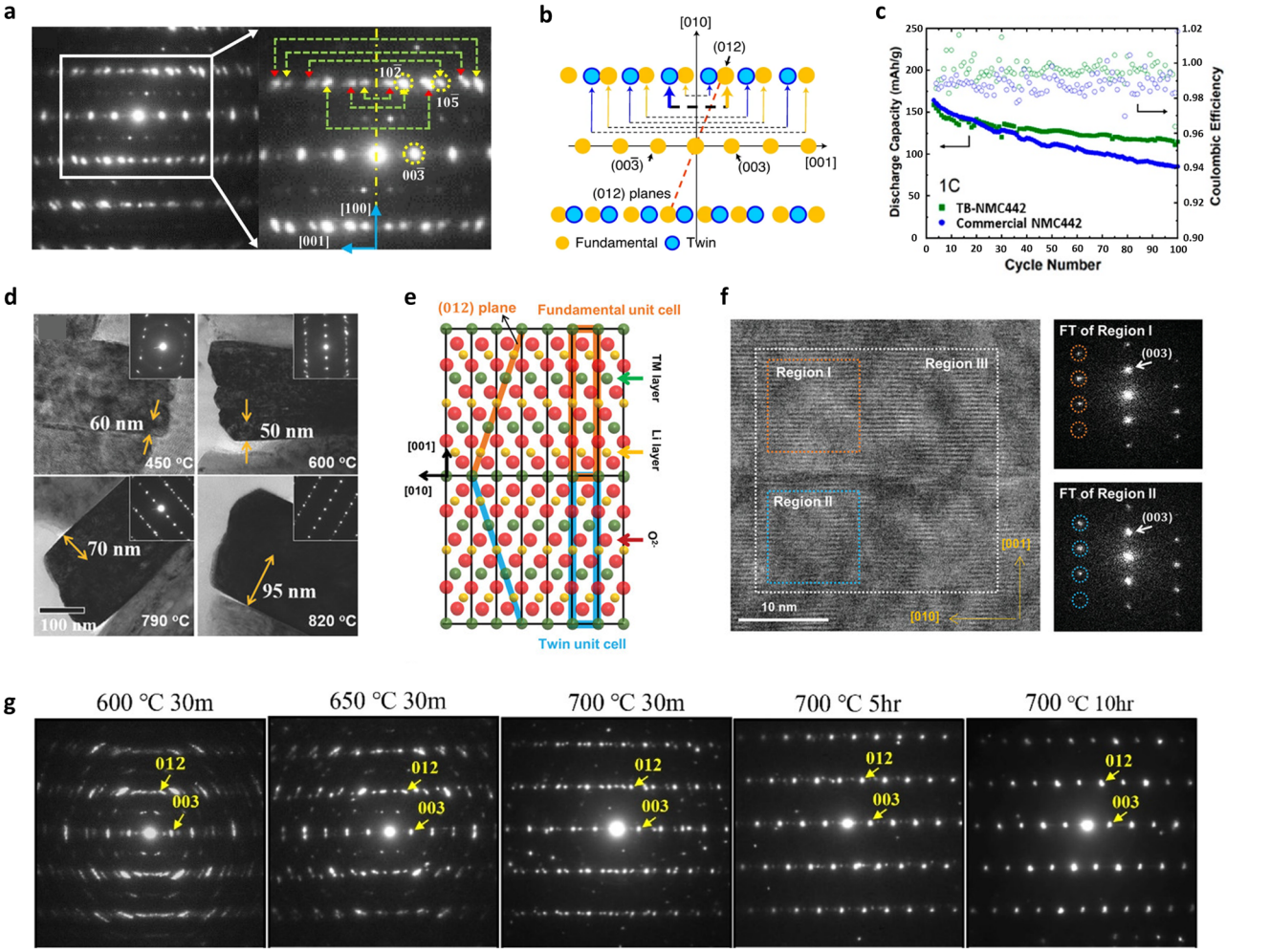

Fig. 10 (a) Electron diffraction pattern recorded for a twinned primary particle from the Zr-doped $LiNiO_2$. The magnified pattern is also shown to indicate the paired diffraction spots caused by the mirror reflection of the [010] zone pattern around the [100] twin plane. (b) Schematic representation of the [100] zone electron diffraction pattern of the layered $R\bar{3}m$ structure corresponding to the fundamental and twin regions. (c) Electrochemical performances of TB-NMC442 and commercial NMC442 cathodes in the voltage range of 2.5–4.7 V. (d) Bright-field TEM images of the FCG cathode, $Li[Ni_{0.75}Co_{0.10}Mn_{0.15}]O_2$, lithiated at different temperatures. Thickness measurements for the respective twins are also shown. The corresponding SAED patterns showing the twin relationships are presented in the insets. (e) Schematic illustration showing an atomic arrangement of the twinned crystal structure. (f) HR-TEM image and corresponding Fourier transforms of the marked regions (regions I and II) of the 4% Mn-doped CG NCA92 cathode. (g) [100]-zone SAED pattern of the 1.5% B-doped NCA95 cathode lithiated at different temperatures and durations. (a) is reproduced with permission,[77] Copyright 2018, American Chemical Society. (b) is reproduced with permission,[53] Copyright 2020, Springer Nature. (c) is reproduced under Creative Commons CC-BY license,[159] Copyright 2022, American Chemical Society. (d) is reproduced with permission,[160] Copyright 2018, John Wiley and Sons. (e) and (f) are reproduced with permission,[72] Copyright 2024, John Wiley and Sons. (g) is reproduced with permission,[116] Copyright 2022, American Chemical Society.

feature more abundant lateral facets and fewer frontal facets than polygonal-shaped grains (Fig. 11a).[69] The structural damage along the lateral side of the grain is insignificant, whereas the frontal side of the grain is more susceptible to structural degradation. As shown in Fig. 11b, the (001) facet parallel to the Li^+ diffusion pathway is more stable to electrochemical cycle-induced irreversible structural degradation than the other facets.[66] In addition, the construction of elongated nano-rod primary particles has been demonstrated to attenuate parasitic chemical reactions along the surfaces in contact with the electrolyte solution. For example, Ni *et al.*[170] showed that the degree of byproduct formation (*e.g.*, C_2F^-, C_2HO^-, PO_2^-, LiF_2^-, and NiF_3^-) originating from unwanted electrolyte decomposition and interfacial parasitic reactions was significantly reduced in the presence of nano-rod grains in the 1Sb-NCA cathode (Fig. 11c). By effectively alleviating irreversible structural degradation and oxidative decomposition of the electrolyte, the nano-rod primary particles can mitigate gas evolution, TM dissolution (Fig. 11d and e).[55,58,69,98,171] The enhanced chemical stability of the nano-rod cathode system was further confirmed during the storage of a highly delithiated cathode in the electrolyte solution, wherein a greater reactivity between the cathode and the electrolyte significantly challenges the chemical stability of the Ni-rich cathode.[172] By constituting

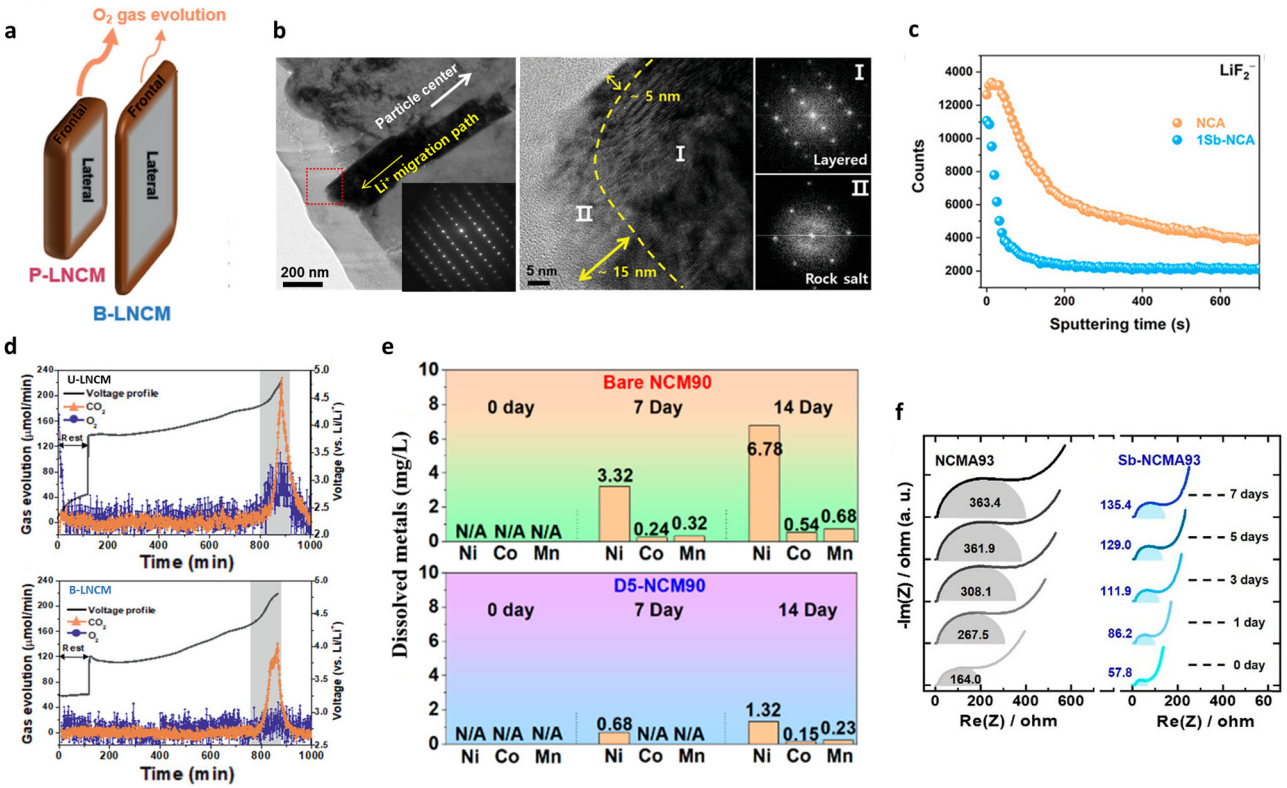

Fig. 11 (a) Schematic illustration of the structural stability differences between the P-LNCM and B-LNCM cathodes. (b) Magnified TEM image, SAED pattern (inset), HR-TEM image, and corresponding Fourier transforms for the CSG-NCMA90 primary particle after 500 cycles at 100% depth of discharge (DoD). (c) ToF-SIMS depth profiles of LiF_2^- obtained from the NCA and 1Sb-NCA cathodes after 200 cycles. (d) Differential electrochemical mass spectrometry (DEMS) spectra of U-LNCM and B-LNCM when charged to 4.8 V at 0.1C (20 mA g^{-1}). (e) ICP analysis results of the dissolved Ni, Co, and Mn ions for bare NCM90 and D5-NCM90 cathodes after storing the cathodes in the electrolyte solution for 14 d at 55 °C. (f) Changes in the charge-transfer resistances of the NCMA93 and Sb-NCMA93 cathodes during a storage test. (a) is reproduced with permission,[69] Copyright 2021, John Wiley and Sons. (b) is reproduced with permission,[66] Copyright 2021, John Wiley and Sons. (c) is reproduced with permission,[170] Copyright 2023, American Chemical Society. (d) is reproduced with permission,[69] Copyright 2021, John Wiley and Sons. (e) is reproduced with permission,[55] Copyright 2023, American Chemical Society. (f) is reproduced with permission,[172] Copyright 2023, American Chemical Society.

highly textured nano-rod grains, the Sb-NCMA93 cathode mitigated thickening of the cathode–electrolyte interphase, thereby alleviating any increment in the charge transfer resistance (R_{ct}), and enhancing the electrochemical performance of the cathode (Fig. 11f). Reducing the relative fraction of Ni compared to the constituent elements (*e.g.*, Co and Mn) at the particle surface can further prevent the unwanted side reactions originating from electrolyte decomposition. For example, the CSG-NCAB87 cathode containing a relatively lower Ni concentration at the outer surface of the particle effectively circumvented the capacity fading originating from cumulative exposure to the electrolyte, thereby markedly improving its long-term cycling performance.[173] Thus, surface protection strategies, such as compositional partitioning and hetero-elemental coating, should be employed to maximize the electrochemical performance of the nano-rod cathode.

2.4.2. Interior surface degradation. The degradation sites of a cathode active material are not confined to the outer surfaces but also include the internal surfaces of the cathode particles. Due to the fact that Ni-rich cathodes can undergo the H2 → H3 phase transition, where an anisotropic volume change mechanically damages the particle to form microcracks, the cycling-induced newly exposed internal surfaces of the cathode can act as fresh reaction sites for electrolyte decomposition.[36,119] Once microcracks are formed, the electrolyte solution can easily permeate into the cathode particle interior, which can react readily with the internal surfaces (Fig. 12a).[79,106,138] Notably, the presence of F and P, which originate from the $LiPF_6$ and $LiPF_6$-derived cathode–electrolyte interphase species to provide direct chemical evidence of electrolyte penetration, was minimal within the rod-shaped cathode particles.[75] As shown in Fig. 12b, after electrochemical cycling, the equiaxed-type cathode contained intergranular boundaries that were completely passivated by Ni^{2+}, indicating the formation of a NiO-like rock-salt impurity phase resulting from intimate contact with the electrolyte.[52] However, Ni^{2+} was limited to the secondary particle surface of the nano-rod-grained cathode, confirming good chemical and structural stabilities (Fig. 12c). Microcrack formation and subsequent irreversible structural degradation of the internal grains rendered the primary particles electrochemically isolated, thereby amplifying capacity loss during electrochemical cycling (Fig. 12d).[106] In contrast, the formation of radially aligned nano-rod grains efficaciously mitigated such degradation of the inner particles. The conductivity map obtained *via* the scanning spreading resistance microscopy (SSRM) mode of

atomic force microscopy (AFM) showed that the electronic conductance of the cycled nano-rod cathodes did not vary significantly within the particles, indicating that degradation of the secondary particle inner surfaces was well circumvented, as microcracking was largely suppressed.

It has also been demonstrated that the formation of nano-rod grains mitigates the cycle-induced internal surface degradation of the cathodes and has a similar effect during thermal aging. More specifically, the storage of highly delithiated cathodes in an electrolyte solution at elevated temperatures (*e.g.*, 45 and 60 °C) was found to undermine the structural stability of the equiaxed cathode, eventually leading to mechanical failure and capacity loss during aging (Fig. 12e and f).[50,146] In contrast, the tighter packing of the cathode secondary particle surfaces imparted by the nano-rod grains effectively protected the particle interior from chemical attack during prolonged exposure to the electrolyte, thereby preserving the reversibility of Li^+.[52] By combining crystallographic textures and compositional partitioning of the particles of the cathode prepared using a concentration gradient, both chemical and structural degradation were noticeably circumvented, confining Ni^{2+} at the very edge of the secondary particle surface (Fig. 12g).[98] When the electrolyte penetrates into the secondary particle of this cathode, the deterioration at the particle center is likely accelerated because the cathode center consists of capacity-maximizing but chemically unstable Ni-enriched compositions. Thus, suppressing the proliferation of intergranular cracks that extend from the secondary particle center to the surface is key to delaying the degradation of inner primary particles.

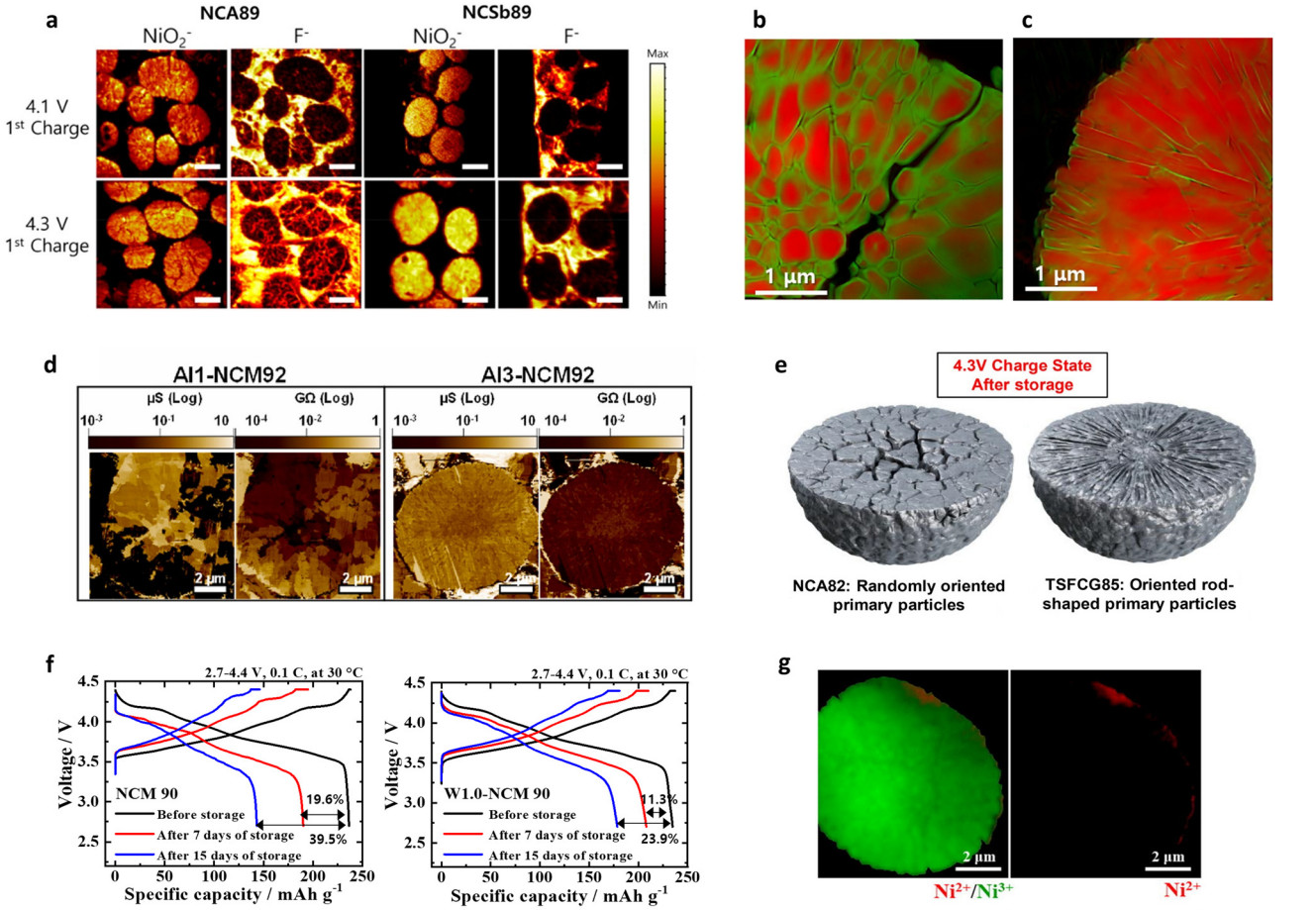

Fig. 12 (a) Cross-sectional TOF-SIMS high-resolution maps showing the NiO_2^- and F^- secondary ion spatial distributions acquired on the NCA89 and NCSb89 cathodes charged to 4.1 and 4.3 V after the first 0.1C (18 mA g^{-1}) cycle. Scale bar = 5 μm. (b) Cross-sectional chemical maps of the P-NCA89 and B-NCA88 cathodes after 100 cycles. The fitting results (chemical information) and averaged OD (morphological information) are indicated based on the color and transparency, respectively. Red and green represent Ni^{3+} and Ni^{2+}, respectively. (d) SSRM images of the Al1-NCM92 and Al3-NCM92 cathodes after 500 cycles mapping their conductance and resistance. (e) Schematic description of the high-temperature (55 °C) aged NCA82 and TSFCG85 cathodes showing the internal morphological differences and the sustained damage. (f) Charge–discharge curves at 0.1C (18 mA g^{-1}) after *n* days of thermal aging, compared to those before storage (*n* = 7, 15), for the NCM90 and W1.0-NCM90 cathodes. (g) Cross-sectional chemical phase maps of the FCG NCM78_790 °C cathode particles after 1000 cycles. (a) is reproduced with permission,[75] Copyright 2020, American Chemical Society. (b) and (c) are reproduced with permission,[52] Copyright 2020, Elsevier. (d) is reproduced with permission,[106] Copyright 2023, Elsevier. (e) is reproduced with permission,[50] Copyright 2017, American Chemical Society. (f) is reproduced with permission,[146] Copyright 2019, Elsevier. (g) is reproduced with permission,[98] Copyright 2022, Elsevier.

2.5. Thermal stability

Recently, the growing importance of battery safety has highlighted thermal propagation as a major issue. Excessive heat generation within a battery cell can lead to a chain reaction, wherein the neighboring cells also become overheated and contribute to thermal propagation, resulting in fires or even explosions.[174–178] One of the primary causes of thermal instability in a battery is the cathode, which can continually supply O_2 during thermal reactions, thereby intensifying the risk of thermal runaway.[179–181] As has been well established, the thermal safety of conventional NCM or NCA cathodes depend on their relative fractions of Ni. More specifically, the higher Ni concentration required to achieve a greater energy density can adversely affect the thermal safety of a cathode active material (Fig. 13a).[31,39] Indeed, during cell operation, delithiated NCM or NCA cathodes contain unstable Ni^{4+} species, which can readily react with the electrolyte solution to generate heat and gaseous species.[182] To address this issue, Sun *et al.*[46] suggested that the use of an NCM cathode possessing nano-rod grains with a concentration gradient should effectively promote the thermal safety of a cathode (Fig. 13b). DSC analysis of an FCG cathode material containing an inner composition (IC) of $Li[Ni_{0.86}Co_{0.10}Mn_{0.04}]O_2$ and an outer composition (OC) of $Li[Ni_{0.70}Co_{0.10}Mn_{0.20}]O_2$ revealed that the thermal properties resembled that of an OC cathode. More specifically, the exothermic reaction temperatures of the IC, FCG, and OC cathodes were 221.3, 257.3, and 259.7 °C, respectively. Relatively lower content of Ni at the outer surface of the nano-rod FCG material was found to be key to mitigating the thermal reaction at the cathode.[183,184] In addition, a relatively higher fraction of Mn has been demonstrated to help mitigate oxygen

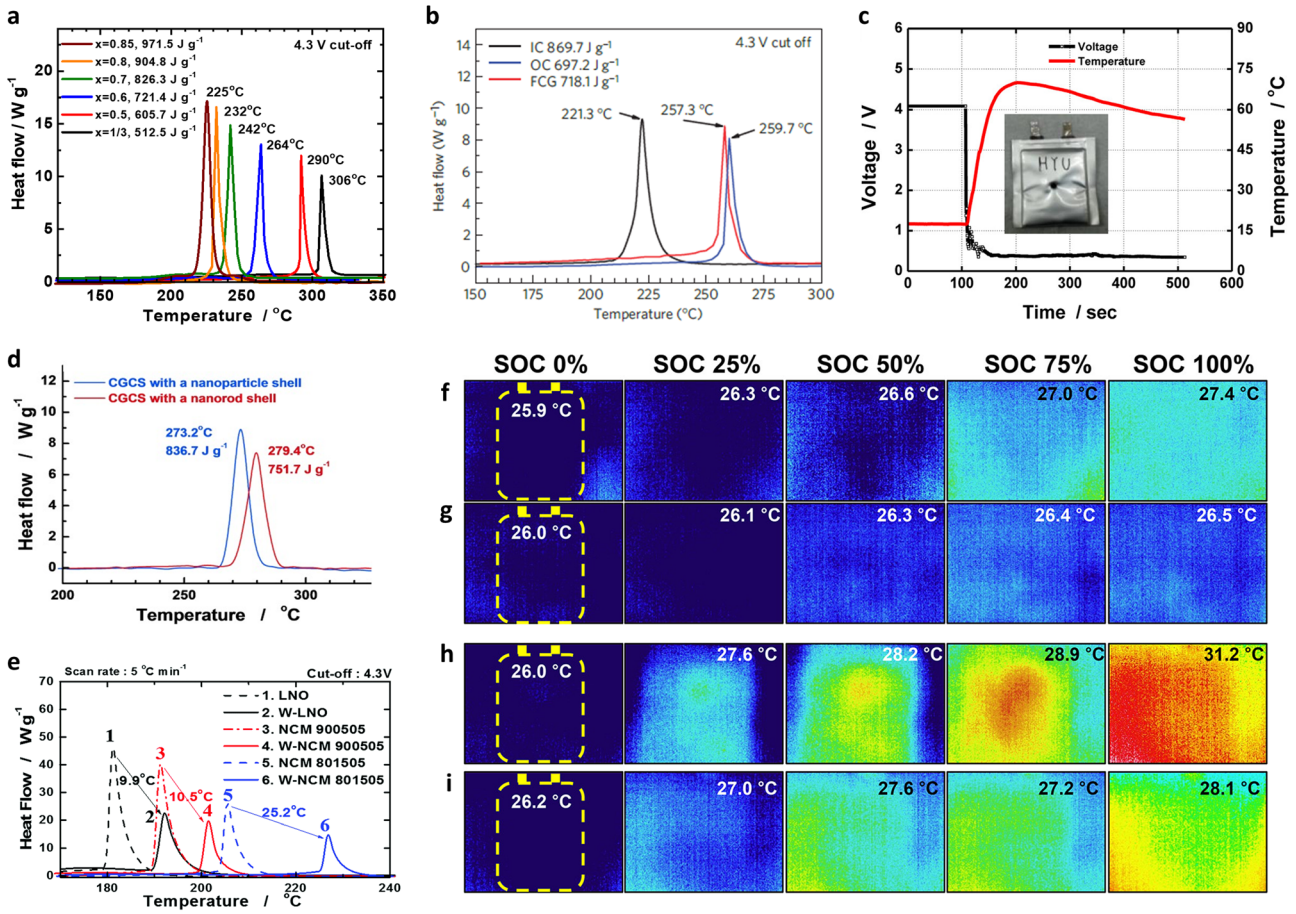

Fig. 13 (a) DSC profiles of the delithiated $Li_{1-\delta}[Ni_xCo_yMn_z]O_2$ (x = 1/3, 0.5, 0.6, 0.7, 0.8, and 0.85) cathodes. (b) DSC profiles of the delithiated FCG material, the delithiated IC, and the delithiated OC ($Li_{1-x}Ni_{0.70}Co_{0.10}Mn_{0.20}O_2$) recorded at a scan rate of 1 °C min^{-1}. The cells were charged in the constant-voltage mote to 4.3 V *versus* Li^+/Li before disassembly. (c) Plots of the voltage and cell temperature against time for a laminated-type Al-pouch MCMB/FCG–Mn-F cell (280 mA h) during a penetration test at 100% SoC (4.2 V). (d) DSC profiles of the delithiated CGCS $Li_{0.18}[Ni_{0.60}Co_{0.15}Mn_{0.25}]O_2$ particles with a nanoparticle shell and the delithiated CGCS $Li_{0.16}[Ni_{0.60}Co_{0.15}Mn_{0.25}]O_2$ with a nano-rod shell. (e) DSC results of the pristine, W-doped $Li[Ni_xCo_yMn_{1-x-y}]O_2$ (x = 0.8, 0.9, and 1.0; y = 0.15, 0.05, and 0) combined with a 1.2 M $LiPF_6$ (EC/EMC, 3 : 7 v/v) + 2 wt% VC electrolyte solution. Distribution of the surface temperature in pouch-type full-cells measured using an IR camera during charge to 4.2 V *vs.* graphite. Thermal images of the (f) NCA93- and (g) Nb-NCA93-based cells charged at 0.1C (18 mA g^{-1}), and of the (h) NCA93- and (i) Nb-NCA93-based cells charged at 3C (540 mA g^{-1}). (a) is reproduced with permission,[31] Copyright 2013, Elsevier. (b) is reproduced with permission,[46] Copyright 2012, Springer Nature. (c) is reproduced with permission,[48] Copyright 2013, American Chemical Society. (d) is reproduced with permission,[188] Copyright 2014, John Wiley and Sons. (e) is reproduced with permission,[138] Copyright 2018, Royal Society of Chemistry. (f)–(i) are reproduced under Creative Commons CC-BY license.[189] Copyright 2022, American Chemical Society.

release from the layered structure, reducing the risk of thermal reactions.[185–187] Notably, the thermal safety of a nano-rod material with a concentration gradient is not confined to the particle level but is related to the cell level. In this context, Noh *et al.*[48] reported overcharging and nail penetration test results for laminated-type Al-pouch cells (280 mA h) featuring a nano-rod concentration gradient cathode and found that no thermal runaway, black smoke or explosions occurred during the experiments (Fig. 13c).

The primary particle morphology close to the secondary particle surface also plays a critical role in defining the thermal stability of a cathode. For example, concentration gradient core–shell (CGCS) cathodes bearing nano-particle and nano-rod shells exhibited exothermic peak temperatures of 273.2 and 279.4 °C while releasing 836.7 and 751.7 J g^{-1} of heat, respectively. These results demonstrate the superior thermal runaway resistance of the nano-rod-grained cathode (Fig. 13d).[188] Recently, nano-rod grains without a concentration gradient were proven to improve the thermal safety profiles of cathodes effectively.[73,109,138,190] More specifically, the W doping of Ni-rich cathodes substantially reduced the cathodic thermal activity, thereby shifting the onset of the exothermic reactions by >10 °C and reducing the amount of overall heat released during the thermal reactions (Fig. 13e).[138] These outstanding thermal properties observed for nano-rod cathodes can be attributed to the chemo-mechanical protection offered by the tightly packed radially oriented grains, which mitigate microcrack propagation and protect internal particle surfaces from direct contact with the electrolyte.[68,97] In this context, using an infrared camera, Kim *et al.*[189] directly demonstrated the thermal response of a pouch-type full cell (800 mA h) during charging. During charging of the full cells at 0.1C, the NCA93- and Nb-NCA93-based full cells showed temperature increments of 1.5 and 0.5 °C, respectively (Fig. 13f and g). However, upon charging the full cells at 3C, the equiaxed-grained NCA93 revealed high levels of heat localization, whereas the nano-rod-grained Nb-NCA93 exhibited a relatively lower surface temperature and no localized heat generation, even at a high current density (Fig. 13h and i). These results indicate the highly textured nano-rod grains can effectively protect the internal surface of the cathode active material, thereby delaying the onset of exothermic reactions, and improving the cathode and battery safety.

2.6. Mechanical strength

The fundamental mechanical strength of a single cathode active material largely affects the electrochemical cycling stability of a cathode. However, the high-pressure rolling process employed during electrode manufacture hampers the mechanical integrity of the cathode.[191–194] To determine the mechanical strength of a cathode active material, the micro-indentation approach is commonly employed.[195–198] This involves loading a flat indenter on a single cathode particle, applying an external force, and recording the mechanical response until particle fracture occurs (Fig. 14a).[55] Compression tests can be accelerated tests to determine whether a cathode can dissipate the internal strain under electrochemical effects. In particular, the test provides valuable data when adopted in Ni-rich cathodes, which generally suffer from microcrack formation and subsequent mechanical failure during electrochemical charging and discharging.[36,79,199] In this context, Ju *et al.*[55] compared the mechanical strengths of the D5-NCM90 and NCM90 cathodes, which possess identical chemical compositions but different grain morphologies (*i.e.*, randomly oriented equiaxed grains and radially aligned nano-rod grains, respectively). They found that the D5-NCM90 cathode exhibited a higher mechanical strength than the NCM90 cathode, with the maximum applied forces reaching 30.5 and 10.2 mN, respectively. These results demonstrate that nano-rod grains effectively enhance the fracture toughness of a cathode. Similarly, it was found that an ultrafine-grained Mo-doped NCMA94 cathode showed a higher mechanical strength than the corresponding undoped cathode. Moreover, increasing the Mo fraction refined the nano-rod grains to further increase the mechanical robustness of the cathode particles (Fig. 14b).[80] This increased mechanical strength was attributed to the presence of abundant triple junctions at the interparticle boundaries, which can serve as barriers to relaxing the mechanical strain effectively.[200,201] Recent studies on nano-rod-grained cathodes have revealed that the cathodes exhibit a peculiar ductile mechanical behavior. More specifically, the force-displacement curves recorded for conventional cathode materials displayed relatively straight load curves before particle breakage, indicating their brittle characteristics typical in ceramic materials (Fig. 14c).[79] In contrast, ultrafine-scaled nano-rod grains showed nonlinear and serrated flow load curves, indicating their ductile properties. Such a ductile response against external forces can improve the fracture toughness of a cathode particle by effectively dissipating the strain accumulation into the cathode material.[202,203] Scanning electron microscopy (SEM) images of the fractured particles demonstrated the different mechanical responses between the equiaxial-grained and nano-rod-grained cathodes; the former catastrophically shattered into numerous grain fragments, whereas the latter fractured into larger aggregates (Fig. 14d). The use of cyclic loading/unloading tests to simulate lattice contraction and expansion in a cathode during electrochemical cycling substantiated the mechanical durability of the nano-rod-grained particles. More specifically, during the cyclic test, the equiaxial-grained FCG NCM78 was steadily but increasingly compressed to 165% compared to its initial displacement (L_1) (Fig. 14e).[204] In comparison, the compression ratio of the rod-shaped W0.5-FCG NCM78 was limited to 125% after the same number of cycles. Furthermore, the equiaxial-grained particles collapsed before reaching 150 cycles, whereas most nano-rod-grained particles remained intact after 250 cycles (Fig. 14f).[205] Moreover, the indentation results suggested that the radial orientation of the nano-rod grains helped dissipate the inherent strain buildup of the layered oxide cathode, mitigating microcrack formation and enhancing the electrochemical performance. These characteristics of nano-rod cathodes are also advantageous during manufacture and application. Indeed, the electrode manufacturing process involves the implementation of high compression forces perpendicular to the particle surface to increase the packing and energy density of the electrode. By

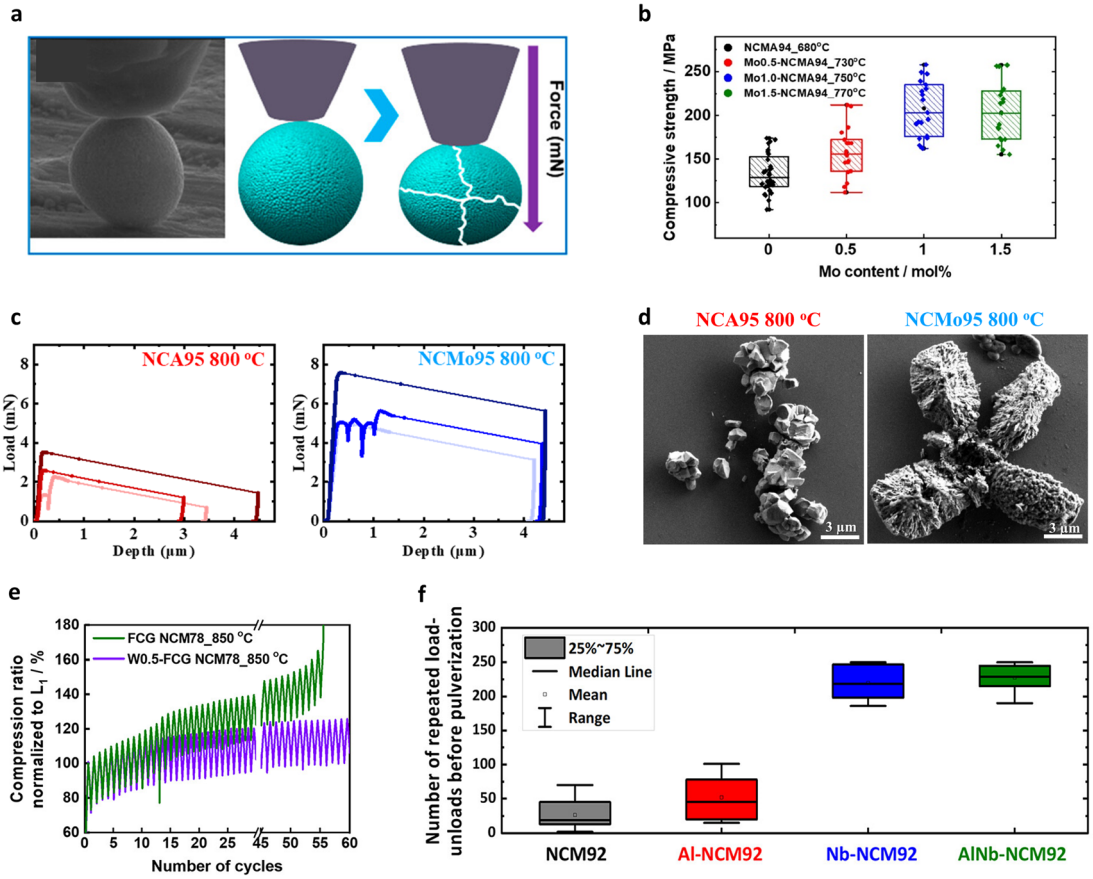

Fig. 14 (a) Schematic representation of nanoindentation analysis carried out before and after mechanical failure of the cathode particle. (b) Distribution of the particle strength for the optimized NCMA94 and Mo-doped NCMA94 cathodes. (c) Representative load-displacement curves for the NCA95 and NCMo95 cathode particles lithiated at 800 °C for 10 h. (d) Post-compression SEM images of the NCA95 and NCMo95 cathode particles lithiated at 800 °C for 10 h. (e) Comparison of the mechanical durability during cyclic loading/unloading tests of the FCG NCM78 and W0.5-FCG NCM78 cathodes calcined at 850 °C. (f) Number of repeated loading/unloading cycles before pulverization was observed for the NCM92, Al-NCM92, Nb-NCM92, and AlNb-NCM92 cathodes, as obtained *via* micro-compression analysis. (a) is reproduced with permission,[55] Copyright 2023, American Chemical Society. (b) is reproduced with permission,[80] Copyright 2023, Elsevier. (c) and (d) are reproduced under Creative Commons CC-BY license,[79] Copyright 2021, Royal Society of Chemistry. (e) is reproduced with permission,[204] Copyright 2023, American Chemical Society. (f) is reproduced with permission,[205] Copyright 2024, American Chemical Society.

securing a high fracture toughness, the nano-rod-grained cathodes can preserve their original particle morphologies in high-density electrodes, avoiding the particle breakage observed for conventional equiaxial-grained layered oxide cathodes.

2.7. Ion diffusion & fast charging

The sizes, morphologies, and grain orientations of primary particles largely affect the Li^+ ion diffusivity of the material. One of the benefits of constructing radially oriented nano-rod grains is the enhancement in the Li^+ ion diffusivity. In the following subsections, the Li^+ diffusivity and uniformity in a single cathode material are discussed in the context of the cathode microstructure, as is the resulting structural stability of the final cathode material.

2.7.1. Li^+ ion diffusion. Primary particles consisting of conventional layered oxide cathodes are predominantly oriented in an irregular manner. Due to the fact that the Li^+ present in a layered oxide cathode should (de)intercalate along the *ab*-plane of the crystal structure, the orientation of constitutive grains largely affects the Li^+ diffusivity. Consequently, the Li^+ ion diffusion pathways for such conventional layered oxide cathodes are normally zigzagged and complex. As suggested by Lee *et al.*,[206] Li^+ diffusion from the center to the surface of a conventional NCM90 secondary particle follows a relatively long pathway compared to that of the cathodes comprised of highly textured rod-shaped grains (Fig. 15a). Although the central grains of modified cathodes are still oriented irregularly, the peripheral rod-like grains with strong crystallographic textures facilitate Li^+ diffusion (Fig. 15b).[101] As a result, the radially aligned primary particles in the cathode material provide relatively straight and rapid diffusion pathways for Li^+ transport, thereby increasing the rate capability of the cathode.[207–210] For confirmation, an investigation of the Li^+ diffusion kinetics using the galvanostatic intermittent titration technique (GITT) showed a larger Li^+ diffusion coefficient in the microstructurally modified cathode than in the unmodified cathode (Fig. 15c).[73]

Another possible reason for the improved rate performance in nano-rod-grained cathodes is the large fraction of interparticle

boundaries. It is often reported that grain boundary diffusion is 3–10 times faster than bulk diffusion.[212,213] With this in mind, Fig. 15d compares the rate capabilities of the NCA93, B-NCA93, and Nb-NCA93 cathodes as a function of the primary particle count in a respective secondary particle. Notably, an increment in the number of grains in a single secondary particle indicates augmentation in the relative fraction of interparticle boundaries. The rate performance of the nano-rod Nb-NCA93 cathode containing the highest number of grains was found to be superior to that of the B-NCA93 and NCA93 cathodes, featuring elongated rod-like grains and equiaxed grains, respectively. These results confirm the positive impact of numerous grain boundaries in promoting Li^+ migration. The construction of nano-rod grains with a concentration gradient offers outstanding power density retention compared to the cathode without any microstructural modification or concentration gradient (Fig. 15e).[66] However, the Li^+ kinetics of a cathode containing a concentration gradient largely depend on its calcination temperature. The corresponding selected area electron diffraction (SAED) patterns confirmed that FCG NCM78 calcined at 790 °C possessed a continuous Li^+ pathway across the adjacent primary particles (Fig. 15f).[160] However, the cathode calcined at 850 °C, wherein a unique texture was barely discernible owing to grain coarsening, possessed a discontinuous migration pathway for Li^+ (de)intercalation. The calcination temperature-dependent

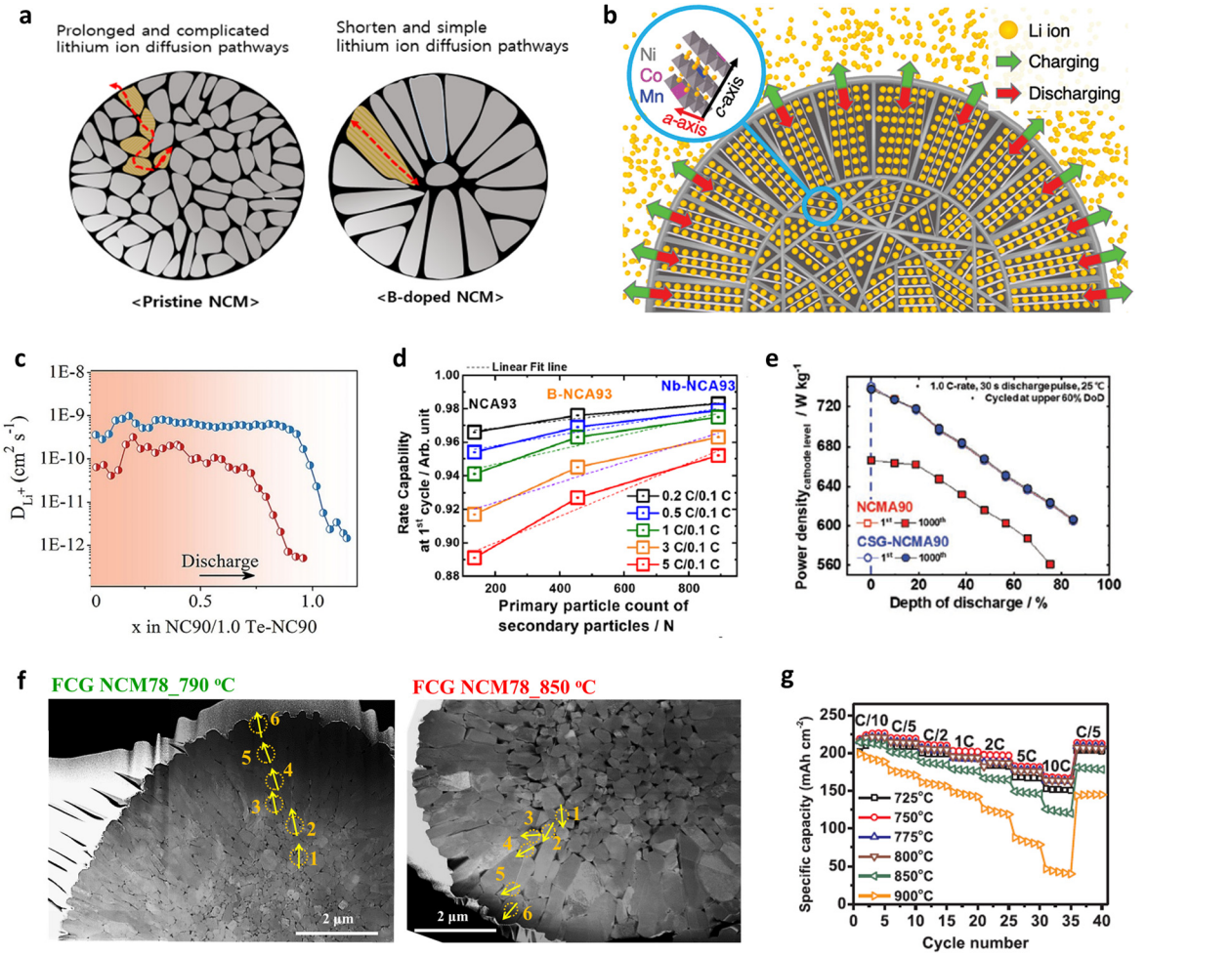

Fig. 15 (a) Schematic illustration of the Li^+ diffusion pathways in pristine and B-doped NCM cathode particles. (b) Rendered image of a core–shell particle based on t-EBSD data. Radial alignment of primary particle Li layers allows faster diffusion from the electrolyte towards the randomly oriented core during discharging (red arrows), and in the inverse direction during charging (green arrows). (c) Calculated D_{Li+} values of the NC90 and 1.0 Te-NC90 cathodes during charging. (d) Plots of the 0.2/0.1, 0.5/0.1, 1/0.1, 3/0.1, and 5/0.1C (0.1C corresponds to 18 mA g^{-1}) capacity ratios for the half-cells based on NCA93, B-NCA93, and Nb-NCA93 cathodes as a function of the primary particle count in the secondary particles. (e) Power densities of the NCMA90 and CSG-NCMA90 cathodes as a function of the DoD before and after 1000 cycles at upper 60% DoD (blue dashed lines indicate the fully charged state). (f) Cross-sectional dark-field TEM images showing the morphologies and crystal orientations of FCG NCM78_790 °C and FCG NCM78_850 °C cathodes. The yellow arrows indicate alignment of the Li^+ paths of the numbered primary particles from the secondary particle core to its surface, determined by SAED analysis. (g) Rate performances of $LiNi_{0.76}Mn_{0.14}Co_{0.10}O_2$ cathodes calcined at different temperatures. (a) is reproduced under Creative Commons CC-BY license,[206] Copyright 2019, Springer Nature. (b) is reproduced under Creative Commons CC-BY license,[101] Copyright 2020, Royal Society of Chemistry. (c) is reproduced with permission,[73] Copyright 2024, Elsevier. (d) is reproduced under Creative Commons CC-BY license,[189] Copyright 2022, American Chemical Society. (e) is reproduced with permission,[66] Copyright 2021, John Wiley and Sons. (f) is reproduced with permission,[98] Copyright 2022, Elsevier. (g) is reproduced with permission,[211] Copyright 2018, Elsevier.

rate performance of the FCG NCM761410 cathode system is presented in Fig. 15g,[211] wherein it can be seen that the cathode calcined at 750 °C exhibited a superior rate capability to the cathodes calcined at other calcination temperatures. These results indicate that the selection of an optimal calcination temperature and microstructure is essential to achieving an outstanding Li^+ diffusivity and rate performance.

2.7.2. Structural durability upon fast charging. Fast charging is one of the key requirements for EVs. It is well known that the fast charging capability of a LIB predominantly depends on the Li^+ migration kinetics of the anode, wherein graphite and composites of graphite and silicon tend to dominate.[214–216] However, understanding the characteristics of the cathode is also key to comprehensively understanding the fast charging capability of a battery. Recently, a number of studies have highlighted the importance of the cathode in ensuring high cycling stability during high C-rate operations.[131,217–220] As stated earlier, the microstructure of a cathode affects its Li^+ diffusivity, and so the geometric characteristics of the constituent primary particles influence the relative spatial distribution of Li^+ within the grains of a single delithiated particle. Fig. 16a quantitatively compares the *c*-axis lattice parameters of Co-free NM90 and Ns-NM90 cathodes, calculated from a number of individual grains from each cathode.[132] Since the *c*-axis lattice parameter of a layered oxide cathode inherently depends on the state of charge, deviation of the *c*-axis lattice parameter between the primary particles indicates Li^+ heterogeneity.[36,118,221] The standard deviation of the interlayer distances of the fast-charged (3C) NM90 and Ns-NM90 obtained *via* a series of SAED analyses were 0.118 and 0.043 Å, respectively, suggesting that the nano-rod grains contain a relatively homogeneous concentration of Li^+. By providing a rapid Li^+ diffusion pathway along the crystallographic textures, the nano-rod-grained Ns-NM90 achieved an outstanding cycle life, retaining 79.5% of its initial capacity after 1000 cycles under fast charge (3C) cycling conditions (Fig. 16b). Any variation in the Li^+ concentration in a single secondary particle can be directly measured using ^7Li time-of-flight secondary ion mass spectrometry (ToF-SIMS). As shown in Fig. 16c, the unmodified NCA93 charged at 3C revealed a locally-varying ^7Li concentration, whereas the nano-rod-grained Nb-NCA93 exhibited a relatively uniform distribution of ^7Li.[189] The development of radially oriented nano-rod grains promoted Li^+ homogeneity, leading to uniform expansion and contraction of the unit cell and resulting in outstanding structural stability and electrochemical performance during long-term fast-charge cycling. In addition, it has been reported that SoC heterogeneity can intensify the

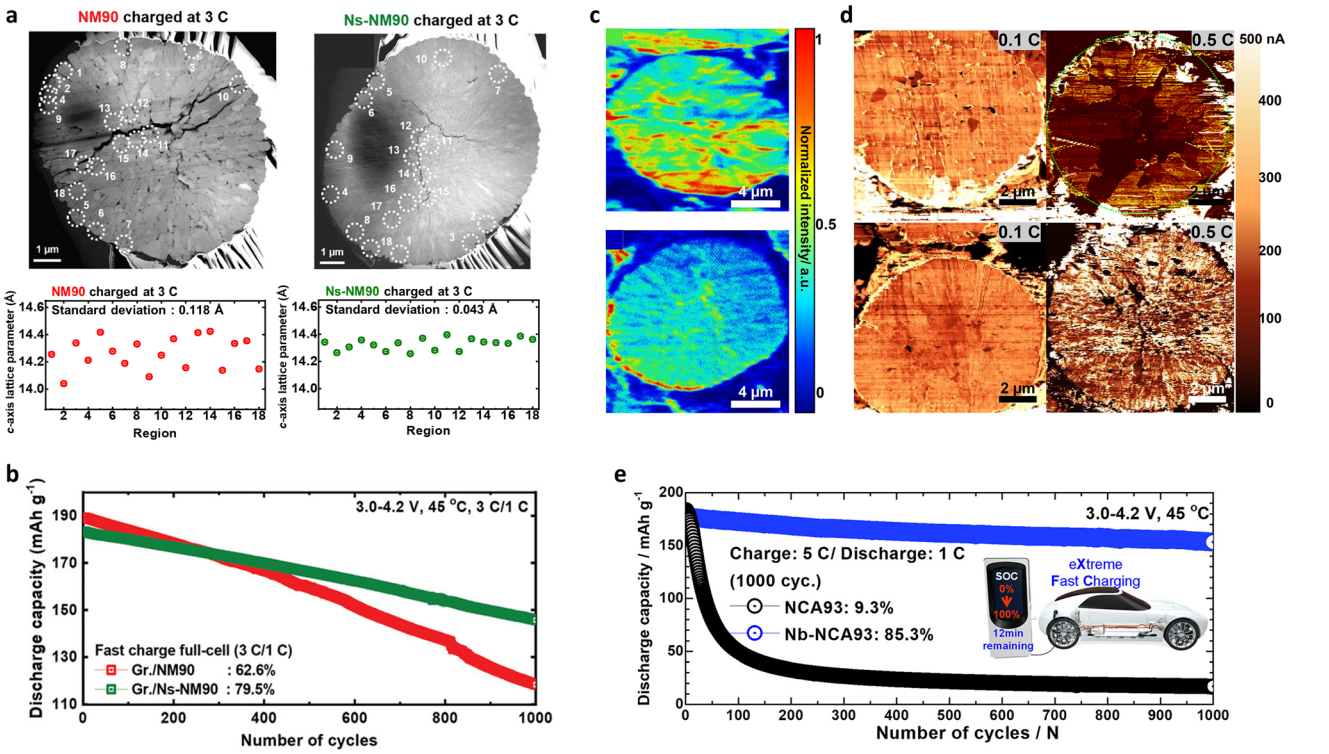

Fig. 16 (a) Cross-sectional dark-field TEM images of the NM90 and Ns-NM90 secondary cathode particles charged to 4.4 V at 3C (540 mA g^{-1}). Variation in the *c*-axis lattice parameters (corresponding to the encircled regions in part (a)) for the NM90 and Ns-NM90 cathodes charged to 4.4 V at 3C (540 mA g^{-1}). (b) Long-term cycling performances of the NM90 and Ns-NM90 cathodes in full cells containing graphite anodes and cycled at a charge C-rate of 3C (540 mA g^{-1}) at 45 °C. (c) TOF-SIMS maps of the normalized elemental distributions of ^7Li in the NCA93 (upper) and Nb-NCA93 (lower) cathodes charged to 4.3 V at 3C (540 mA g^{-1}). (d) SSRM images of the NCA93 (upper) and Nb-NCA93 (lower) cathodes charged to 4.3 V at various C-rates. (e) Comparison of the long-term cycling performances of full cells based on NCA93 and Nb-NCA93 cathodes and an EF31 + DFOB electrolyte at 5C (900 mA g^{-1})/1C (180 mA g^{-1}). (a) and (b) are reproduced with permission,[132] Copyright 2022, John Wiley and Sons. (c)–(e) are reproduced under Creative Commons CC-BY license,[189] Copyright 2022, The Authors, American Chemical Society.

mechanical strain since stress localization promotes structural distortion of the cathode active material; this results in reduced structural durability for the cathode material.[222,223] Fig. 16d compares the electrical conductivity maps of the NCA93 and Nb-NCA93 cathodes at charging C rates of 0.1 and 0.5C. It can be seen that upon charging the cathodes at 0.1C, the electrical conductivity within the cathode particles was spatially uniform in both cases.[189] However, after charging at 0.5C, the electrical conductivity of the NCA93 cathode fluctuated significantly, whereas that of the Nb-NCA93 cathode maintained its spatial uniformity. By achieving uniform (de)lithiation, the Nb-NCA93 cathode reduced the accumulation of the internal strain resulting from the charging process, thereby maintaining good structural durability and electrical conductivity. By adopting highly oriented nano-rod grains in the Nb-NCA93 cathode, a pouch-type full cell was able to operate even under 5C charge cycling; the Nb-NCA93 retained 85.3% of its initial capacity after 1000 cycles, while the NCA93 cathode exhibited only 9.3% capacity retention under the same conditions (Fig. 16e).

3. Concentration gradient cathodes

3.1. Origin of the nano-rod structure in concentration gradient cathodes

Nano-rod structures were first observed in layered oxide concentration gradient cathode materials.[46] These materials have two defining characteristics, namely the varying TM concentrations (Ni, Co, Mn, *etc.*) throughout the secondary particles and the nano-rod-shaped grain morphology found near the particle surface (Fig. 17a and b).[46,47,224–228] Concentration gradient-type cathode materials originally stemmed from the idea of placing the low-capacity but chemically stable Mn at the particle surface and the capacity contributing but reactive Ni in

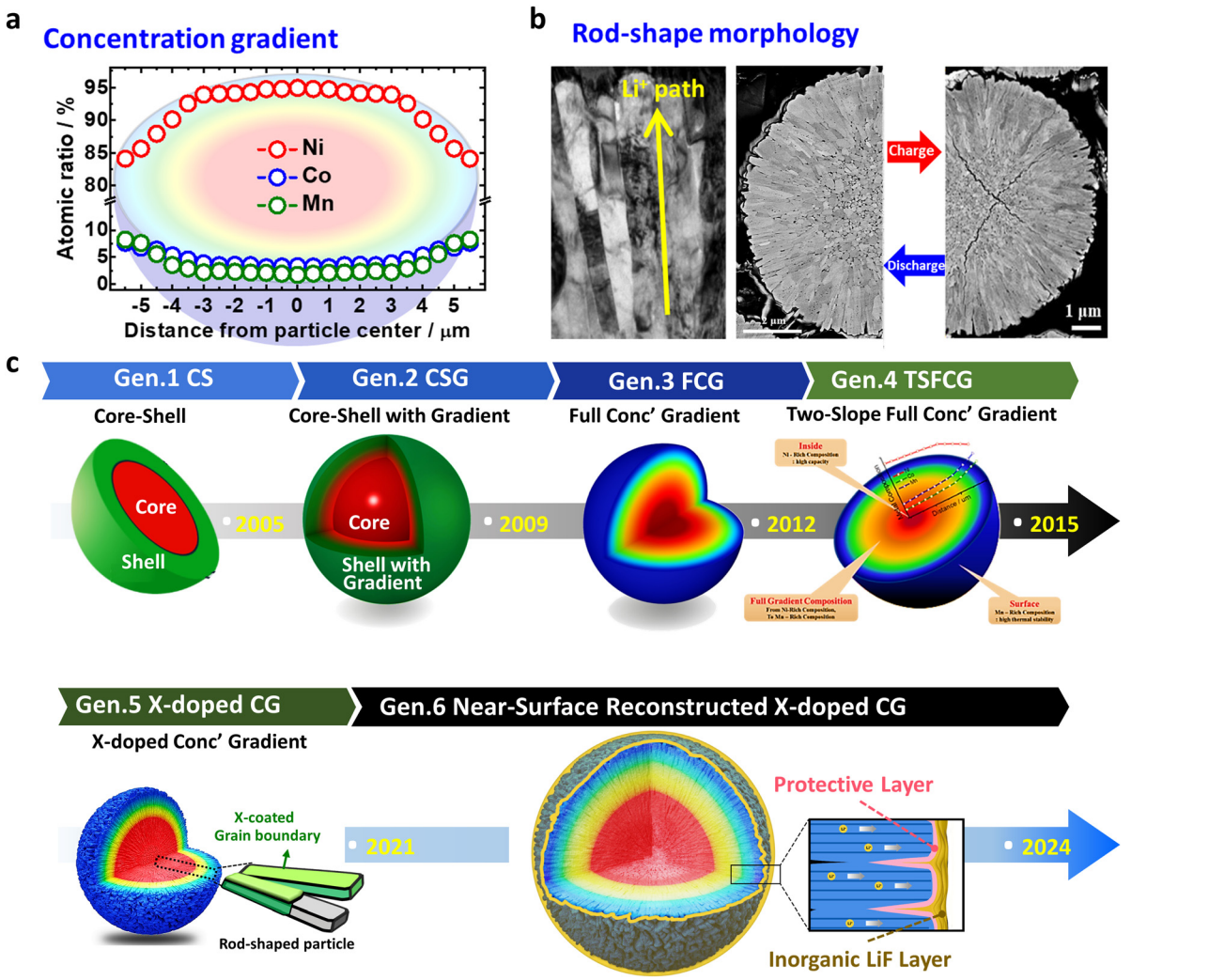

Fig. 17 Concentration gradient cathode materials defined by: (a) Varying TM concentrations throughout the secondary particles, and (b) the rod-shaped morphology of the primary particles. (c) Schematic representation outlining the six generations of concentration gradient-type materials: (i) CS, (ii) CS with gradient, (iii) FCG, (iv) two-slope FCG, (v) X-doped concentration gradient, and (vi) surface-modified concentration gradient. (b) is reproduced with permission,[48,98] Copyright 2013, American Chemical Society and Copyright 2022, Elsevier.

the core to protect the core and develop a cathode material capable of delivering a high capacity and stability.[31,47] As intended, the concentration gradient design has significantly contributed to enhancing the performances of cathode materials. However, a common finding has been the presence of the nano-rod morphology as another unique characteristic of concentration gradient materials. This spatial configuration also has played a significant role in enhancing the performances of cathode materials, as has the compositional design, with its importance becoming more pronounced as the Ni content in cathode materials increases.[50]

In concentration gradient-type materials, the characteristic features are formed at the precursor synthesis stage during co-precipitation, and these features are known to impact the final microstructures of the lithiated gradient cathode materials.[68] At a glance, the precursor primary particles appear as fiber-like bundles with fine boundaries between the subgrains and are oriented in the radial direction of the secondary particle.[160] Structurally, the $Ni(OH)_2$ unit cell exhibits a strong crystallographic texture, where the (001) TM planes are aligned parallel to the direction of the elongated primary particles (Fig. 18a). Upon closer examination, the subgrains contain stacking faults that are indicated by discontinuous lattice fringes in the high-resolution transmission electron microscopy (HRTEM) image and horizontal streaks in the diffraction pattern. This diffraction pattern consists of three sets of overlapping patterns of two mirror images of the [010] zone diffraction pattern from the twinned MnOOH crystals (space group: $P21/c$) and a single [010] zone pattern from $Ni(OH)_2$ (space group: $P\bar{3}m1$). The additional MnOOH phase co-exists with the $Ni(OH)_2$ phase within the primary particles and stems from Mn-enrichment at the surface and the oxidation of Mn^{2+} to Mn^{3+} under a relatively O-rich atmosphere (Fig. 18b).[229,230] This is corroborated by the gradual disappearance of the twinned crystal SAED patterns while approaching the particle center where the Mn fraction progressively decreases in the FCG $Li[Ni_{0.75}Co_{0.10}Mn_{0.15}](OH)_2$. However, the twin phases do not disrupt the layered structure nor the crystallographic texture of the gradient precursors, as the (100) planes of the MnOOH phase are parallel to the (001) planes of the $Ni(OH)_2$ phase, with the difference in the interplanar distance of the two phases being approximately 0.03 nm. They contribute to preserving the nano-rod microstructures of gradient cathodes during the lithiation process. More specifically, during high-temperature lithiation, the precursor microstructure and crystallinity become distorted from adjacent precursor particles to coalesce into randomly oriented, polygonal particles. At the same time, Ni migrates to the vacant Li sites (cation disordering).[79,211] The presence of the twin MnOOH and $Ni(OH)_2$ phases at the precursor stage mitigates this degradation by maintaining the layered planes parallel along the radial direction, while also retarding sintering of the adjacent primary particles.[160] Furthermore, the twins persist in the lithiated cathode (Fig. 18c); however, their density decreases with increasing lithiation temperature (Fig. 18d). This effect is further strengthened by concentration gradients within individual partitioned crystal structures present along the Li-containing (003) lattice in the direction of the columnar primary particles. It is also strengthened by preferential migration of the X-dopants to the grain boundary regions to act as barriers to sintering, as discussed above.[153,204,231]

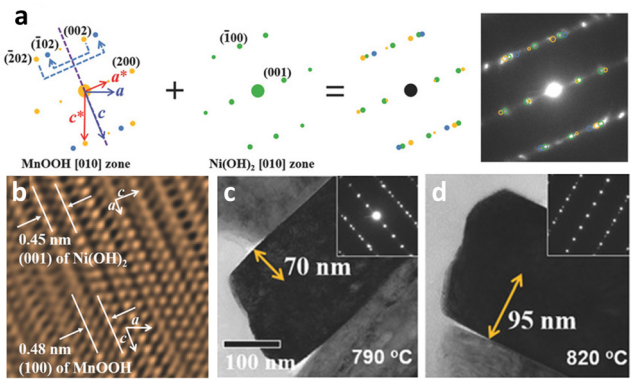

Fig. 18 (a) Combination of the calculated electron diffraction patterns of the MnOOH and $Ni(OH)_2$ phases indexed to reproduce the SAED pattern observed for FCG $Li[Ni_{0.75}Co_{0.10}Mn_{0.15}](OH)_2$. (b) Fourier-filtered image exemplifying the coexistence of the $Ni(OH)_2$ and MnOOH phases with an interplanar distance difference of approximately 0.03 nm. (c) and (d) Bright-field TEM images for the FCG $Li[Ni_{0.75}Co_{0.10}Mn_{0.15}]O_2$ lithiated at 790 and 820 °C, and the corresponding SAED patterns in the insets, showing the twin phase structures. (a)–(d) are reproduced with permission,[160] Copyright 2018, John Wiley and Sons.

3.2. Nano-rods in concentration gradient cathodes

So far, six generations of gradient-type materials exist, namely the CS, CS with gradient, FCG, TSFCG, X-doped concentration gradient, and surface-modified concentration gradient materials, as shown in Fig. 17c. Notably, the nano-rod structure has been observed consistently in the particle morphologies of all six generations of material.

The CS cathode material was the first concentration gradient material introduced in 2005. As a precursor to subsequent generations, the CS $Li[(Ni_{0.8}Co_{0.1}Mn_{0.1})_{0.8}(Ni_{0.5}Mn_{0.5})_{0.2}]O_2$ material consisted of a Mn-rich $Li[Ni_{0.5}Mn_{0.5}]O_2$ shell and a Ni-rich $Li[Ni_{0.8}Co_{0.1}Mn_{0.1}]O_2$ core.[232,233] This system exhibited improved cell performance and thermal stability due to the Mn-rich shell shielding the Ni-rich core to minimize the $Ni^{3+/4+}$-electrolyte parasitic side reactions akin to a coating layer. However, the sudden change in chemical composition and the crystal lattice mismatch at the CS interface resulted in physicochemical separation between the two sections. This was attributed to the volume changes occurring during cycling, eventually leading to rapid electrochemical degradation. To address the shortcomings of the CS material, a concentration gradient connecting the core and the shell was added at their interface to give a CS-with-gradient (CSG) cathode material.[47,184,234] By resolving the shortcomings of the CS cathode, the CSG cathode demonstrated a greatly improved cycle life, with approximately 90% retention being achieved over 1000 cycles in some cases.[49,66] When the concentration gradient and CSG materials were first reported, their morphologies were not discussed in depth, and much of the enhanced performance was attributed to the concentration gradient. It is important to note that the characteristic rod-shaped grain structures and their radial

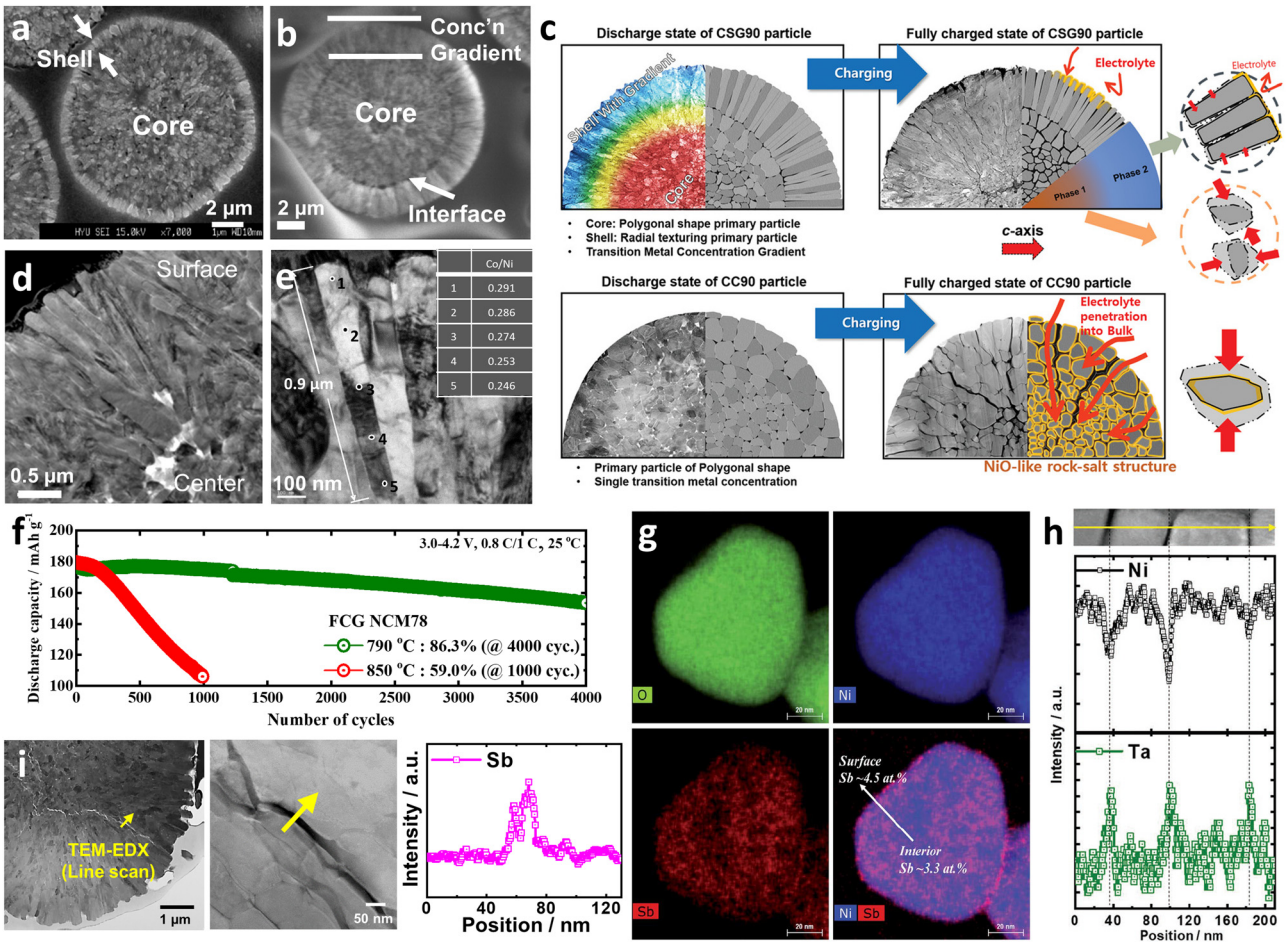

Fig. 19 Cross-sectional SEM images of the (a) CS and (b) CSG materials showing the rod-shaped primary particle morphology in the shell region. (c) Schematic illustration showing the CSG $Li[Ni_{0.90}Co_{0.05}Mn_{0.05}]O_2$ (CSG90, top) and conventional $Li[Ni_{0.90}Co_{0.05}Mn_{0.05}]O_2$ (CC90, bottom) materials in the charged and discharged states. In CSG90, the radially textured nano-rods in the shell prevent microcrack nucleation and propagation, while in CC90, microcracks propagate and allow the electrolyte to penetrate. (d) Cross-sectional TEM image of a FCG $Li[Ni_{0.60}Co_{0.15}Mn_{0.25}]O_2$ particle showing the nano-rod grains at the particle surface. (e) TEM image and EDS data along a single elongated grain of an FCG $Li[Ni_{0.60}Co_{0.15}Mn_{0.25}]O_2$ nano-rod particle, illustrating the concentration gradient within individual grains. (f) Long-term cycling performances of the nano-rod microstructure optimized FCG $Li[Ni_{0.78}Co_{0.10}Mn_{0.12}]O_2$ (calcined at 790 and 850 °C) in pouch-type full cells *versus* the graphite anode. (g) EDS maps of O, Ni, and Sb, along with the overlapped Sb and Ni maps for the Sb-doped $LiNiO_2$ system. (h) TEM-EDS line scan of Ta-doped CS $Li[Ni_{0.94}Co_{0.04}Mn_{0.02}]O_2$ cathode across the grain boundary, showing the concentration spikes of Ta at the grain boundary regions. (i) STEM image of the Sb-doped CSG90 after 1000 cycles, and the corresponding line scan across the microcrack, as indicated by the marked line. (a) and (b) are reproduced with permission,[47] Copyright 2009, Springer Nature. (c) is reproduced with permission,[49] Copyright 2019, John Wiley and Sons. (d) and (e) are reproduced with permission,[48] Copyright 2013, American Chemical Society. (f) is reproduced with permission,[98] Copyright 2022, Elsevier. (g) is reproduced under Creative Commons CC-BY license,[93] Copyright 2020, Royal Society of Chemistry. (h) is reproduced with permission,[153] Copyright 2023, John Wiley and Sons. (i) is reproduced under Creative Commons CC-BY license,[231] Copyright 2021, The Authors, American Chemical Society.

alignment can still be clearly observed in the shell region, as shown in Fig. 19a and b. The efficacy of the nano-rod structure was confirmed by comparing two different CS cathode materials having the same concentration gradient profile but different primary particle morphologies in the shell region, one being the nano-rod structure and the other simply being nano-scale particles.[188] These two different morphologies originated from the disorder of primary particles in a hydroxide precursor, a result of alterations in the synthetic conditions during the co-precipitation reactions. Compared to the nano-scale particles in the shell, the nano-rods more effectively protected the core region due to their dense packing and reduced surface area, even demonstrating improved thermal stability. Subsequent studies into these nano-rod materials have also attributed the performance enhancement to the compactly packed nano-rod structure in the shell, alleviating the stress associated with the taxing H2 → H3 phase transition. Two-dimensional finite element analysis calculations demonstrated that the nano-rod grains in the shell region homogeneously lower the tensile stress in the core region to prevent microcrack nucleation and propagation to the surface, as illustrated in Fig. 19c.[49,66,151] As a result, the capacity fading and impedance increase caused by intergranular boundary surface degradation from direct contact with the infiltrated electrolyte was prevented to enable the CSG cathode to continuously deliver high specific

discharge capacities during long-term cycling (see Fig. 19c), along with the added effect of reducing TM dissolution. More recently, Park *et al.* reported a Co-free CSG $Li[Ni_{0.90}Mn_{0.10}]O_2$ delivering a 79.5% retention rate after 1000 cycles under a fast 3C charge rate. These characteristics were attributed to the nano-rod primary particles preserving the strong crystallographic texture by inducing a homogenous Li distribution, *i.e.*, homogeneity in the SoC, leading to uniform expansion and contraction of the unit cell (Fig. 16a).[132]

The FCG material is the third generation of the CG-type materials. As the name implies, it displays a concentration gradient that extends fully from the particle center to the surface. The first FCG material possessed a chemical composition of $Li[Ni_{0.86}Co_{0.10}Mn_{0.04}]O_2$ at the particle center that graded to a surface composition of $Li[Ni_{0.70}Co_{0.12}Mn_{0.20}]O_2$, thereby representing an average composition of $Li[Ni_{0.75}Co_{0.10}Mn_{0.15}]O_2$.[46,48,98,185] The FCG material is also interesting in that it demonstrated the generation of elongated rod-like primary particles in a radial arrangement with well-developed crystallographic textures near the particle surface for the first time. The aspect ratios of the grains were also maximized because the primary nano-rod particles were crystallographically aligned in the radial direction and had their own concentration gradients within individual grains (Fig. 19d and e).[46,48] Due to the fully extended gradient, the nano-rod region within the secondary particle extended well beyond the shell region seen in the CSG system. To the best of our knowledge, this was the first report of the nano-rod grain structure in layered oxide cathode materials. The combination of these two features in FCG materials greatly reduced the strain and stress to minimize microcrack generation during cycling among the gradient types to deliver enhanced cycling, especially during extended cycles. For example, the nano-rod microstructure of the optimized FCG $Li[Ni_{0.78}Co_{0.10}Mn_{0.12}]O_2$ was found to retain 86.3% of its original discharge capacity over 4000 cycles at a 0.8C/1C charge/discharge rate as shown in Fig. 19f.[98] In addition to the radially parallel nano-rod alignment, the crystal lattice was oriented such that the Li slabs point outward from the center of the particle along the *ab* plane to minimize the tortuosity of inbound or outbound Li^+. Accordingly, a nearly straight diffusion path for Li^+ transport across adjacent primary particles was provided for rapid charge/discharge. This aligned diffusion path was also advantageous during operation at high and low temperatures.[48] The presence of concentration gradients within the elongated rod-shaped primary particles also brings another beneficial effect. Since more Li-ions are (de)intercalated in Ni-rich regions, expansion and contraction of the crystal structure take place, allowing different structural behaviors to be observed within the rod-shaped primary particles depending on the Ni concentrations in the local regions.[36,235,236] The inner region with a relatively higher Ni content contracts to a greater extent than the outer surface region, resulting in the generation of a relative compressive stress on the inner side and tensile stress on the outer side. This differential state of internal stress within the nano-rod particles enhances the mechanical strength against microcracking, much like tempered glass.[99] However, the fully extended concentration gradient limits the Ni content, achieving a Ni content of $\geq$80% difficult. A steeper second gradient was added to the surface to circumvent this limitation and generate a TSFCG material.[50,237,238] The TSFCG displayed similarly distinct nano-rod grain morphologies with large aspect ratios in a radial alignment and delivered excellent electrochemical and thermal properties despite the increased Ni content. It should also be noted that the synthesis process for gradient materials is simple and can easily be substituted for existing manufacturing lines. This is possible since it is only necessary to add a secondary tank that feeds into the original feed tank to generate the chemical concentration gradient.

Despite the numerous advantages of CG-type materials and their revisions through multiple generations, they are not without their challenges. One major challenge is the deterioration occurring during the high-temperature lithiation process, wherein the slope of the pre-designed concentration gradient flattens due to the interdiffusion of TMs. More concerningly, the well-developed, needle-shaped primary particles in the precursors sinter to form the irregular, polygonal primary particles often seen in conventional layered cathode materials in the absence of meticulous and optimized temperature control.[98] However, the addition of high valence state dopants (*e.g.*, Ta^{5+}, Sb^{5+}, W^{5+}, and Nb^{5+}) has effectively reduced the above deterioration during synthesis. Studies have revealed that high valence dopants (denoted as X-dopants) show a strong tendency to segregate to the surface during lithiation, as shown in Fig. 19g and h.[50,153,204,231,239] These X-dopants present at the grain boundary regions act as sintering inhibitors to maintain the characteristic nano-rod shape. They also reduce TM (*i.e.*, Ni, Co, Mn, and Al) interdiffusion to maintain the pre-designed gradient slope more effectively. Consequently, the X-doped concentration gradient materials, as the 5th generation gradient-type materials, resist deterioration during high-temperature calcination and preserve the original physicochemical features.[153,204,231,239] This directly translates into an improved suitability for large-scale industrial synthesis where precise temperature control is difficult. This is possible due to the lower sensitivity of X-doped CG materials to temperature fluctuations. The X-dopants also act as a protective layer to minimize the NiO-like impurity formations when microcracks eventually occur, and consequently, they further increase the electrochemical durability of the concentration gradient material (Fig. 19i). This can be seen in the case of the W-doped FCG $Li[Ni_{0.78}Co_{0.10}Mn_{0.12}]O_2$, which continues to provide 72% of its 0.2C capacity at 5C even after 1000 cycles, leading to preservation of the fast-charge capability.[204,231]

The most recent development in concentration gradient-type materials is the near-surface reconstructed concentration gradient.[240] This material is treated with a Co-dissolved aqueous solution and coated with fluorine to concurrently eliminate any residual Li found in the Ni-enriched layered oxides, ultimately establishing a fluorinated protective layer. As a result, the undesirable gas evolution that leads to cell swelling is suppressed. Coupled with these two features of concentration gradient-type material, the surface-modified concentration gradient $Li[Ni_{0.90}Co_{0.05}Mn_{0.05}]O_2$ material delivered an unprecedented 65% retention over 6000 cycles at 0.8/1C (charge/discharge) in a full-cell

versus the graphite configuration. This result hints at the possibility of a material that can satisfy the energy density, durability, and safety requirements of LIBs in practical applications.

4. Nano-rod cathodes without a concentration gradient

4.1. Nano-rod structure in bulk-type cathodes

As it has been recognized that the presence of the nano-rod structure in concentration gradient materials is a key factor in improving the cathode performance, research has also focused on the development of this nano-rod structure in conventional cathode materials without concentration gradients. As summarized in Table 1, the nano-rod structure is found in various bulk-type cathode materials, such as $LiNiO_2$ (LNO), $Li[Ni_xCo_yAl_{1-x-y}]O_2$ (NCA), $Li[Ni_xCo_yMn_{1-x-y}]O_2$ (NCM), $Li[Ni_xCo_yMn_zAl_{1-x-y-z}]O_2$ (NCMA), $Li[Ni_xCo_{1-x}]O_2$ (NC), and $Li[Ni_xMn_{1-x}]O_2$ (NM), regardless of the composition. In particular, many studies have been conducted to develop nano-rod structures in cathode materials with Ni contents $>80\%$ since the main degradation mechanism of Ni-rich cathodes is microcrack formation. As discussed above, the nano-rod structure can effectively suppress these microcracks.[52,53,57,58,71,76,78–80,97,106,108,130,207,241–243]

Despite the absence of a TM concentration gradient as a driving force to develop nano-rods, it was possible to develop the nano-rod structure in cathode materials without a concentration gradient by controlling the co-precipitation reaction conditions during precursor synthesis or by doping heterogeneous elements into the cathode (Table 1). For this purpose, the precursor should be preferentially grown in the radial direction, and the nano-rod microstructure of the precursor should be passed down to the cathode material during the lithiation process. Spherical particles are synthesized during the preparation of the precursor through the nucleation step and the subsequent particle growth step (Fig. 20a). In the initial stage of precursor synthesis, the TM ions inside the reactor form a complex with ammonia molecules and react with OH^- to generate $TM(OH)_2$ nuclei, wherein nanosized crystal nuclei spontaneously agglomerate into porous microspheres to reduce their surface energies. Subsequently, these microspheres spontaneously aggregate into irregular quasi-spheres during continuous stirring. Ultimately, the nanosheets on the surface of the quasi-sphere grow radially until the interface gradually disappears and the surface becomes compact. During this particle growth stage, the concentration of ammonium, pH conditions, stirring environment, and other synthetic conditions affect particles' continuous and preferential radial growth.[130,244–247] However, during the particle growth process, the newly generated nucleus or microspheres can be adsorbed on the surfaces of the existing quasi-spheres, and they subsequently tightly adhere to one another and grow together. This new microsphere generation and re-agglomeration processes with the existing quasi-spheres play dominant roles in forming the randomly distributed primary particles and the irregular morphology found in the precursor. In contrast, when this re-agglomeration of new nuclei is inhibited and when the preferential radial growth of particles is promoted, a radially oriented microstructure is generated in the precursor. When this precursor is composed of rod-shaped grains and coarsening of the grains is minimized during calcination, the precursor microstructure is passed down to the lithiated cathode, resulting in a nano-rod structure.[79,241]

During high-temperature heat treatment (*i.e.*, calcination) of a mixture of the precursor and the Li source, the morphology and orientation of the primary particles comprising the cathode material can be precisely controlled by doping heterogeneous elements. As shown in Fig. 20b, the shape of the primary particles could be modified depending on the doping element employed (*e.g.*, Mg, Al, Ti, Ta, or Mo). In particular, doping

Table 1 Bulk-type cathode materials with the nano-rod structure

Cathode	Composition	Method for developing the nano-rod morphology	Ref.
LNO	$LiNiO_2$	Doping (Al,Ti)	58
LNO	$LiNiO_2$	Doping (Nb/Ta/Mo)	241
LNO	$LiNiO_2$	Doping (W)	242
NCA	$Li[Ni_{0.885}Co_{0.1}Al_{0.015}]O_2$	Doping (B)	52
NCA	$Li[Ni_{0.855}Co_{0.13}Al_{0.015}]O_2$	Doping (Nb)	76
NCA	$Li[Ni_{0.95}Co_{0.04}Al_{0.01}]O_2$	Doping (W)	97
NCM	$Li[Ni_{0.92}Co_{0.04}Mn_{0.04}]O_2$	Doping (Al)	106
NCM	$Li[Ni_{0.92}Co_{0.05}Mn_{0.03}]O_2$	Doping (B,Na/Mg/Al/Zr)	108
NCM	$Li[Ni_{0.83}Co_{0.06}Mn_{0.11}]O_2$	Doping (Si)	243
NCM	$Li[Ni_{0.94}Co_{0.05}Mn_{0.01}]O_2$	Doping (W)	71
NCM	$Li[Ni_{0.95}Co_{0.025}Mn_{0.025}]O_2$	Doping (W,F)	207
NCM	$Li[Ni_{0.8}Co_{0.1}Mn_{0.1}]O_2$	Controlled co-precipitation synthetic conditions	130
NCM	$Li[Ni_{0.83}Co_{0.05}Mn_{0.12}]O_2$	Controlled co-precipitation synthetic conditions	244
NCM	$Li[Ni_{0.6}Co_{0.2}Mn_{0.2}]O_2$	Controlled co-precipitation synthetic conditions	245
NCM	$Li[Ni_{0.6}Co_{0.2}Mn_{0.2}]O_2$	Controlled co-precipitation synthetic conditions	246
NCM	$Li[Ni_{0.8}Co_{0.1}Mn_{0.1}]O_2$	Controlled co-precipitation synthetic conditions	247
NCMA	$Li[Ni_{0.94}Co_{0.03}Mn_{0.02}Al_{0.01}]O_2$	Doping (Mo)	80
NC	$Li[Ni_{0.96}Co_{0.04}]O_2$	Doping (Mo)	79
NC	$Li[Ni_{0.9}Co_{0.1}]O_2$	Doping (B,Ta)	53
NC	$Li[Ni_{0.9}Co_{0.1}]O_2$	Doping (Ti/Ta/Mo)	57
NM	$Li[Ni_{0.9}Mn_{0.1}]O_2$	Doping (Mo)	78

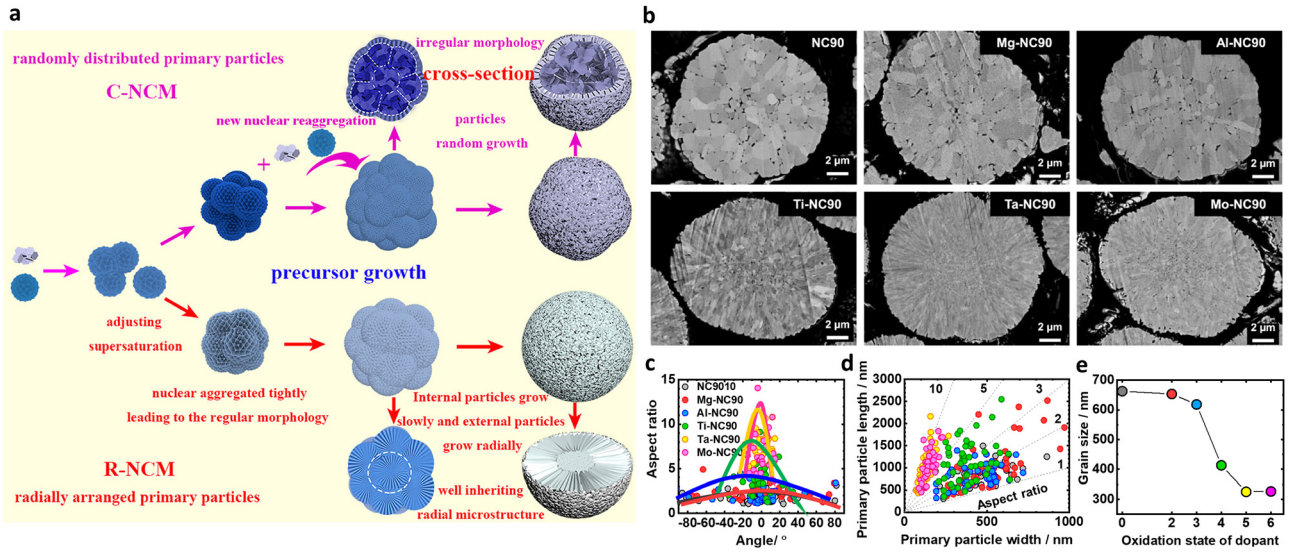

Fig. 20 (a) Schematic diagram illustrating the growth mechanism of precursors with and without the nano-rod structure. (b) Cross-sectional SEM images of cathode particles that show the morphological and orientation differences between the polygonal grains of NC90, Mg-NC90, and Al-NC90, and the elongated grains of Ti-NC90, Ta-NC90, and Mo-NC90. Quantitative analytical results for the cathode grains and their orientations: (c) relationship between the aspect ratio and the relative grain orientation, (d) the aspect ratio (length/width), and (e) the grain size as a function of the oxidation state of dopant. (a) is reproduced with permission,[247] Copyright 2020, American Chemical Society. (b)–(e) are reproduced under Creative Commons CC-BY license,[57] Copyright 2021, Springer Nature.

elements with higher oxidation states led to higher aspect ratios in the primary grains (narrower and longer). In addition, the smaller the grain size, the more radially aligned the orientation of the primary grains tended to be (Fig. 20c–e). Since high-valence elements are segregated at the grain boundaries rather than being incorporated into the crystal structure, they inhibit grain coarsening during calcination and ultimately reduce the size of the primary particles to form nano-rods.[76,79,241,242] Therefore, as the doping amount was increased, the primary grains became increasingly nano-sized in nature.[80,242] Exceptionally, in the case of B doping into the cathode with a layered structure, the (003) facet was dominantly developed, resulting in a rod-shaped primary particle with a particularly high aspect ratio.[52,53] As the content of B was increased, the primary grains became thinner and longer, resulting in rod-shaped primary grains with an aspect ratio of >10, wherein crack growth was further suppressed.[54] Likewise, the primary particle morphology modification has been achieved by controlling the types and contents of the doping elements. Since the aspect ratio and size of the primary particles can be effectively tuned by doping, the cathode microstructure has been successfully optimized to effectively distribute the strain induced by anisotropic lattice volume changes, thereby suppressing microcrack formation and enhancing the electrochemical performance.[52,248]

4.2. Importance of the hydroxide precursor microstructure

All cathode materials with a layered structure that are currently used in LIBs are synthesized by mixing a hydroxide precursor with LiOH and calcinating the mixture at high temperatures. During calcination, the hydroxide precursor undergoes crystal structural changes (from the $P\bar{3}m1$ to the $R\bar{3}m$ structure) as it transforms into a lithiated oxide.[249] Simultaneously, the fine grains of the precursor undergo a morphological change through coarsening to become the primary particles of the cathode material.[79,211,241] Therefore, as shown in Fig. 21a, if the grains comprising the precursor are randomly oriented in a polygonal shape, the primary particles of the cathode material prepared from such a precursor will also be randomly oriented in a polygonal shape. Conversely, if the grains comprising the precursor are radially oriented in a rod-shaped form, the primary particles of the cathode material prepared from such a precursor will also have a radially oriented rod-shaped morphology. Therefore, the precursor's microstructure plays a crucial role in determining whether or not the microstructure of the cathode material contains a TM concentration gradient. To investigate the inheritance of the precursor microstructure by the cathode, a precursor with randomly oriented grains was synthesized by suppressing the uniform growth of the precursor through the intermittent pumping of solutions during the co-precipitation reaction (Fig. 21b).[68] When the cathode material was prepared using such a precursor, the grains were randomly coarsened during the calcination process, resulting in a cathode material composed of randomly oriented polygonal primary grains, as shown in Fig. 21c. However, when the cathode material was prepared using a precursor whose grains were rod-shaped and radially oriented (Fig. 21d), the resulting cathode material also exhibited a well-developed radially oriented nano-rod structure (Fig. 21e). Even when various methods are used to induce the nano-rod structure, the development of this structure in the precursor is a prerequisite for the eventual development of a nano-rod structure in the cathode material. Zhou *et al.*[246] also reported that the development of the nano-rod structure in a

cathode material is dependent on the microstructure of the precursor (Fig. 21f–i). Since the microstructure of the cathode material is inherited from the precursor, this structure must be developed in the precursor *via* the co-precipitation approach. In other words, the presence of a well-developed nano-rod structure in the cathode material indicates that the rod-like microstructure of the precursor was maintained during the calcination process. In addition to the hydroxide precursor method, cathode materials can also be synthesized without the requirement for a precursor, such as *via* the sol–gel and solid-state reaction approaches. More specifically, $LiMO_2$ cathodes can be prepared using the sol–gel method, wherein acetate and nitrate sources, such as $Li(CH_3COO)$, $Mn(CH_3COO)_2{\cdot}4H_2O$, $Ni(CH_3COO)_2{\cdot}4H_2O$, and $Co(NO_3)_2{\cdot}6H_2O$, are dissolved in water, and citric acid is added to form a gel. After subsequent drying and grinding of the gel, it is calcined to give the desired cathode material.[250] Regarding the solid-state reaction approach, $LiMO_2$ cathodes can be prepared by mixing oxide sources, such as NiO, Co_3O_4, and MnO_2, with LiOH and subsequent calcination at high temperatures.[251] Although these methods can yield cathode materials without the requirement for a precursor, they produce microstructures consisting of several large agglomerated grains, which cannot develop the nano-rod structure (Fig. 21j and k).[250,251] Furthermore, the cathode particles synthesized using these methods are sub-micron in size, resulting in a lower tap density and volumetric energy density compared to cathodes with spherical secondary particles measuring >10 μm. Therefore, the nano-rod structure can only be developed through the lithiation of precursors synthesized *via* a co-precipitation reaction, which is currently a standard method in this field. These studies clearly emphasize the importance of the precursor microstructure in the development of cathode materials with nano-rod structures.

4.3. Mechanisms of nano-rod generation using the doping approach

The primary particle morphology of a cathode material can be further engineered by introducing dopants during the lithiation of the nano-rod precursors. The morphology of the primary particles differs depending on the dopant type, and the resulting size and shape can vary depending on the type and amount

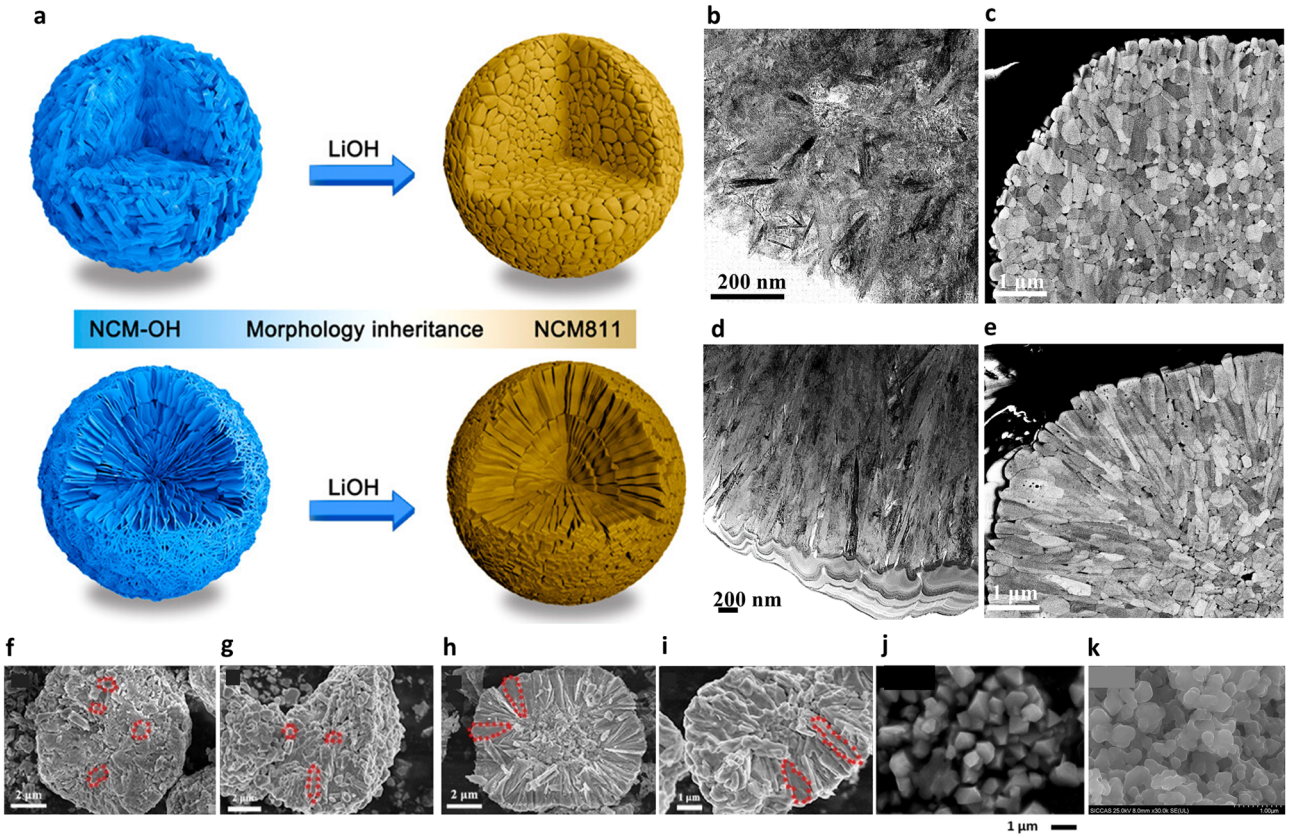

Fig. 21 (a) Schematic representation showing inheritance of the precursor microstructure by the cathode material. (b) TEM image of a precursor with randomly oriented grains and (c) cross-sectional SEM image of the cathode microstructure synthesized using this precursor. (d) TEM image of a precursor with radially oriented grains and (e) cross-sectional SEM image of the cathode microstructure synthesized using this precursor. Cross-sectional SEM images of (f) a precursor without the nano-rod structure and (g) the cathode synthesized using this precursor. Cross-sectional SEM images of (h) a precursor with the nano-rod structure and (i) the cathode synthesized using this precursor. SEM images of the cathodes synthesized using (j) the sol–gel method and (k) the solid state reaction method. (a) is reproduced with permission,[109] Copyright 2023 American Chemical Society. (b)–(e) are reproduced with permission,[68] Copyright 2021, Royal Society of Chemistry. (f)–(i) are reproduced with permission,[246] Copyright 2016, Elsevier. (j) is reproduced with permission,[250] Copyright 2022, American Chemical Society. (k) is reproduced under Creative Commons CC-BY license,[251] Copyright 2017, Royal Society of Chemistry.

of dopant. In this context, Sun *et al.*[51,52] reported that B doping on NCA or NCM cathodes lowers the surface energy of certain facets during lithiation, forcing the primary particles to grow into thin elongated shapes enclosed on the sides by the (003) planes (Fig. 22a–c). To verify the surface energy modification caused by boron doping, the (003), (012), (014), and (100) surface energies of pristine $LiNi_{0.92}Co_{0.04}Al_{0.04}O_2$ and B-doped $LiB_{0.02}Ni_{0.90}Co_{0.04}Al_{0.04}O_2$ cathodes were calculated using the density functional theory approach.[52] Fig. 22d shows the surface ene rgy plots $\gamma(\Delta\mu_{Li})$ of the pristine $LiNi_{0.92}Co_{0.04}Al_{0.04}O_2$ and B-doped $LiNi_{0.90}Co_{0.04}Al_{0.04}$ $B_{0.02}O_2$ surfaces. $\Delta\mu_{Li}$ was referenced to the total energy per atom of a metal Li reservoir, and the low and high values of $\Delta\mu_{Li}$ represent Li-poor and -rich environments, respectively. For low Li chemical potential values of $\Delta\mu_{Li} \leq -3.67$ eV, the pristine $LiNi_{0.92}Co_{0.04}Al_{0.04}O_2$ (003) surface was found to be the most favorable, while for values of -3.67 eV $\leq \Delta\mu_{Li} \leq -2.85$ eV, the B-doped $LiB_{0.02}Ni_{0.90}Co_{0.04}$-$Al_{0.04}O_2$ (104) surface was stabilized. However, for cases where -2.85 eV $\leq \Delta\mu_{Li}$, the B-doped $LiNi_{0.90}Co_{0.04}Al_{0.04}$ $B_{0.02}O_2$ (003) surface was the most favorable. As lithiation of the hydroxide precursor was performed using excess Li, it is likely that the surface of the B-doped cathode was enriched in Li and that the B atoms preferentially lowered the energy of the (003) surface. Therefore, through B doping, the surface energy was engineered to maximize the (003) facet, and consequently, rod-shaped primary particles with high aspect ratios were achieved.

If the precursor with a nano-rod structure is lithiated at a low calcination temperature, the nano-rod structure is well preserved in the cathode material by minimizing grain coarsening. However, the electrochemical performance of the cathode is poor due to its low crystallinity.[211] However, during calcination at higher temperatures or for longer durations, the crystallinity is enhanced, and the precursor grains are coarsened in a random direction, resulting in larger primary grains and random polygonal shapes.[79,211,241] High-valence elements such as Sb, Nb, Ta, Mo, and W impede the coarsening of primary particles by segregating at the particle boundaries, thereby preserving the microstructure until the cathode attains an optimal crystal

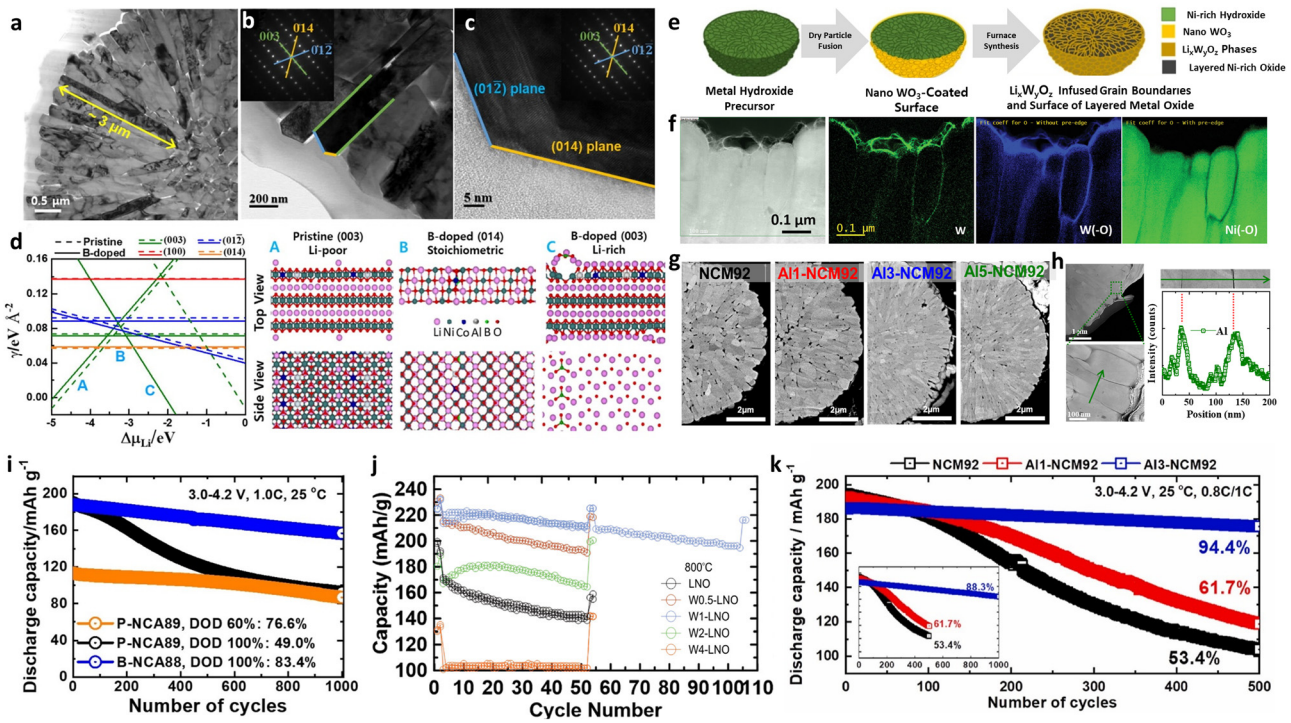

Fig. 22 (a) and (b) Bright-field TEM images of the as-synthesized particles showing the B-NCA88 microstructure. (c) HRTEM images of the magnified region in part (b). (d) Surface energies of the pristine and B-doped $LiNi_{0.9}Co_{0.04}Al_{0.04}O_2$ (003), (012), (100), and (104) surfaces as a function of the chemical potential of Li ($\Delta\mu_{Li}$) referenced to bulk metal Li (left). The solid and dashed lines represent the B-doped and pristine surfaces, respectively. The most favorable surface structures at different values of $\Delta\mu_{Li}$ (right), labeled as A: pristine (003)-Li poor, B: B-doped (014)-stoichiometric, and C: B-doped (003)-Li rich in the surface energy plot. (e) Schematic illustrations of the secondary particle cross-sections at various stages of the W-modification procedure. (f) TEM image, EELS mapping of the W signal, MLLS fitting of oxygen without pre-edge spectra, and MLLS fitting of oxygen with pre-edge spectra for the W1-LNO sample where the precursor was coated with WO_3 *via* the dry particle fusion approach. (g) Cross-sectional SEM images of the NCM92, Al1-NCM92, Al3-NCM92, and Al5-NCM92 particles. (h) TEM–EDX elemental line scan results for the 4 mol% Al-doped NCA cathode analyzed across the grain boundaries. (i) Long-term cycling performances of the P-NCA89 cathodes cycled at DoD 60 and 100%, and the B-NCA88 cathode cycled at DoD 100%. (j) Electrochemical cycling performances of LNO, W0.5-LNO, W1-LNO, W2-LNO, and W4-LNO synthesized at 800 °C (2 cycles at C/20, 50 cycles at C/5, and 2 cycles at C/20). (k) Long-term cycling performances of the NCM92, Al1-NCM92, and Al3-NCM92 cathodes in pouch-type full cells containing graphite anodes. (a)–(d) and (i) are reproduced with permission,[52] Copyright 2020, Elsevier. (e) is reproduced under Creative Commons CC-BY license,[252] Copyright 2021, IOP Publishing. (f) and (j) are reproduced with permission,[242] Copyright 2021, John Wiley and Sons. (g) and (k) are reproduced with permission,[106] Copyright 2023, Elsevier. (h) is reproduced with permission,[68] Copyright 2021, Royal Society of Chemistry.

structure.[79,241,242] These high valence elements are likely insoluble in the crystal structure, resulting in accumulation along the interparticle boundaries. In this context, Dahn *et al.*[242,252] reported that the W introduced during lithiation of the precursor is concentrated in the form of $Li_xW_yO_z$ phases on the surfaces of the secondary particles and in the grain boundaries between the primary particles after calcination (Fig. 22e and f). The presence of these phases limits grain coarsening in polycrystalline materials, and the resulting smaller primary particles lead to an enhanced resistance to the microcrack formation induced by the anisotropic stress during the (de)intercalation of Li^+ ions. Furthermore, the $Li_xW_yO_z$ phases can act as a glue between the primary particles. Hence, a lesser degree of microcracking was observed in the W-doped cathode materials.[242,252] Similarly, Nb, Ta, and Mo form $LiNbO_3$, $LiTaO_3$, Li_2MoO_4 compounds during lithiation, which retard coarsening by segregating at the grain boundaries.[241] Therefore, by doping with high-valence elements, the crystallinity can be maximized without sacrificing the integrity of the microstructure, resulting in a wide range of possible calcination temperatures and enhanced electrochemical performances compared to those of the pristine cathodes. Furthermore, since solubility differences also exist in the crystal structure depending on the type of dopant, elements such as Mo (which remain as lithiated oxides at high temperatures) maintain the microstructure and electrochemical performance of the cathode at higher temperatures than is possible for Ta or Nb.[79,241] Since these high valence elements develop a nano-rod structure through a mechanism that maintains the microstructure of the precursor during lithiation, the development of a nano-rod structure in the precursor is clearly a prerequisite.

Elements such as Al, which are soluble in the crystal structure due to their low atomic weights, can be sufficiently incorporated into the lattice structure at concentrations of up to 2 mol%. However, introducing excessive doping beyond the dopant solubility causes segregation at the grain boundaries (Fig. 22g and h).[68,106] As in the case of high-valence element doping, segregation by such excessive doping suppresses the coarsening of primary particles by pinning the grain boundary, thereby maintaining the microstructure of the precursor after lithiation. Therefore, developing a nano-rod structure in the precursor is also a prerequisite for inducing the nano-rod structure through such excess doping. As excess doping increases, a greater degree of segregation occurs, and the precursor microstructure can be more effectively maintained, generating nano-sized primary particles.[68,106] However, the reversible capacity decreases as the content of electrochemically inactive elements increases, and the excessive segregation of dopants can act as an impurity. Therefore, the optimum excess doping level in the case of Al has been defined as 3 mol%.[106] Conventionally, the doping strategy considers only incorporating additional elements into the bulk structure of the cathode in terms of fortifying the crystal structure. However, the ability to engineer a cathode material's crystal structure and microstructure through methods such as excessive doping has made it possible to maximize long-term cycling stabilities, especially for Ni-rich cathodes that suffer from microcrack-induced capacity fading.

The above results indicate that doping is a simple and effective method to induce nano-rod formation *via* various mechanisms (*e.g.*, surface energy modification and suppression of coarsening *via* the segregation of doping elements). In addition, it is necessary to develop a nano-rod structure in the precursor stage to achieve the nano-rod structure using these doping methods. As the radial alignment of thin and long particles is effective in preventing microcracks, which are the main culprit of the degradation of Ni-rich cathodes, cathodes with a nano-rod structure developed through doping tend to exhibit enhanced cycling stabilities compared to those without doping (Fig. 22i–k). Therefore, multi-stage engineering, from precursor synthesis to morphological control through doping, is important for developing the nano-rod structure in cathode materials and enhancing their respective electrochemical performances.

5. Challenges and advances of the nano-rod structure

5.1. Considerations during nano-rod cathode preparation

The performances of Ni-rich layered cathode materials greatly depend on various fundamental properties, such as crystallinity, grain morphology, and surface conditions, which are determined during the synthetic process. Hence, it is crucial to understand the relationship between the synthetic conditions and the cathode material structure to optimize the performance of the nano-rod cathode material. In this context, it is known that Ni-rich cathode materials are produced in a two-step process involving the synthesis of the hydroxide precursor and subsequent calcination of this precursor in the presence of a Li source. While various reaction systems could be considered, a hydroxide-type precursor is favored due to its ease of mass production and ability to provide template structures for the final cathode product. Ultimately, this facilitates the development of a desirable crystallinity, Li pathway, and grain alignment.[253] The calcination process is also important since it should preserve the desired characteristics of the hydroxide precursors even after heat treatment at high temperatures (Fig. 23a).[79,231,241]

As the temperature rises during calcination, Li ions are inserted into the hydroxide precursor with a $P\bar{3}m1$ space group structure, forming an intermediate state where Li and the TMs are randomly arranged.[249] At higher temperatures, Li and the TMs form alternating layers, accompanied by changes in the chemical states of the TMs. This process forms a layered structure with an $R\bar{3}m$ space group. In addition, various crystal structural features, such as Li/TM intermixing and the Li–slab distance, are known to significantly influence the mobility of the Li ions, affecting overall performance. Furthermore, it has been reported that the skeletal structure and crystallinity of a cathode material are predominantly influenced by both the peak temperature during the calcination step and the duration of this elevated temperature.[80,211] An insufficient thermal energy cannot induce adequate Li/TM ordering, while excessive heat and prolonged exposure to such heat can lead to the loss of Li and O from the crystal structure, resulting in increased

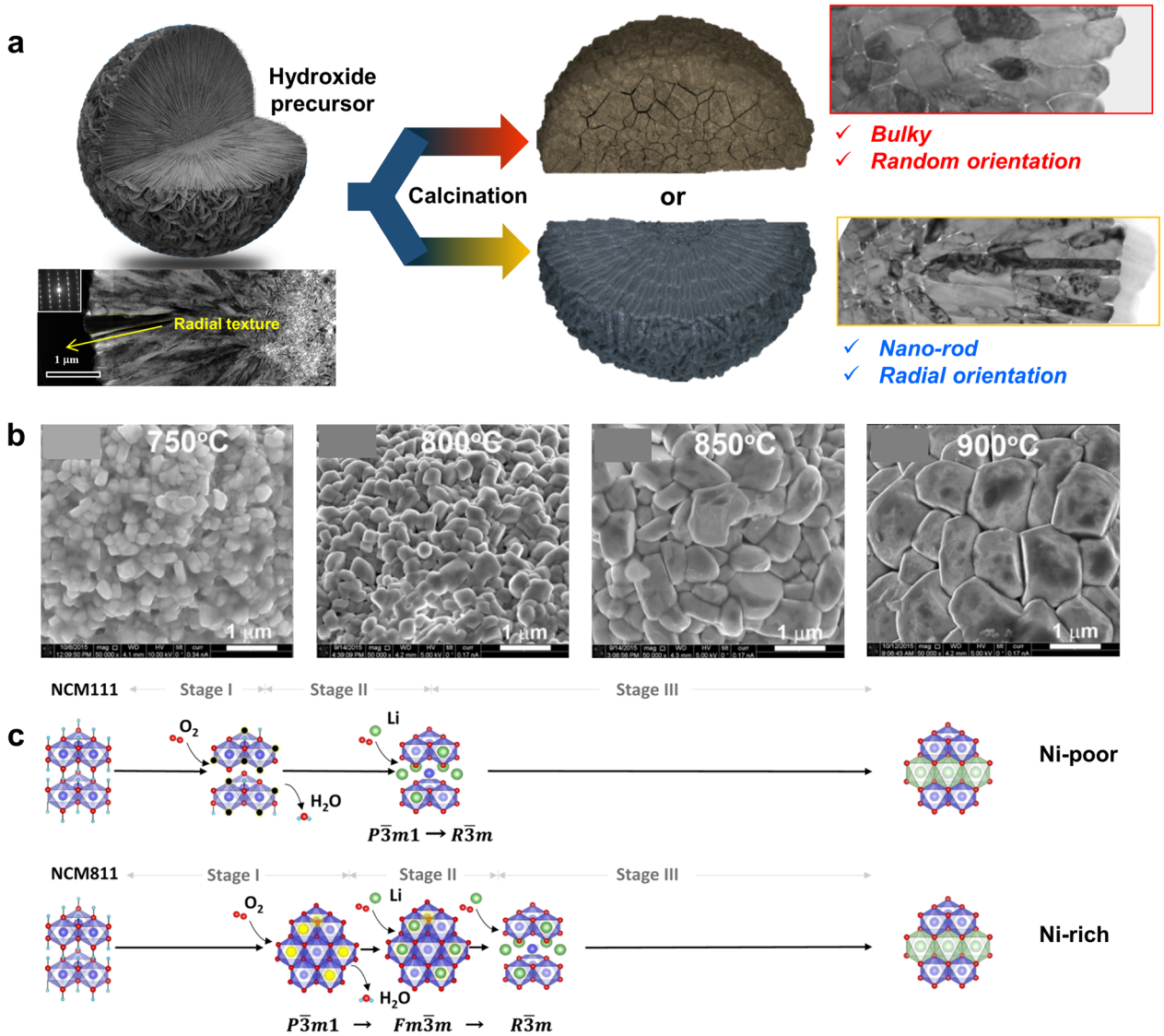

Fig. 23 (a) Schematic representation of the microstructure of the cathode material, which varies depending on the sintering conditions. (b) Variation in the evolution of the primary particle morphology under different heat treatment temperatures. (c) Variation in the crystal structural evolution depending on the chemical composition during the sintering process. (b) is reproduced with permission,[211] Copyright 2018, Elsevier. (c) Reproduced under Creative Commons CC-BY license,[249] Copyright 2023, American Chemical Society.

disordering.[211] Therefore, it is crucial to establish an optimal sintering temperature to ensure a sufficiently high crystallinity for any specific composition.

The electrochemical properties of cathode materials are significantly influenced by their microstructures, surface areas, pore distributions, grain sizes, and Li-ion pathways. The hydroxide precursors, typically synthesized *via* the co-precipitation approach, generate secondary particles through the aggregation of nano-scale primary particles. During calcination, the insertion of Li ions into the structure induces volume expansion of the primary particles.[204] While the size of the secondary particles is relatively less sensitive to the calcination temperature, the primary particles coarsen through the fusion of neighboring particles, resulting in grain growth at certain calcination temperatures. In this context, Zheng *et al.*[211] investigated the effect of the calcination temperature on Ni-rich cathode materials. They found that the primary particle size increased with an increasing calcination temperature, and the resulting cathode performance was directly related to the primary particle size (Fig. 23b). Notably, changes in the shape, size, and orientation of the primary particles during calcination play a crucial role in determining the morphology of the cathode material. More specifically, the size and shape of the primary particles not only determine the exposed surface area on the outside of the secondary particles but also influence the reconstruction of the surface structure and the degree of residual Li formation depending on the calcination conditions (*i.e.*, O_2 flow, pressure, and cooling rate).[254]

A Ni-rich cathode material can exhibit its peak performance when synthesized under optimal conditions. However, one of

the challenges associated with optimizing the performances of such materials is the complex synthetic conditions that become more intricate as the Ni content rises. For example, the optimal calcination temperature decreases and its range narrows as the degree of O loss becomes more prevalent with the enrichment of Ni. Kleiner *et al.*[249] reported that Ni-rich and Ni-poor cathode materials underwent different structural reaction mechanisms (Fig. 23c). In contrast to Ni-poor hydroxide precursors, which maintain a stable layered scaffold upon calcination, Ni-rich precursors transition through a rock-salt structure to produce an $R\bar{3}m$ layered structure. This transformation necessitates precise temperature control to avoid incomplete phase transformation and structural disorder. Additionally, compositional changes in the Co or Mn ions influence structural evolution.[255,256] Each TM ion exhibits a different preference for oxidation during the calcination process, thereby affecting the breakage or reconstruction of NiO_6 octahedra. Different magnetic and electronic interactions among the constituent cations in the framework, which can be imparted by tuning the extent of Li/Ni exchange, further determine the order of the local structure.[255] Many comprehensive studies based on the use of advanced analytical tools have provided insights into the crystalline and morphological changes taking place during the calcination of conventional layered cathode materials. However, intriguingly, adding a small amount of dopant leads to entirely different transformations in the cathode material during sintering, posing a challenge in performance optimization in nano-rod cathode materials.

As discussed above, the addition of dopants can alter the optimal calcination temperature. For example, it has been reported that when a small amount of W is doped into the LNO material with an optimal calcination temperature of 650 °C, the optimal calcination temperature increases by >100 °C.[257] Notably, at temperatures far beyond the optimal range, numerous defects are generated in the pure $LiNiO_2$ cathode material due to O loss, and the layered structure is also collapsed. However, adding small amounts of W during the sintering process maintained the layered structure even at high temperatures and enhanced the structural stability for long-term cycling. In this context, Bianchini *et al.*[81] observed that the incorporation of W into an LNO cathode material suppressed the occupancy of Ni on the Li sites, indicating a higher structural stability at elevated calcination temperatures. They suggested that the doping-induced increase in the calcination temperature may be attributed to the formation of trace amounts of rock-salt-like impurity structures. This, in turn, was potentially caused by the high valence state of W^{6+}, leading to the migration of Ni^{2+} to the Li sites.

A similar behavior was observed in Mo-doped NCMA94 materials during variable-temperature X-ray diffraction (XRD) measurements (Fig. 24a).[80] Upon increasing the temperature during calcination, the (003)/(104) peak ratio of the pristine NCMA94 cathode rapidly increased, the degree of cation mixing decreased, and both parameters were found to level off at 680 °C. However, when the temperature was further elevated to 770 °C after a 10 h holding period at 680 °C, the crystalline parameters of the cathode deteriorated, resulting in the collapse of its $R\bar{3}m$ layered structure in the presence of such an excessive thermal energy. In contrast, for the NCMA94 cathode containing 1.5 mol% MoO_3 doping, the optimal crystal structure formed at 770 °C rather than 680 °C, displaying an even higher (003)/(104) peak ratio than that of the pristine cathode at 680 °C. These results confirm that even trace amounts of MoO_3 significantly influence the crystallinity of NCMA94 and increase the optimal lithiation temperature. Interestingly, the magnitude of the shift depends on the amount of Mo, such that four cathode materials with varying doping levels exhibit their optimal crystallinities when calcined at different temperatures. The impact of the Mo doping content also includes morphological refinements, which become increasingly more pronounced at higher Mo concentrations (Fig. 24b).[80] Moreover, a higher degree of Mo doping suppresses primary particle growth over a wider temperature range, likely due to kinetic or thermodynamic effects hindering grain boundary diffusion by solute accumulation.[79,242,252] These variations in the material crystallinity and morphology distinctly affect its electrochemical performance. The left panel in Fig. 24c shows the relationship between the crystallinity and discharge capacity. Notably, the discharge capacities of the cathodes calcined at different temperatures show a roughly similar tendency to the variations in their $c/3a$ ratio, with the exception of the pristine cathode. On the other hand, the right panel in Fig. 24c shows the relationship between the primary particle size and capacity retention. While the capacity retention of the pristine NCMA94 cathode decreases with an increasing lithiation temperature, that of the Mo-doped NCMA94 cathode remained stable over a wide temperature range. This trend suggests that capacity retention is inversely related to the average primary particle size of the cathode materials. However, an excess Mo doping of 2 mol% compromises the initial capacity while providing limited benefits in terms of capacity retention. It was therefore suggested that the optimized Mo-doped NCMA94 cathode could be synthesized using 1 mol% Mo doping and calcination at 750 °C. The results showed that determining the optimal synthetic conditions for tuning the electrochemical performance (*i.e.*, doping amount, calcination temperature, and calcination time) requires a trial-and-error approach. This process depends on the compositional and morphological features of precursors/cathodes and the characteristics of the dopants, thereby rendering the development of high-quality nano-rod cathode materials a significant challenge.

Various dopants have been applied and tested in Ni-rich cathode materials; however, their properties and roles require further clarification. Significant efforts have been aimed at categorizing and understanding the characteristics of various types of dopants when introduced into Ni-rich layered cathode materials. For example, Sun *et al.*[53,57] experimentally evaluated the electrochemical, morphological, and structural characteristics of dopants and categorized them according to the extent to which doping altered the physical properties of the material and increased the cathode cycle life (Fig. 24d). They determined that dopants with higher oxidation states are more effective at increasing the stability of the cathode material, as a higher oxidation state tends to induce a highly oriented elongated grain microstructure and generates a cation-ordered superlattice

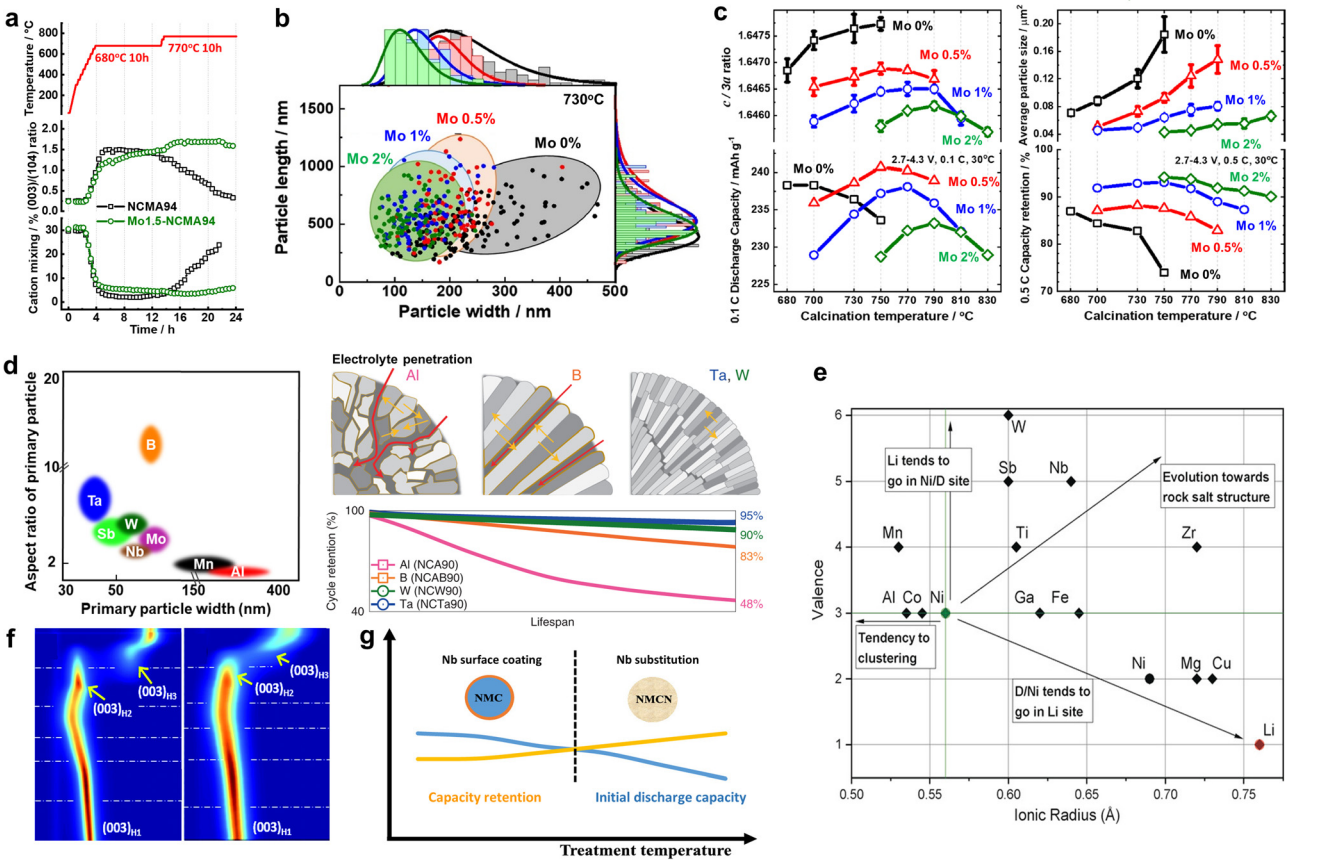

Fig. 24 Comparison of (a) the crystallinity changes during the sintering process, and (b) the primary particle size depending on the doping content. (c) Correlation between the physicochemical properties and the electrochemical performances of cathode materials with different doping amount. (d) Map of the primary particle morphology and the electrochemical performance with variation in the oxidation state of the dopant. (e) Dopant categorization as a function of the ionic size and valence. (f) Contour plots of the (003) reflections of the LNO (left) and W-1 LNO (right) materials analysed by operando XRD. (g) Controversy regarding the presence of dopants, *i.e.*, whether they exist only at grain boundaries, substitute within the crystal structure, or coexist on both sides. (a)–(c) are reproduced with permission,[80] Copyright 2023, Elsevier. (d) is reproduced with permission,[53] Copyright 2020, Springer Nature. (e) is reproduced with permission,[258] Copyright 2018, John Wiley and Sons. (f) is reproduced with permission,[257] Copyright 2019, Royal Society of Chemistry. (g) is reproduced with permission,[259] Copyright 2021, American Chemical Society.

atomic arrangement. In addition, their results highlighted the close relationship between the resulting electrochemical performance and the micro- and atomic-level structures formed by the dopants. In another study, Janek *et al.*[258] summarized previous research carried out on LNO cathode materials, categorizing the characteristics of the dopants based on their oxidation states and ion sizes (Fig. 24e). Their summary indicated that dopants with smaller cation sizes tend to lead to non-uniform doping due to their clustering inside the structure, resulting in a low tolerance of the doping concentration. In contrast, larger dopants can be easily accommodated into the structure. They also concluded that large dopants with low oxidation states tend to occupy Li sites, while those with high oxidation states induce the formation of a rock-salt structure. Furthermore, Cho *et al.*[260] used first-principles calculations to predict the trends induced by dopants, such as phase instability, Li–Ni exchange, Ni segregation, lattice distortion, and oxygen evolution. They noted a strong site preference depending on the Mn and Co concentration ratio, suggesting multicomponent doping strategies are required.

The mechanisms by which dopants are incorporated into cathode materials during synthesis have yet to be precisely elucidated. This leads to debates over whether dopants diffuse into the structure, substitute Li or TM sites, or segregate at the grain boundaries as solutes. Indeed, some dopants have been shown to refine the microstructure by segregating at the grain boundaries, thereby delaying the coalescence of the primary particles. This raises the possibility that the added dopants may not substitute Ni or Li but that they instead exist only at the grain boundaries and surfaces (Fig. 22e and f).[242] To date, numerous cases of dopants distributed at grain boundaries have been captured by electron energy loss spectroscopy (EELS) and energy-dispersive X-ray spectroscopy (EDS).[90,241,242,261,262] On the other hand, tracking changes in the lattice parameters or the Li–Ni exchange degree *via* XRD is a standard method for determining whether dopants have diffused into a crystal structure or not. As shown in Fig. 24f, the phase transition behavior clearly changed during W doping, wherein the wholly separated H2 and H3 phases of the pristine LNO cathode

transformed to exhibit a continuous transition, as indicated by the (003) shift. However, obtaining clear evidence using solely XRD for NCM/NCA cathodes with a Ni content <95% is challenging in most cases. This can be attributed to the fact that their phase transitions are not as abrupt as those of LNO, owing to the stabilization effects imparted by Co, Mn, and Al. In addition, the effective doping amounts are mostly restricted to <2 mol%, which leads to extremely subtle changes. It has also been reported that the crystal structural information varies depending on the synthetic conditions and doping amount employed.[80,261] Currently, the most plausible explanation is that some dopants are inserted into the crystal structure while the rest remain at the grain boundaries (Fig. 24g).[259] However, due to the complexity of the system, further multidimensional research into the doping mechanisms is required to promote the development of high-performance cathode materials.

5.2. Highly Ni-rich concentration gradient nano-rod cathodes

Doping is generally considered the most effective method for enhancing the performances of Ni-rich cathode materials. However, it is not a panacea, necessitating careful consideration of various combinations, doping methods, and dopant types/amounts. This section introduces recent advancements in doping strategies.

Most degradation in Ni-rich cathode materials originates from the surface, indicating the necessity to protect the cathode material from microcracks and minimize the exposed surface area that comes into contact with the electrolyte. Ideally, if microcracks do not form, the electrolyte only attacks the outer surface of the secondary particles. In this regard, concentration gradient cathode materials possess significant advantages by minimizing the Ni content on the surface to reduce side reactions with the electrolyte.[46,47,99,224–228] More specifically, concentration gradient materials composed of a hybrid structure (*i.e.*, a high Ni content in the core and a low Ni content on the surface) suppress the formation of microcracks by creating a non-uniform spatial distribution of microstrain within the cathode particle. This structure resembles tempered glass, enhancing resistance to microcracking during electrochemical operations.[99] In the absence of microcracking, the lower Ni content on the surface of a concentration gradient cathode delays parasitic attack by the electrolyte, leading to exceptional long-term stability. However, despite increasing the demand for concentration gradient cathode materials with higher Ni contents and energy densities, limited spatial flexibility exists for implementing concentration gradients within the precursor.[153] Consequently, the thickness of the shell gradually decreases, and the difference in concentration between the interior and the exterior is reduced, leading to issues resembling those of materials without concentration gradients (Fig. 25a). Furthermore, challenges are also associated with the use of thin concentration gradient layers that are unable to withstand high sintering temperatures due to interdiffusion between TM ions.[98,153,231] Therefore, the development of concentration gradient cathode materials containing >90% Ni poses significant challenges. Drawing inspiration from high-entropy alloys,

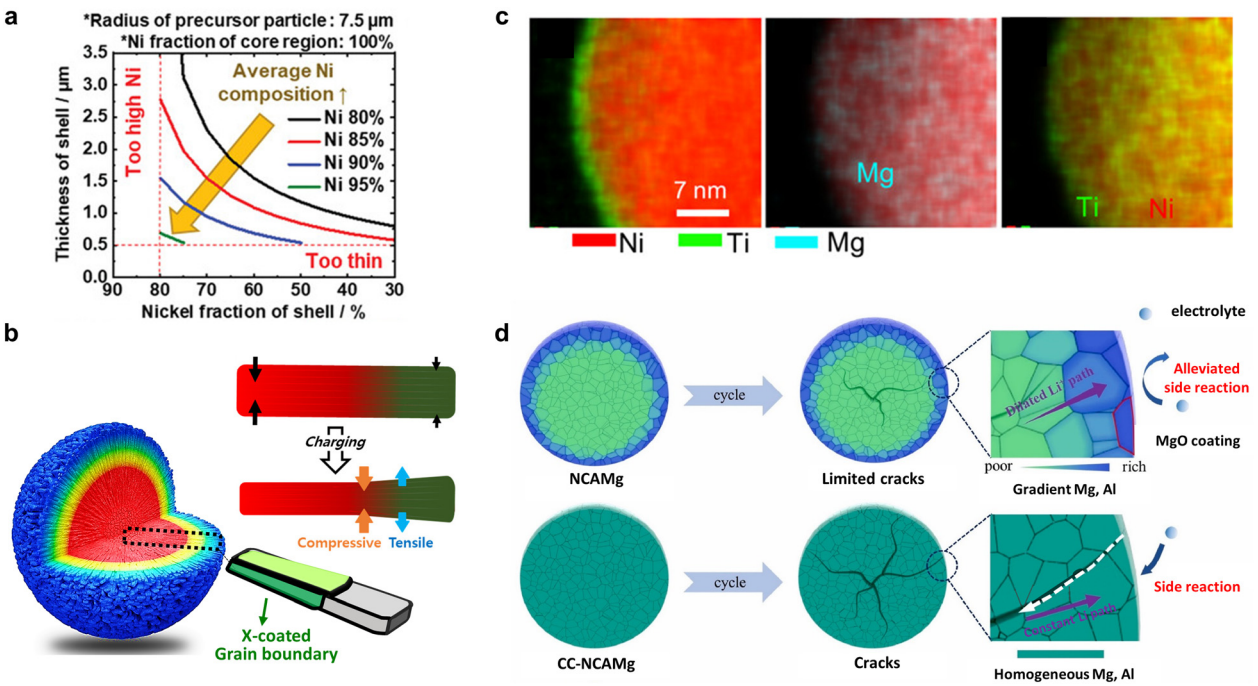

Fig. 25 (a) Concentration gradient profiles demonstrating the limitations of the concentration gradient design as the average Ni content increases. (b) Schematic representation of a nano-rod concentration gradient cathode with a grain boundary coating. (c) and (d) Advanced cathode materials containing dopant concentration gradients. (a) is reproduced with permission,[153] Copyright 2023, John Wiley and Sons. (b) is reproduced with permission,[99] Copyright 2021, American Chemical Society. (c) is reproduced with permission,[262] Copyright 2019, American Chemical Society. (d) is reproduced with permission,[263] Copyright 2022, Elsevier.

some of the challenges found the intermixing of TMs during calcination were overcome by the addition of high-valence dopants. For examples, a Sb-doped concentration gradient cathode material containing 90% Ni was found to possess Sb compounds within its grain boundaries after calcination, which enveloped the primary particles, and segregated at their boundaries (Fig. 25b).[231] This layer slowed down the interdiffusion of TMs (*e.g.*, Ni, Co, and Mn) between the neighboring primary particles. It was therefore considered that the incorporation of Sb ions into the crystal structure delays cation diffusion by altering the adjacent atomic distance. This alteration increases the bulk diffusion barrier energy, thereby impeding the bulk migration of Ni ions. Indeed, concentration gradient cathode materials doped with antimony maintained at least double the concentration difference between the core and surface compared to the corresponding undoped materials. Another benefit of doping concentration gradient cathode materials is the inhibition of coarsening due to the presence of a dopant solute at the grain boundaries.[153,231] While concentration gradient materials without dopants also possess rod-shaped primary particles with a radial alignment, any deviation from the optimal calcination temperature range results in shorter and thicker primary particles, which possess less desirable properties. However, such grain growth can be hindered by solute segregation, which pins the grain boundaries kinetically or thermodynamically. Therefore, this microstructure resulting from high-valence ion doping can be maintained over a wide range of calcination temperatures (*i.e.*, approximately 100 °C), providing a competitive advantage in mass production. Unlike in the laboratory, where the synthetic temperatures can be precisely controlled, industrial-scale cathode synthesis operates over a wide range of temperatures, which may lead to the sintering of the nano-rod primary particles. High-valence ion doping can address this challenge by producing a strong crystallographic texture that ensures exceptional product quality over a wide range of temperatures.

Unlike concentration gradient cathode materials, wherein the concentrations of the major elements (*i.e.*, Ni, Co, and Mn) change gradually, varying the dopant concentration in a cathode material has been demonstrated to enhance cyclability effectively. In this context, Lin *et al.*[262] aimed to enhance the stability of $LiNiO_2$ using dual dopants, namely Mg and Ti (Fig. 25c). They found that both dopants were present at the Ni sites, although Ti was concentrated on the surface, leading to a gradient distribution; in contrast, Mg was uniformly distributed throughout the particles. Similarly, Chen *et al.*[263] synthesized Mg- and Al-gradient Ni-rich cathode materials *via* a co-precipitation approach (Fig. 25d). They found that the high concentrations of Al and Mg on the outer surface induced gentle phase transitions in the highly charged state, while the local segregation of Mg formed a MgO coating layer, which provided a stabilization effect at the electrode–electrolyte interface. Furthermore, Gao *et al.*[264] implemented surface gradient doping by exploiting the characteristic surface segregation caused by the high formation energies associated with yttrium oxides. Importantly, these gradient doping methods have been shown to maintain or enhance Li diffusion while suppressing irreversible phase transitions and TM leaching on the surface. In another study, Whittingham *et al.*[259] controlled the role of the Nb dopant in an NCM811 cathode material by varying the calcination temperatures. The presence of Nb in the coating layer was found to play a role in reducing initial cycle losses and improving the cycling performance, while Nb substitution stabilized the crystal structure to enhance the long-term performance characteristics. It was therefore considered that an optimal combination of coating and doping is ideal, considering the different roles adopted by the dopant depending on its form. Although no extensive studies have focused on engineering the dopant distributions in battery materials, there is ample room to manipulate the three-dimensional gradient distributions of dopants to enhance the stabilities of Ni-rich cathode materials.

The impact of such doping approaches has also been demonstrated in Co-free cathode materials. This is relevant because it is crucial to devise strategies to tackle the expected Co shortage as the battery demand rises.[265] It has been noted that Co^{3+} helps mitigate cation mixing and stabilizes the layered structure by easing magnetic frustration.[266] Additionally, an absence of Co in a layered cathode diminishes the electronic conductivity, leading to a decline in both the rate capability and the performance at low temperatures.[267] Despite numerous efforts to find alternative dopants to substitute the role of Co, these endeavors have failed to yield success. Nevertheless, it has been reported that the design of nanostructured architectures and the alignment of diffusion pathways lead to rapid charging and enhanced durability characteristics.

Although the intrinsic properties of Co cannot be replaced by doping, a strategy has been employed to complement them by forming nano-rod primary particles. Park *et al.*[78] proposed a Co-free NM90 cathode material consisting of ultrafine grains. High-quality doping achieved this, and the resulting grain size refinement dissipated the deleterious strain through fracture toughening, ultimately suppressing microcrack formation during long-term cycling.[268] In addition, the enhanced cation ordering attributed to the presence of high-valence dopants has also been found to stabilize the delithiated structure when the structure is most vulnerable due to the non-uniform extraction of Li^+ ions. Furthermore, Yang *et al.*[252] also enhanced the performance of co-free cathode materials using W^{6+}. More specifically, the cathode material was obtained by coating WO_3 onto the hydroxide precursor and then calcining it. The presence of $Li_xW_yO_z$ on the surface reduced the primary particle size, which enhanced the material's mechanical strength against the anisotropic stress experienced during Li^+ insertion/extraction. It was therefore suggested that the $Li_xW_yO_z$ phases form strong bonds between the primary particles, resulting in fewer microcracks in the W-modified materials.

5.3. Surface shielding of the nano-rod structure

One of the key advantages of microstructural refinement through nano-rod formation is the effective relief of the structural stress generated during charge/discharge, which allows the cathode material to resist microcracking.[269,270] Indeed, many studies have demonstrated that this method suppresses

microcrack formation and enhances the cathode performance.[52,120–122,124,129–132] However, as high Ni contents are required to increase the energy density, it is necessary to develop methods that suppress the resulting material.[36] Although the preparation of crack-resistant particles has been reported, coating the outer surfaces of the particles may also constitute an effective approach to protecting against high Ni contents on the exposed surfaces.[271]

One of the methods proposed for controlling the surfaces of nano-rod cathode materials is F coating.[154,172,240,272] More specifically, F coating has been extensively researched to react with any residual Li present on the surface to form stable LiF compounds. One of the key features of F coating is that, during heat treatment, F is infused into the particles and forms a coating layer along the grain boundaries. When applying such a coating, it is crucial to control the thickness of the coating layer; otherwise, it may simply add to the electrochemically resistive layer, diminishing its effectiveness. In this context, Ryu *et al.*[172] synthesized nano-rod cathode materials by doping Sb into a 93% Ni NCMA material, and subsequently, they further enhanced the material performance by coating with F. Despite controlling the thickness of the F coating layer within tens of micrometers, an abnormal behavior was observed during the initial cycles in the half-cell tests. More specifically, a gradual increase in the delivered capacity was recorded, suggesting an "activation" process was necessary over several cycles. After this process, the rate of capacity degradation decreased, and this effect was more pronounced in the full-cell evaluations. It was therefore considered that the LiF layer in the F-coated nano-rod cathode protects the cathode surface from parasitic side reactions with the electrolyte, attack by HF, and TM dissolution, as evidenced by the reduced intensities of the decomposed electrolyte fragment peaks in the ToF-SIMS depth profile. Interestingly, the F coating significantly improved the lifespans of nano-rod cathode materials, whereas the protective effect of the F coating was insignificant on conventional cathode materials (Fig. 26a). This difference was attributed to the suboptimal microstructure of the conventional cathode, which suffered severe microcracking during cycling to expose the new surface (Fig. 26b). These results, therefore, suggested that the surface protection effect can be maximized when coupled with appropriate microstructure modification.

Another significant issue related to the surfaces of Ni-rich cathodes is the presence of residual Li,[273–276] which forms when the cathode is exposed to air (containing moisture and CO_2) during calcination. The primary cause of the increased residual

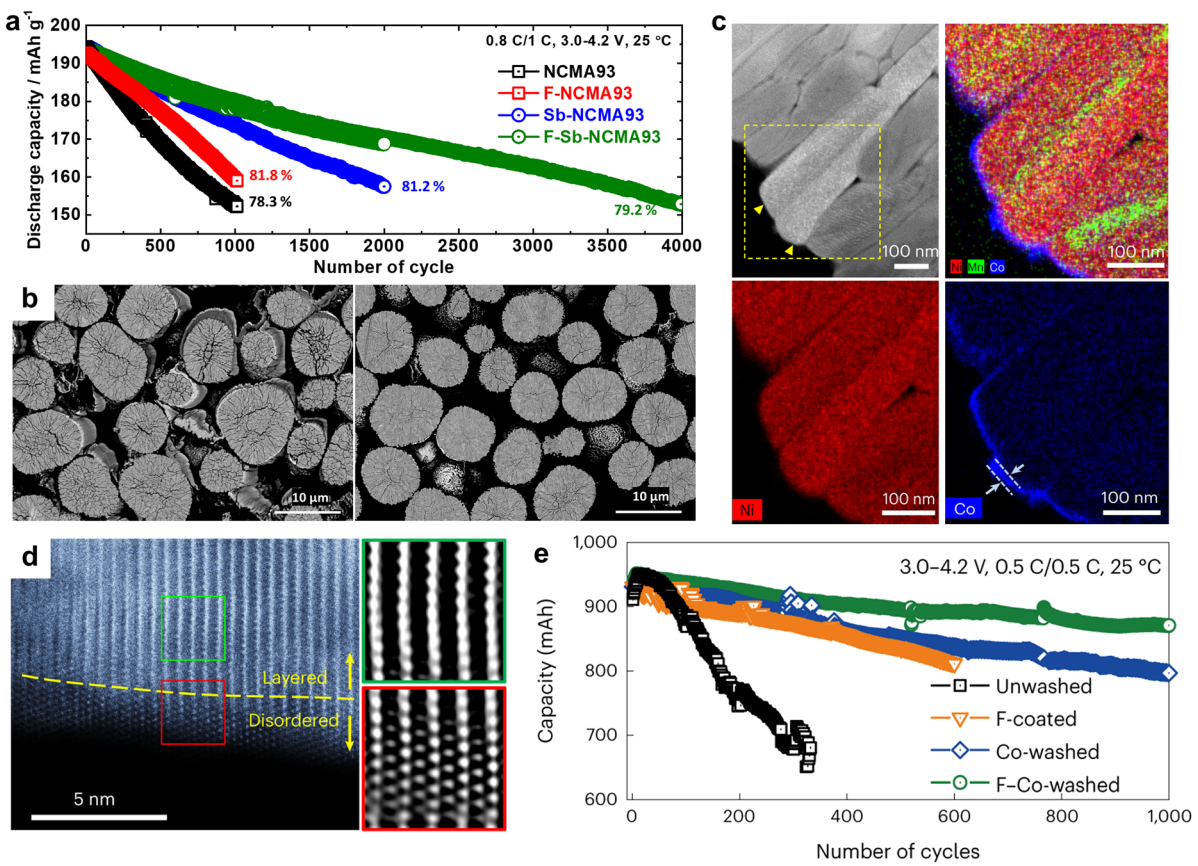

Fig. 26 (a) Comparison of long-term cycling between conventional and nano-rod cathode materials with and without F coating, and (b) cross-section SEM images of the (left) F-NCMA93 and (right) F-Sb-NCMA93 cathodes. (c) TEM-EDS maps, and (d) near-surface structures of the Co-coated cathode surface after washing. (e) Long-term cycling performances of the surface-treated cathode materials. (a) and (b) are reproduced with permission,[172] Copyright 2023, American Chemical Society. (c)–(e) are reproduced with permission,[240] Copyright 2024, Springer Nature.

Li content, particularly in compositions with higher nickel content, is the instability of Ni^{3+} rather than the addition of excessive lithium during synthesis. It is known that the highly reactive Ni^{3+} species present on the surface are reduced to Ni^{2+}, releasing O from the lattice and causing Li to leach out to the surface.[31,34] As a result, the amount of residual Li on the cathode surface increases with the Ni content, thereby rendering residual Li treatment a necessary process.

When a slurry is exposed to air during the electrode coating process, residual Li can gel the slurry, thereby leading to significant manufacturing difficulties. Consequently, strict process control and storage conditions are required to minimize exposure to external air, ultimately leading to increased processing costs.[34,277] Additionally, the residual Li can impede Li movement on the surface during the electrochemical reactions, and it can decompose to generate a gas, thereby causing cell swelling and localized heating, which poses potential safety risks during practical applications.[167] Thus, the presence of residual Li must be carefully considered in the context of commercialization since it increases battery manufacturing costs and can lead to safety and reliability issues. In this regard, nano-rod cathode materials, composed of smaller primary particles than conventional ones, have been considered due to their potential to exhibit different surface conditions and properties. Although the overall fracture toughening effect of nano-sizing has been investigated, the surface issues arising from smaller primary particles have yet to be addressed accurately. Two approaches can be used to prepare such structures: a dopant can be employed, or the calcination temperature can be lowered. However, both methods are likely to increase the amount of residual Li on the surface. More specifically, at low calcination temperatures, there is a high possibility that the Li may not sufficiently penetrate the crystal structure, leaving residual Li on the surface.[278,279] Additionally, when using a dopant, a residue, which is suspected to be a Li–dopant–oxide composite, can remain on the surface.[272] Therefore, controlling and protecting the reactivity of the surface is important in both cases.

When the doping approach is used to form nano-rods, the dopant compounds are passivated on the surface of the cathode material. Since only a very small amount of the dopant compound is present on the surface, it is difficult to determine exactly what structure and composition is formed; however, these are widely speculated to be the abovementioned Li–dopant–oxides. For example, when B doping is used, the possibility of $Li_xB_yO_z$ generation has been studied, while the possibility of $Li_xW_yO_z$ formation during W doping has been explored.[81,242,252,257] The presence of such passivation layers reportedly delays material degradation by reducing the amount of direct contact between the electrolyte and the cathode material surface.[231] However, recent studies have shown that materials doped with Mo produce greater amounts of gas than non-doped materials when left in a charged state for an extended period of time.[272] The gas bubbles formed on the surface disrupt the movement of Li ions and hinder proper contact, thereby preventing the cell from operating normally.[278,280] Moreover, this can lead to battery swelling, posing safety risks. These issues could be the largest obstacles associated with the commercialization process. This increased gas production may be attributed to the inherent characteristics of Mo doping and the presence of various Li compounds on the surface, which originate from the high-valence doping. More specifically, these gas byproducts could be formed from self-decomposition of the Li–dopant compounds, or from the ability of these compounds to act as catalysts and accelerate electrolyte decomposition.

To avoid the detrimental effects associated with residual Li, the current industrial process implemented by battery manufacturers involves washing the Ni-rich cathodes.[281–284] However, washing often leads to performance degradations because the air- and moisture-sensitive cathode materials are immersed in water.[282–284] Therefore, additional coating and heat treatment processes are required to minimize such performance degradations. Notably, the washing procedure removes residual Li from the cathode surface and any Li ions located within the crystal structure through the proton-exchange reaction.[285–288] This extraction may result in surface reconstruction to form rock-salt structures and promote further performance degradation. Heat treatment at significantly high temperatures is necessary to restore the damaged surface structure. For example, Hou *et al.*[289] conducted a systematic investigation into the effect of recalcination on temperature after washing. They varied the holding temperature between 500 and 740 °C and determined that temperatures >600 °C were necessary to restore the layered structure from the rock-salt structure generated during washing.

Dry coating is a simple method to protect the cathode surface from degradation during washing or convert the residual Li into a desirable coating.[240,290–296] However, given that the washing solution comes into contact with all exposed surfaces of the cathode material, conventional dry coating, which results in an island-type coating, generally cannot cover every degraded surface unless the coating agent can diffuse inside the particles and along the grain boundaries. In addition, dry coating has the disadvantage of adding an additional step between the washing and heat treatment stages. In contrast, the wet coating has several advantages despite is associated handling difficulties. More specifically, since a liquid solution is used in the washing process, a coating process could be included in the washing step to achieve the simultaneous removal of residual Li while forming a protective layer.[240,293,296] In this case, the residual Li is employed as a reactant to form the coating layer, and the coating layer formed at the liquid–solid interphase can be uniformly deposited to cover the exposed surface completely. As one literature example, Chen *et al.*[296] carried out the wet coating of $LiNi_{0.83}Mn_{0.1}Co_{0.07}O_2$ by soaking in a diluted $Al(H_2PO_4)_3$ solution and mixing under ultra-sonication. The slightly acidic solution readily reacted with Li_2CO_3 to form Li_3PO_4 and $AlPO_4$ after heat treatment at 550 °C. The same group further investigated the wet impregnation process using several dihydro-phosphate solutions in which the coating proceeded through a similar reaction mechanism with $Al(H_2PO_4)_3$.[297] They paid particular attention to the acidity of the coating solution and argued that a weakly acid

solution with a pK_a of 7.2 imparted the best protection to Ni-rich NMC cathode materials. These protective phosphate layers block chemical attacks by the electrolyte and prevent exposure of the TM atoms, thereby suppressing CO_2 evolution and structural degradation to the rock-salt structure. In another example, Ryu *et al.*[240] combined the idea from co-precipitation process with the wet-coating of a 90% Ni cathode material. They considered that, during co-precipitation of the cathode precursor, dissolved TM ions precipitate as metal hydroxides in the high-pH aqueous solution. In addition, when the Ni-rich cathode material is immersed in water, the pH rapidly rises to >11 due to the high solubility of the residual Li compounds. Thus, to harness these two reactions during the washing step, a Co source was added to the washing solution to promote the direct precipitation reaction on the cathode surface. Since this coating reaction consumed the residual Li present on the cathode surface, it combines the washing and coating steps into a single process. It was demonstrated that the resulting Co coating layer uniformly covered the outer surface with a thickness of a few nanometers (Fig. 26c). Importantly, this precipitate layer was epitaxially grown on the cathode surface through the formation of a crystal structure between the layered and spinel-like phases (Fig. 26d). The Co coating layer remained even after 4000 cycles, which prevented structural degradation by suppressing direct contact between the Ni-enriched cathode surface and the electrolyte. Additionally, a LiF coating layer was added to the Co-coated cathode surface to further enhance the surface stability. While the Co coating process itself removed approximately 40% of the residual Li compared to the unwashed state, the additional F coating further reduced the Li level, resulting in $<50\%$ of the residual Li being retained compared to the unwashed cathode material. The synergistic effect of the F and Co coatings significantly reduced the amount of gas released from the charged cathode materials compared to the unwashed and Co-coated cathodes. Interestingly, the F-coated cathode without Co-washing produced similarly small amounts of gas, suggesting that the suppression of gas evolution from the cathode materials is mostly attributed to the F-coating effect. However, the F coating alone did not sufficiently protect the surface structure from accumulation of the rock-salt phase during cycling, although the LiF layer effectively suppresses the autocatalytic side reactions triggered by electrolyte and impurities decomposition. Therefore, combining a LiF coating and Co-washing effectively protects the near-surface structures of Ni-rich cathodes and removes residual Li impurities, resulting in excellent cycling stabilities without problematic gas release (Fig. 26e).

5.4. Feasibility of nano-rod cathodes for practical application

The cathode material significantly impacts the performance, safety, lifespan, and cost of EV batteries. Cathode materials with higher energy density increase the driving range of EVs to deliver longer driving distances on a single charge and reduce frequency of charging to allow manufacturers to offer longer warranty periods. Cathode materials with higher durability and thermal stability also increase the lifespan of the battery application and reduce the chances of battery swelling or thermal runaway, as safety is an increasingly emphasized aspect of batteries in electric transport applications. However, it is difficult for conventional cathode materials to satisfy these key characteristics, as materials with high energy tend to be highly reactive.[31] Cathode materials that are stable, on the other hand, exhibit low energy density and require a more materials to achieve the desired energy level within a battery cell. This translates to decreased cost-effectiveness and resource inefficiency. As such, determining the performance of electrode materials solely through chemical composition creates a dilemma of balancing energy density, stability, and cost, which makes satisfying all aspects challenging.

Considering these requirements and features, the use of nano-rod cathode materials in EV batteries has become a feasible choice due to their practical advantages in high-performance and long-term applications. Nano-rod cathode materials with microstructural engineering, in addition to chemical composition engineering, can minimize the compromises derived from the trade-offs between energy density, safety, and durability.[50,153] Owing to the systematically structured, spatial configurations, nano-rod cathode materials exhibit excellent durability that preserve the particles coherency and minimize surface degradation even after long-term use. For these reasons, nano-rod cathode materials are adopted in EV batteries such as the KIA Niro, Hyundai Kona EU and Ford F-150 lightning (Fig. 27a).[298–301] The long-term cycling stability of the nano-rod cathodes has been further improved through modifications such as surface coating and additional doping. As shown in Fig. 26a and b, particles with radially aligned nano-rod structures not only retain their structural integrity after cycling but also demonstrate enhanced synergy with surface coating effects. Further strengthening the crystal structure by doping the nano-rod cathode can inhibit the occurrence of microcracks during the cycling process, resulting in enhanced long-term cycling stability; the Al-doped concentration gradient cathode with nano-rods retained 84.5% of its initial capacity after 3000 cycles (Fig. 27b) and inhibited particle pulverization after long-term cycling (Fig. 27c and d).[302] More recently, the fluorine-doped concentration gradient cathode exhibited an unprecedented 8000 cycles operational capability (Fig. 27e),[154] where the cathode material minimized the formation of NiO-like impurity phase on the inner particle surface to bypass the degradation pathway during long-term cycling (Fig. 27f and g). This is significant because impurity phase generated throughout the particles by electrolyte infiltration increases the resistance during Li (de)intercalation, resulting in a significant kinetic capacity loss especially at high C-rates.[119] When these nano-rod cathodes used a carbon nanotube-Si composite anode instead of a graphite anode, which allows higher energy density, the full cell produced an energy density of 350 W h kg^{-1} with excellent capacity retention for 500 cycles at 1C rate, satisfying the energy density and driving range requirement for EVs (Fig. 27h).[238]

By suppressing electrolyte infiltration into the particle interior at the charged state, nano-rod cathode materials exhibit high storage stability and remain stable over prolonged

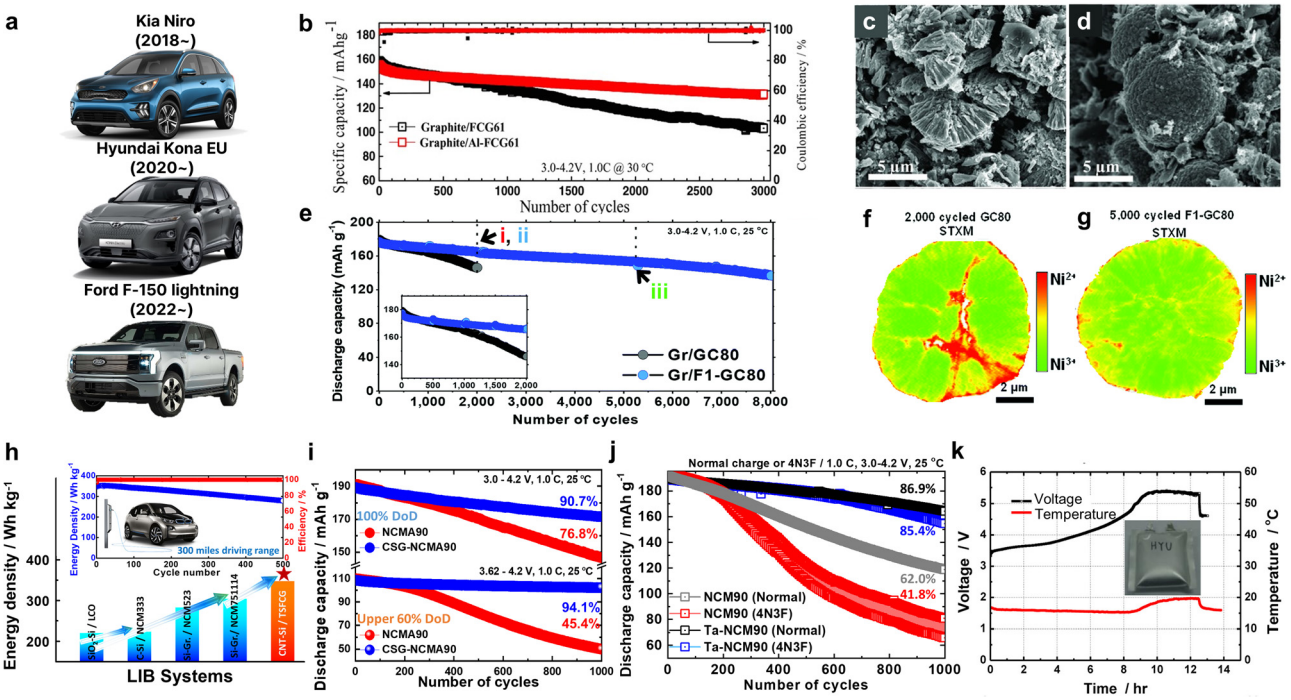

Fig. 27 (a) Kia Niro, Hyundai Kona EU and Ford F-150 Lightning EVs adopting Sk on's cells with nano-rod cathodes. (b) Cycling performance of FCG61 and Al-FCG61 cathodes in a full-cell *versus* graphite anode. SEM images of the cycled (c) FCG61 cathode and (d) Al-FCG61 cathode after 3000 cycles. (e) Long term cycling performance of the GC80 and F1-GC80 cathodes using pouch-type full cells at 25 °C. Mapping of Ni oxidation states for the cycled (f) GC80 (2000 cycles) and (g) F1-GC80 (5000 cycles) cathodes analyzed by STXM. The presence of pure Ni^{3+} and Ni^{2+} are assigned colors green and red, respectively. (h) Energy density of different LIBs. Comparison of the CNT–Si/TSFCG against the currently developed LIBs and schematic illustration of Li-rechargeable battery system based on CNT–Si anode and TSFCG cathode for vehicle application (inset). (i) Long-term cycling performance of NCMA90 and CSG-NCMA90 cathodes cycled at 100% DoD and upper 60% DoD using pouch-type full cells. (j) Long-term cycling performances of the cathodes in full cells under normal charging (0.8C) and 4N3F cycling protocols (4N: 4 times of normal charging at 0.8C, 3F: 3 times of fast charging at 2.0C), with a fixed discharging current of 1.0C (180 mA g^{-1}). (k) Voltage and cell temperature plots with time for laminated-type Al-pouch MCMB/FCG–Mn-F cell (280 mA h), as a function of time during overcharge test. (b)–(d) are reproduced with permission,[302] Copyright 2016, John Wiley and Sons. (e)–(g) are reproduced with permission,[154] Copyright 2021, Royal Society of Chemistry. (h) is reproduced with permission,[238] Copyright 2016, Royal Society of Chemistry. (i) is reproduced with permission,[66] Copyright 2021, John Wiley and Sons. (j) is reproduced with permission,[303] Copyright 2024, John Wiley and Sons. (k) is reproduced with permission,[48] Copyright 2013, American Chemical Society.

exposure times. When the cathode material is at the charged state, high oxidation states of nickel and structural instability lead to rampant side reactions. Problem is that devices are often stored in a charged state in practical applications. In a study simulating such a scenario by Namkoong *et al.*, cells that remained in the charged state exhibited shortened lifespan. However, in cells with the nano-rod structure cathode, the performance remained largely unaffected even with prolonged storage in a charged state.[173] Similarly, the range and limit of the depth of discharge (DoD), which determine the extent of micro-cracking, critically affect the cycling stability as persistent micro-cracks in the upper DoD range allowed electrolyte to penetrate the particle interior.[66,304] Nano-rod cathode materials not only can be utilized across the entire DoD range, but also they show superior characteristics even at the commonly used upper DoD range compared to the conventional cathodes (Fig. 27i).

The unique microstructural features of nano-rod cathodes also offer additional advantages for fast charging, making them highly suitable for practical applications. The extended primary particle morphology in a radial configuration facilitates Li^+ diffusion by providing a direct pathway from the core to the surface. This enables the battery to deliver high performance even at high C-rates and reduces charging time. Unlike the conventional cathode, which does not sufficiently dissipate the stress induced by the H2–H3 phase transition under fast charging conditions, the exceptional durability of the nano-rod cathode helps maintain superior rate capabilities even after long-term cycling.[189,303] Kim *et al.* applied extreme-fast-charging protocol to test the effect of fast charging on cathode materials.[189] In a full cell evaluation driven at 4C over 500 cycles at elevated temperatures, the nano-rod-structured cathode material not only maintained a more intact form and performance but also exhibited a more uniform lithium distribution throughout the particles. This indicates that the migration of Li ions is expedited through short-distance diffusion facilitated by numerous interparticle boundaries. Considering that EV users employ a mix of normal and fast charging, a cycling protocol of four normal charges (0.8C) followed by three fast charges (2.0C), denoted as 4N3F, was applied (Fig. 27j).[303] Unlike NCM90 which shows sharply deteriorated capacity after 200 cycles under 4N3F condition, Ta-NCM90 with nano-rods exhibited a minimal capacity difference between fast and

normal charging conditions, demonstrating that the latter effectively maintain fast charging capabilities during long-term cycling. These properties enhance user convenience and maximize feasibility as cathode materials for EV batteries.

In addition, nano-rod cathode materials demonstrate superior thermal stability even after long-term cycling, as confirmed by DSC analysis, indicating reduced risk of thermal propagation or explosion during device usage.[48] Fig. 27k shows the variation of cell voltage and temperature with time after overcharge. After overcharge (at 250% state of charge), the cell featuring nano-rod cathode shows a voltage increase to only 5.5 V, with the temperature remaining below 20 °C. The nano-rod cathode also shows stable characteristics in nail penetration test, indicating robust resistance to physical impact as shown in Fig. 13c. The superior thermal stability is attributed to the material not breaking apart to minimize surface exposure to electrolyte even after cycling. These tests clearly show the significant improvements in the safety aspect, ensuring the reliability even in the event of accidents and providing greater relief to battery consumers. As demonstrated by their adoption in commercial EV batteries, various enhanced properties of nano-rod cathodes compared to conventional cathodes make nano-rod cathodes feasible for practical applications.

6. Next-generation batteries

In addition to their application in LIBs, cathode materials with nano-rod primary particles are also employed in next-generation energy storage devices, including all-solid-state batteries (ASSBs), Li-metal batteries (LMBs), and Na-ion batteries (SIBs).

6.1. All-solid-state batteries

6.1.1. Challenges in all-solid-state batteries. To completely eliminate the safety issues caused by combustible liquid electrolytes, the use of solid electrolytes (SEs) instead of liquid electrolytes is considered an alternative solution for LIBs.[305] Therefore, ASSBs with good safety profiles and high energy densities have received considerable attention, such as those based on Li-metal anodes and the bi-polar stacking technology. Following years of development, the ion conductivities of SEs (10^{-2} S cm^{-1}) have reached the same order of magnitude as those of liquid electrolytes;[306] however, the design of practical ASSBs containing high-performance cathodes remains a challenge. The capacity fading of ASSBs originating from composite cathodes is primarily attributed to three factors: surface degradation at cathode/solid electrolyte interfaces, isolation of internal particles by microcracks, and detachment of cathode particles from the SE (Fig. 28a).[307,308] Because typical sulfide-based SEs have a narrow electrochemical stability window of 1.71–2.31 V *vs.* Li/Li^+, they are not electrochemically or chemically compatible with typical 4-V-class layered cathodes.[308–310] As a result, the cathode/SE interface is susceptible to parasitic reactions, resulting in the reconstruction of the cathode surface from a layered structure to a rock-salt structure and the concomitant decomposition of the SE, leading to an impedance buildup. With increasing Ni content, this effect amplifies due to an abundance of highly reactive Ni^{4+} species in the highly delithiated state.[308] Mechanically, the lattice volume change of the cathode during the charge discharge isolates internal particles through microcracks and detaches the cathode particles from the SE. During charging, intergranular microcracks develop due to strain in the cathode particles induced by anisotropic lattice volume changes. Microcracking disconnects the grain boundaries and causes loss of contact with the SE to sunder Li^+ diffusion pathways, thus inhibiting Li^+ diffusion and leading to structural heterogeneity.[311,312] Furthermore, the microcracks that propagate to the secondary particle surfaces result in the fracture of these particles into smaller fragments. which develop into dead sites due to the loss of contact with the cathode connected to the SE. Therefore, repeated microcracking during cycling leads to deteriorated cycling stability of the composite cathode in ASSB. This effect becomes more pronounced with increasing Ni content. In addition, the lattice contraction of the cathode during delithiation may lead to the detachment of the active material from the SE.[313] The voids observed between the cathode particle and the SE after cycling are attributed to the lattice volume contraction in the cathode during charging. The lattice volume changes in cathode particles also affect the composite cathode as a whole, resulting in not only detachment but also the formation of pores within the SE. The voids and contact loss caused by these detachments disrupt Li^+ conduction between cathode particles and the SE, thereby contributing to capacity fading. Unlike liquid electrolytes that can penetrate into large secondary particles, SEs only wrap around the peripheries of the cathode particles. Due to the inability of SE to refill newly formed microcracks and interface voids, the capacity deterioration by mechanical degradation is amplified in ASSB systems, resulting in shorter service lives compared to batteries using liquid electrolytes.[313,314] The degree of particle isolation within the cathode and detachment from SE become more pronounced with increasing Ni content, as demonstrated by NCA80 and NCA95 cathode particles after 50 cycles (Fig. 28b), which limits the utilization of Ni-rich cathodes in ASSBs.

6.1.2. Nano-rod cathodes in all-solid-state batteries. To overcome the above challenges, the development of cathode materials suitable for use in high-performance ASSBs has received growing research attention.[306] Although some studies have revealed that single-crystal cathodes capable of eliminating intergranular cracks could effectively achieve practical ASSBs, comparisons have only been carried out with traditional polycrystalline materials comprising randomly oriented primary particles.[316,317] As mentioned above, the grain refinement strategy is favored in traditional LIB systems because it can dissipate mechanical stress and provide rapid ion diffusion channels,[241,318,319] which may provide a new perspective for the development of ASSBs. In this context, Jung *et al.*[314] elucidated the electrochemo-mechanical effects of Ni-rich cathode particles in ASSBs by comparing conventional NCA and FCG cathode materials (Fig. 28c). In stark contrast to the severely disintegrated NCA cathode at the charged state

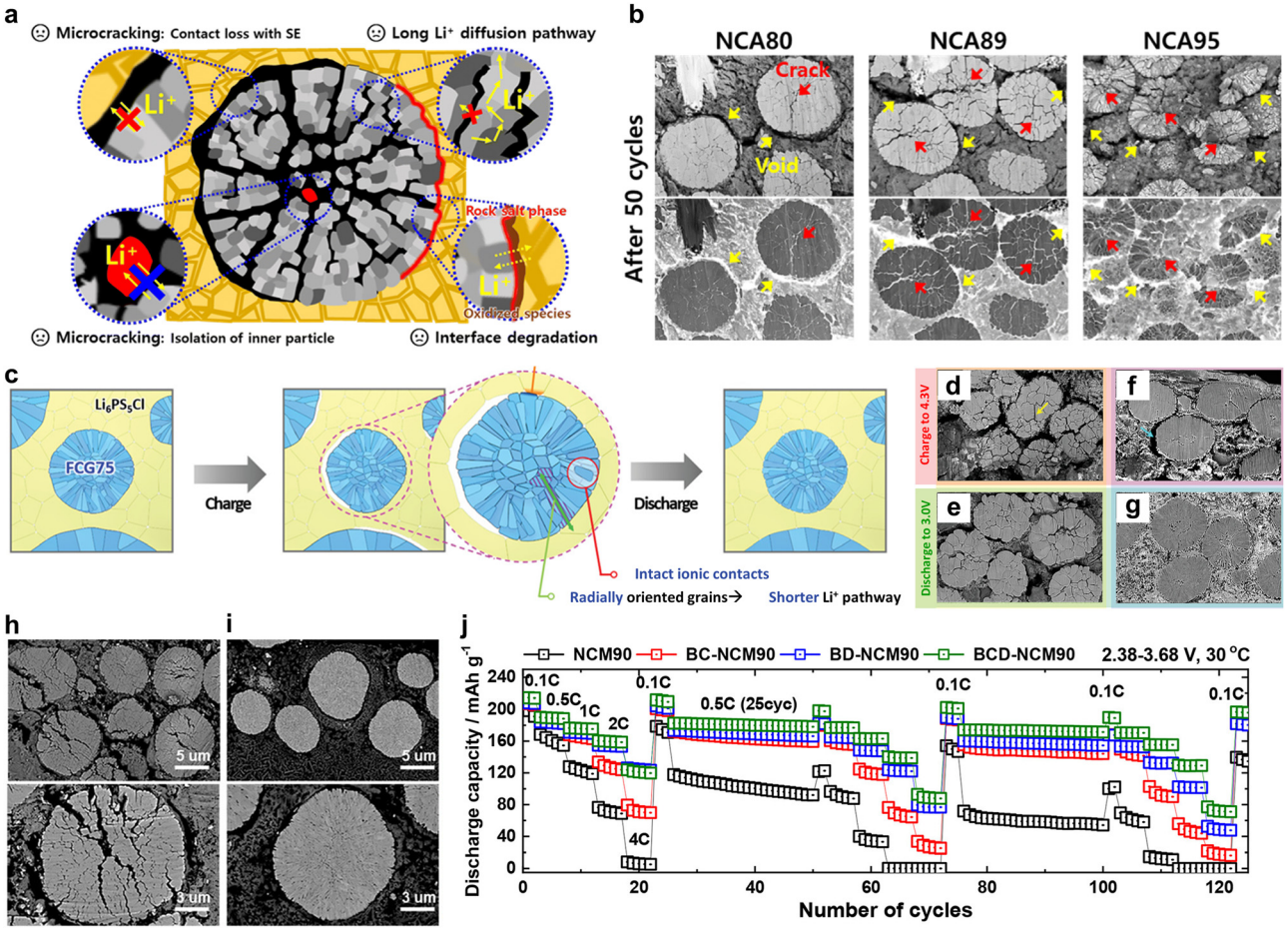

Fig. 28 (a) Schematic illustration of the capacity fading mechanism of a Ni-rich cathode in an ASSB. (b) Cross-sectional SEM images of the NCA80, NCA89, and NCA95 electrodes recovered from ASSBs after 50 cycles. (c) Schematic diagram of the impact of cathode materials with customized microstructures on the performance of ASSBs (related to interface stability). Cross-sectional SEM images of (d), (e) NCA80 and (f), (g) FCG75 electrodes after (d), (f) first charge to 4.3 V (*vs.* Li/Li$^+$) and (e),(g) the subsequent discharge to 3.0 V (*vs.* Li/Li$^+$). Cross-sectional SEM images of (h) NCM90 and (i) BCD-NCM90 cathodes after cycling recovered from ASSBs. (j) Electrochemical test combining cycle and rate capability tests for NCM90, BC-NCM90, BD-NCM90 and BCD-NCM90 cathodes. (a) and (b) are reproduced with permission,[308] Copyright 2023, Royal Society of Chemistry. (c)–(g) are reproduced with permission,[314] Copyright 2019, John Wiley and Sons. (h)–(j) are reproduced with permission,[315] Copyright 2023, American Chemical Society.

(Fig. 28d), the FCG cathode, composed of radially arranged rod-shaped primary particles, effectively dissipated the internal stress induced by lattice volume change and maintained mechanical integrity (Fig. 28f). Although detachment of the cathode particle from SE still occurred in the FCG cathode in the charged state due to lattice volume contraction, the extent was less compared to the conventional cathode. After discharge, the isolation of internal particles by microcracks and the detachment of cathode particles from SE remained irreversibly in the conventional NCA cathode (Fig. 28e), whereas the isolation and detachment largely disappeared after discharge of FCG cathode because the nano-rod structure enabled uniform cathode particle contraction and expansion (Fig. 28g). Cross-sectional SEM images of the cycled electrode and operando electrochemical pressiometry measurements successfully demonstrated this.[314] In addition, the concentration distribution of the TM ions inherited from the FCG precursor reduced the exposure to active Ni^{4+} species, thereby suppressing parasitic side reactions and inhibiting surface structural degradation. Therefore, the constructed practical ASSB (NCM/Li_6PS_5Cl/Li-In) simultaneously delivered a high reversible capacity (196 mA h g^{-1}) and a long cycle life (79.1% capacity retention after 200 cycles at 0.5C). In addition to mechanical degradation, the compatibility between a cathode material and the SE is also a key factor that limits the development of ASSBs.[307] To investigate this aspect, Zhang *et al.*[320] designed a CS NCMA cathode coated with $LiNbO_3$, wherein the shell was composed of rod-shaped primary particles that were poor in Ni. The introduced protective coating not only inhibited decomposition of the SE, but it also delayed surface degradation of the cathode, thereby improving the stability of the cathode/SE interface. Hence, the optimized ASSB (NCMA/$Li_{9.54}Si_{1.74}P_{1.4}S_{11.7}Cl_{0.3}$/Li-In) exhibited an excellent cycling stability, with a capacity retention of 96.4% after 300 cycles at 0.5C. In another study, Kim *et al.*[315] successfully synthesized B-doped and/or B-coated NCM90 composite cathodes. The pristine NCM90 cathode, composed of polygonal primary particles with randomly oriented microstructures, displayed limited electrochemical

reaction after cycling due to the aforementioned composite cathode/SE degradation mechanism (Fig. 28h). The introduction of B into the cathode changes the morphology of the primary particles into nano-rods which effectively dissipated strain and suppressed microcracks upon cycling (Fig. 28i). Although the B-doped NCM maintained the mechanical integrity of the cathode by inhibiting microcrack formation through the nano-rod structure, detachment of cathode particles from the SE still occurred due to volume changes in the cathodes, albeit at a lessened degree. Therefore, to further overcome the capacity fading in cathodes with nano-rod structure, it is essential to suppress the detachment of cathode particles from the SE by other approaches (*e.g.*, zero-strain cathode or elastic SE) that maintain the physicochemical contact between the cathode particles and the SE even during repeated lattice volume changes. The electrochemical performance evaluation of ASSBs using B-coated and/or B-doped NCM90 in Fig. 28j demonstrated that suppressing mechanical degradation of the composite cathode by B doping is more effective in maintaining cycle life and rate capability than suppressing surface reactions at the cathode/SE interface by B coating. Particularly, BD-NCM90 and BCD-NCM90, which have a nano-rod structure, exhibited excellent rate capabilities even after extended cycling. This demonstrates the importance of facilitating electrochemical reactions throughout the composite cathode by minimizing resistance associated with isolation and detachment. Benefiting from this dual optimization strategy, an ASSB composed of the optimized cathode (B-coated and B-doped NCM90, BCD-NCM90) and Li_6PS_5Cl as the SE displayed a high initial discharge capacity of 214 mA h g^{-1} and a long cycle life, maintaining 90.7% of its initial capacity after 300 cycles at 0.5C, which is superior to the majority of other reported systems.

6.2. Li-metal batteries

6.2.1. Challenges in Li-metal batteries. LMBs have the potential to maximize energy density by utilizing Li metal as the anode, which has a theoretical capacity of 3860 mA h g^{-1}. Increasing the operating voltage and the Ni content in layered oxide cathodes is an effective approach to achieving higher energy density in LMBs. However, the phase transition of the cathode materials and the uncontrolled decomposition of the electrolytes can lead to irreversible dissolution of TM ions, which can cause crossover effects on the lithium metal anodes (Fig. 29a). The dissolution of TMs from the cathode and subsequent deposition of TMs on the anode can lead to severe degradation of the solid electrolyte interphase (SEI) on the anode surface (Fig. 29b).[321–323] Previous studies have reported that the exposure of fresh surfaces of the NCM to electrolyte, due to particle cracking during cycling, is the main culprit of

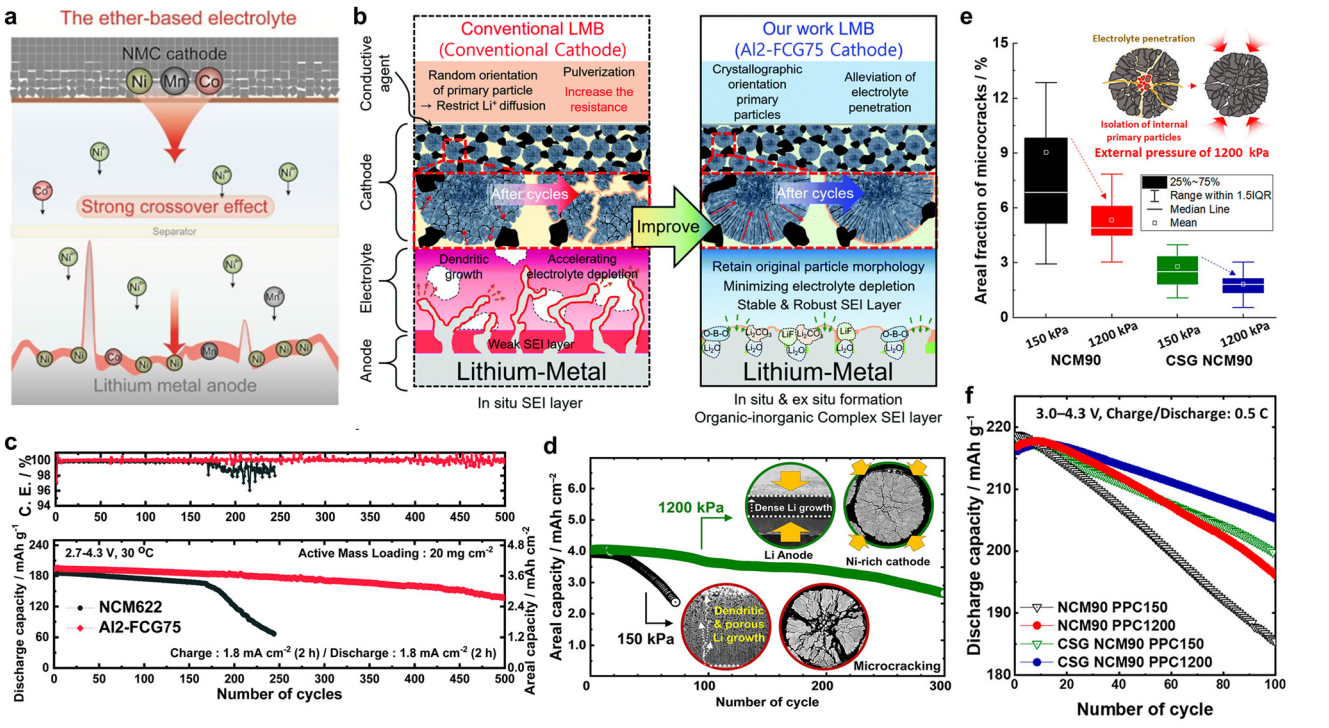

Fig. 29 (a) Schematic illustration of crossover effect resulted from TM dissolution in LMBs. (b) Summary of conventional LMBs and the LMB concept using Al2-FCG75 cathode with nano-rods. (c) Comparison of the cycling performance of Li/NCM622 and Li/Al2-FCG75 cells with high capacity loading of 4.1 mA h cm^{-2} cycling at 1.8 mA cm^{-2}. (d) Comparison of the cycling performances of Li/FCG NCM78 (loading level of 20 mg cm^{-2}) PPC150 with the coated separator and PPC1200 with the coated separator. (e) Box-and-whisker plot demonstrating the areal fraction of microcracks in the NCM90 and CSG NCM90 particles after 100 cycles in PPC150 and PPC1200. (f) Comparison of cycling performances of Li/NCM90 (loading level of 10 mg cm^{-2}) PPC150 and PPC1200 and Li/CSG NCM90 (loading level of 10 mg cm^{-2}) PPC150 and PPC1200. (a) is reproduced with permission,[323] Copyright 2023, Springer Nature. (b) and (c) are reproduced with permission,[327] Copyright 2019, Royal Society of Chemistry. (d)–(f) are reproduced with permission,[328] Copyright 2023, American Chemical Society.

TM dissolution.[324,325] It catalyses solvent decomposition, leading to the formation of a thick SEI, which then reduces the Coulombic efficiency (CE) of the cells and ultimately shortens the life of the cell. Furthermore, increased surface area of cathode/electrolyte interface due to microcracks can induce electrolyte depletion.[325] Electrolyte depletion is detrimental to the cycling stability of lean electrolyte LMBs because it leads to ionic disconnection at un-wet regions, deactivating the active materials and increasing the cell impedance.[326] Although many studies on LMB have used strategies to inhibit dendrites by modifying the electrolyte solution or the surface of the lithium metal, it is necessary to optimize the cathode for LMB taking into account the crossover effect.

6.2.2. Nano-rod cathodes Li-metal batteries. Although various strategies and improvements for LMBs have been reported,[329–339] their effects are often more pronounced when applied alongside compatible cathode materials. From this perspective, the advantages of nano-rod cathode materials are evident even in the LMBs. For example, Hwang *et al.*[327] formed a stable SEI layer by adding a specially designed LiDFOB electrolyte and treating Li metal with $LiNO_3$ to effectively inhibit Li metal growth on the surface. The resulting LMB cells, with conventional NCM622 and Al-doped FCG (Al2-FCG75) cathode materials, showed that despite the higher Ni content, the Al2-FCG75 cathode with nano-rods achieved a higher mechanical stability to inhibit material degradation and maintain a higher cycling stability even at higher current densities, thereby allowing higher loading levels. In long-term cycling test, the Li/NCM622 cell with $LiNO_3$-treated Li-metal and LiDFOB electrolyte showed good cycling stability at 1.8 mA cm^{-2} up to the 170th cycle, with a capacity fade rate of 0.06% per cycle (Fig. 29c) but experienced significant capacity drop and erratic CE beyond the 170th cycle. When the cathode and anode from the cycled cell were reassembled with fresh electrodes ($LiNO_3$-treated Li-metal and NCM622, respectively) and LiDFOB electrolyte, the recovered Li-metal anode cell reproduced the discharge capacity of a fresh anode at 1.8 mA cm^{-2}. In contrast, the recovered NCM622 cathode exhibited a 13% decrease in discharge capacity, indicating that the cathode failure was responsible for the drastic capacity degradation of the Li/NCM622 cell. This is corroborated by the NCM622 secondary particles largely being pulverized after cycling, losing their initial spherical morphology. Conversely, the Li/Al2-FCG75 cell with the $LiNO_3$-treated anode and LiDFOB electrolyte demonstrated exceptional cycling stability, with extremely high CE ($\geq$99.8%) maintained up to 500 cycles at 1.8 mA cm^{-2}. Not surprisingly, the spherical shape of the Al2-FCG75 secondary particles remained intact with minimal cracking after 500 cycles to support this cycling stability. These findings emphasize the critical importance of selecting appropriate cathode materials alongside strategies to protecting Li metal to achieve practical long-term cycling stability in LMBs.

In addition to modifying the electrolyte solution or the surface of the lithium metal, external pressure application has been another successful strategy in suppressing Li dendrite growth and controlling Li metal deposition.[328,335] Kim *et al.*[328] induced uniform Li metal deposition in a LMB using a carbonate-based electrolyte and a boehmite-coated separator under an external pressure of 1200 kPa. As shown in Fig. 29d, pressure-controlled pouch-type cells (PPCs) at a high pressure (1200 kPa) level drives Li metal growth as a dense uniform layer, whereas at a low pressure (150 kPa) level, the Li metal growth was dendritic and porous. Furthermore, the analysis of the cycled NCM90 cathode revealed that compressive stress mitigates crack nucleation and propagation, thus providing a so-far-unexplored option for suppressing inherent microcracking and improving the cycling stability of Ni-rich layered cathodes. As shown in Fig. 29e, the effectiveness of this external pressure in suppressing microcracks in the cathode was maximized when using a nano-rod cathode such as the CSG NCM90, which inhibits the formation of microcracks during charge and discharge and maintains the electrical pathways throughout the particle without any discontinuity. Therefore, as shown in Fig. 29f, the CSG NCM90 cathode with nano-rods exhibited the most stable cycling when evaluated at 1200 kPa. Furthermore, the nano-rod cathode materials were able to effectively withstand the external pressure, emphasizing the mechanical stability of this structure and aptitude for high pressure conditions. When the surface of CSG NCM90 cathode was further coated with F, the PPC featuring the coated cathode cycled at 1200 kPa retained 82.0% of the initial capacity after 500 cycles with a loading level of 22 mg cm^{-2}, an E/C ratio of 2.8 μL mA h^{-1}, and an anode to cathode capacity ratio (N/P ratio) of 2.7 using a 70 μm thick Li foil. The capacity retention at high loading levels of >4 mA h cm^{-2} is markedly superior to that observed in LMBs utilizing carbonate-based electrolytes, and is comparable to that observed in LMBs utilizing ether-based electrolytes. These studies demonstrate the importance of cathode material properties, particularly mechanical stability and resistance to microcracks, for future LMBs, as the performance of an LMB are significantly impacted by the cathode.

6.3. Sodium-ion batteries

6.3.1. Challenges in sodium-ion batteries. One of the primary challenges in SIB technology is overcoming the capacity fading, often resulting from the relatively large size of Na^+ (Li^+: 0.76 Å *vs.* Na^+: 1.02 Å) (Fig. 30a), which hinders its facile diffusion into and out of the cathode crystal structure.[31,340,341] The comparatively larger size of the Na^+ ion induces severe phase transitions during electrochemical reactions, accompanied by significant mechanical stress (Fig. 30b). Fig. 30c illustrates the differential capacity (dQ/dV) *versus* voltage for lithium-ion batteries (LIB) and sodium-ion batteries (SIB) using NM5050 material. The LIB operates within a voltage range of approximately 2.7 V to 4.3 V, showing broad peaks corresponding to lithium intercalation and deintercalation processes. Conversely, the SIB operates from around 2.3 V to 4.3 V, with peaks around 3.0 V, 3.6 V, and 4.0 V. These differences in peak positions and shapes between LIB and SIB indicate the unique electrochemical mechanisms for lithium and sodium ions. The NM5050 material accommodates both lithium and sodium ions, albeit with different efficiencies and reaction dynamics.[342] For instance,

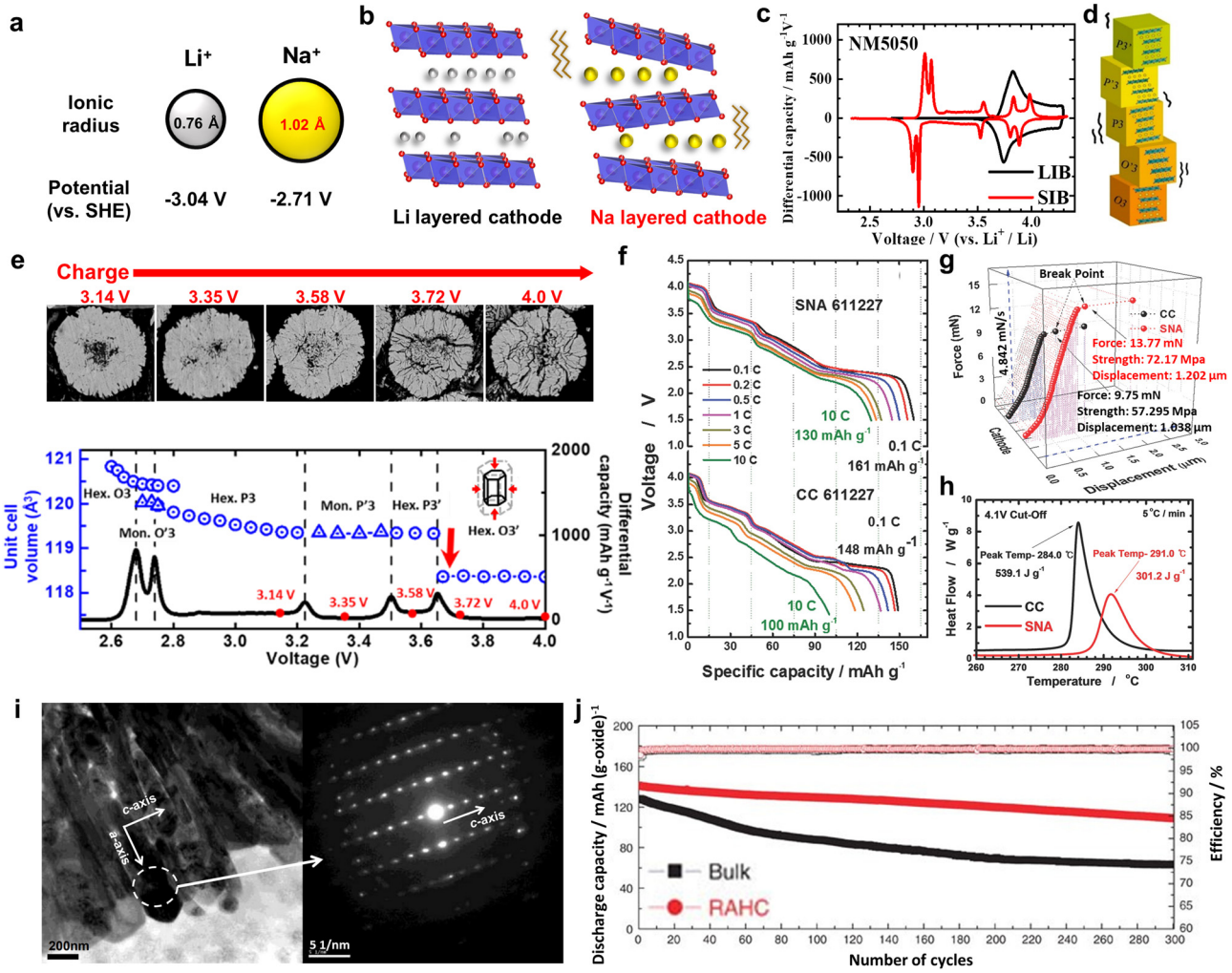

Fig. 30 (a) Comparison of ionic radius and standard hydrogen electrode potential of Li/Li^+ and Na/Na^+. (b) Schematic illustration of lithium- and sodium-ion layered crystal structure. (c) Differential capacity ($dQ\ dV^{-1}$) profile of the $LiNi_{0.5}Mn_{0.5}O_2$ (Li-NM5050) and $NaNi_{0.5}Mn_{0.5}O_2$ (Na-NM5050) cathodes. (d) Phase transition scheme of the $NaNi_{0.5}Mn_{0.5}O_2$ cathode during the charge and discharge process. (e) Cross-sectional SEM images of $Na_xNi_{0.5}Mn_{0.5}O_2$ cathode in different charged states during the 1st cycle and corresponded unit cell volume variations combined with $dQ\ dV^{-1}$ profile. (f) Rate capability comparison of CC $Na[Ni_{0.61}Co_{0.12}Mn_{0.27}]O_2$ (CC 611227) and SNA $Na[Ni_{0.61}Co_{0.12}Mn_{0.27}]O_2$ (SNA 611227) at various discharge C-rates from 0.1C (15 mA g^{-1}) to 10C (1500 mA g^{-1}). (g) Micro-compression test results for CC $Na[Ni_{0.61}Co_{0.12}Mn_{0.27}]O_2$ and SNA $Na[Ni_{0.61}Co_{0.12}Mn_{0.27}]O_2$ single cathode particles. (h) DSC tests results of desodiated CC and SNA $Na[Ni_{0.61}Co_{0.12}Mn_{0.27}]O_2$. (i) TEM image and the corresponding electron diffraction pattern from a RAHC primary particle, illustrating the crystallographic alignment of the primary particle along the radial direction. (j) Long-term cycling performance of $Na[Ni_{0.60}Co_{0.05}Mn_{0.35}]O_2$-RAHC/hard carbon and $Na[Ni_{0.60}Co_{0.05}Mn_{0.35}]O_2$-bulk/hard carbon full cells within voltage range of 1.5–3.9 V. (c) and (e) are reproduced with permission,[342] Copyright 2020, John Wiley and Sons. (d) is reproduced with permission,[344] Copyright 2019, American Chemical Society. (f), (g), and (h) are reproduced with permission,[346] Copyright 2016, John Wiley and Sons. (i) and (j) are reproduced with permission,[347] Copyright 2015, Spring Nature.

the O3-type $Na[Ni_{0.5}Mn_{0.5}]O_2$ cathode experiences several phase transitions: starting from hexagonal O3 to monoclinic O′3, then to hexagonal P3, followed by monoclinic P′3, hexagonal P3′, and finally reverting to a hexagonal O3′ phase[3.14 V (P3), 3.35 V (P′3), 3.58 V (P3′), 3.72 V (O3′), and 4.0 V (O3′)].[342,343] Among these multiple-phase transitions, the emergence of the hexagonal O3' phase under a deeply charged state compromises the mechanical stability (Fig. 30d) and leads to sudden structural collapse occurring during this phase transition.[344] Similar to Ni-rich cathodes in LIBs, degradation occurs through microcrack formation and fracture of the secondary particles, followed by electrolyte penetration to the particle interior (Fig. 30e).[342,345] Therefore, microcrack formation also poses a serious threat to the operation of Na cathode materials.

6.3.2. Nano-rods in sodium-ion batteries. The radial alignment of nano-rods within secondary particles of layered oxide cathodes has many applications, especially in terms of LIB technologies.[348] More specifically, this customized configuration increases the ion diffusion, electrode density, mechanical stress, and thermal management, thereby providing guidance regarding tuning the electrode design for individual performance requirements.[127,346,347,349,350] Indeed, it has been reported that the incorporation of radially oriented nano-rods within layered oxide cathodes can substantially improve battery safety, energy

density, and cycle life.[48,127,346] Even beyond LIBs, the introduction of nano-rod primary materials in layered oxide cathodes can lead to intriguing physicochemical properties with the potential for enhancing energy storage in SIBs.[351] O3-type materials experience gradual capacity fading during prolonged cycling due to multiple phase transitions. To develop effective O3-type cathode materials for NIBs, a new concept, tuned to SIBs, was introduced: spoke-like nano-rod assemblies (SNAs), with a chemical composition varying from the inner core ($Na[Ni_{0.75}Co_{0.08}Mn_{0.17}]O_2$) to the outer shell ($Na[Ni_{0.58}Co_{0.14}Mn_{0.28}]O_2$), totaling in an average composition of $Na[Ni_{0.61}Co_{0.12}Mn_{0.27}]O_2$. The inner composition, $Na[Ni_{0.75}Co_{0.08}Mn_{0.17}]O_2$, delivers high capacity, while the outer composition, $Na[Ni_{0.58}Co_{0.14}Mn_{0.28}]O_2$, helps maintain structural integrity by preventing multiphase transitions. The rate capability and voltage profiles for the SNAs and conventional cathode (CC) at various rates are shown in Fig. 30f. The SNA cathode exhibits higher discharge capacity retention than the CC cathode at all current densities. Specifically, at a 10C rate, the SNA cathode delivers a high discharge capacity of approximately 130 mA h g^{-1}, while the CC cathode delivers only 100 mA h g^{-1}. The micro-compression test (MCT) results in Fig. 30g show the dramatic difference in particle strength between SNA and CC cathode materials. The parameters in the figure indicate the final detected force and displacement point just prior to particle destruction. Under the same test conditions, the SNA particles (diameter: 13.04 μm) were resistant to a force of approximately 13.8 mN (displacement: 1.202 μm), resulting in a particle strength of approximately 72.2 MPa. In contrast, the CC particles (diameter: 12.32 μm) showed much lower values (test force of about 9.76 mN, displacement of about 1.038 μm, corresponding to a particle strength of about 57.3 MPa). These mechanical strengths demonstrate the significant advantage in robustness of the SNA cathode particles composed of nano-rods, compared to the CC particles. Furthermore, as shown by the DSC test results in Fig. 30h, the thermal reactions of SNA and CC cathodes start at around 291 and 284 °C, respectively, with specific heat generation around 301.2 and 539.1 J g^{-1}, respectively. It shows that nano-rod cathodes in SIBs have improved thermal stability *via* a similar mechanism to that of nano-rod cathodes in LIBs (Fig. 13).

A radially aligned hierarchical columnar (RAHC) structure, which is similar to SNAs, in spherical particles with varied chemical composition from the inner core ($Na[Ni_{0.75}Co_{0.02}Mn_{0.23}]O_2$) to the outer shell ($Na[Ni_{0.58}Co_{0.06}Mn_{0.36}]O_2$) of the structure has been developed.[347] The TEM image of the RAHC particle shows that the primary particles are radially oriented (Fig. 30i). The SAED pattern from the marked region confirms that the layer planes (*i.e.*, *a*–*b* planes) in the hexagonal structure, perpendicular to the c-axis, are nearly parallel to the radial direction emanating from the particle center, demonstrating that the layer planes of the marked primary particle are radially oriented, confirming an apparent crystallographic texture in the primary particles of the RAHC cathode. The cathode with RAHC structure reduced side reactions during long-term electrochemical cycling (Fig. 30j). This cathode material facilitates an electrochemical reaction based on $Ni^{2+/3+/4+}$, delivering a discharge capacity of 157 mA h (g-oxide)$^{-1}$ at 15 mA g^{-1}, a capacity retention of 80% (125 mA h g^{-1}) over 300 cycles when paired with a hard carbon anode, and a rate capability of 132.6 mA h g^{-1} at 1500 mA g^{-1} (10C-rate). Additionally, the cathode performs well at low temperatures, even at −20 °C. These results are attributed to the unique chemistry of the cathode material, which enables efficient Ni redox reactions and minimizes the surface area in contact with the corrosive electrolyte. Furthermore, the nano-rods uniformly expanded and contracted during Na ion insertion and extraction, allowing the whole secondary spherical particles to reduce or absorb the cycling stresses.[49] Therefore, the nano-rod-based cathode was able to withstand high currents without any morphological damage, even at extremely low operation temperatures (*e.g.*, −10 °C).[347] In addition, the nano-rods enhanced the electrode energy density due to the high tap density of the densely packed spherical micron-sized particles, which reduced the exposure of the active material to the electrolyte solution and to HF attack. Owing to the excellent integrated structure and mechanical strength, the nano-rod-based cathode exhibited a significant improvement in its thermal reactions (with a high onset temperature and a lower level of heat generation) at the deeply charged state.[352,353] The interfacial stability (*i.e.*, moisture resistance, delayed active material dissolution, and prevention of electrolyte side reactions/decomposition) of the cathode was further stabilized by utilizing aluminum fluoride (AlF_3) coating, improving the cycling performances of practical cells.[188,354–356] This combination of particle engineering and surface modification strategies to develop advanced cathode materials is therefore crucial for achieving the large-scale applications of SIBs, which requires further research efforts in the coming years.[355,357]

7. Conclusions and perspectives

In this paper, we comprehensively reviewed the origin, physicochemical properties, challenges, and advances of nano-rods in layered oxide cathodes and as well as their application in lithium-ion and next-generation batteries (ASSBs, LMBs, SIBs). The microstructure of the cathode active material is principally determined by its hydroxide precursor.[68,109,160,247] For this reason, the development of radially aligned rod-shaped primary particles in the precursor is a prerequisite for the eventual development of a nano-rod structure in the cathode material (Fig. 31a). However, the conventional method for synthesizing cathodes, in which materials are subject to high calcining temperatures (>700 °C), invariably leads primary particles to coarsen and form the randomly oriented and equiaxed primary particles often observed in conventional layered cathode materials.[79,211] Therefore, multi-stage engineering, from precursor synthesis to morphological control through doping, is important for developing the nano-rod structure in cathode materials and enhancing their respective electrochemical performances. The representative methods for developing nano-rod in cathode materials are summarized in below:

(1) Nano-rod structures can be obtained by compositional partitioning of the cathodes, in which nano-rods are firstly

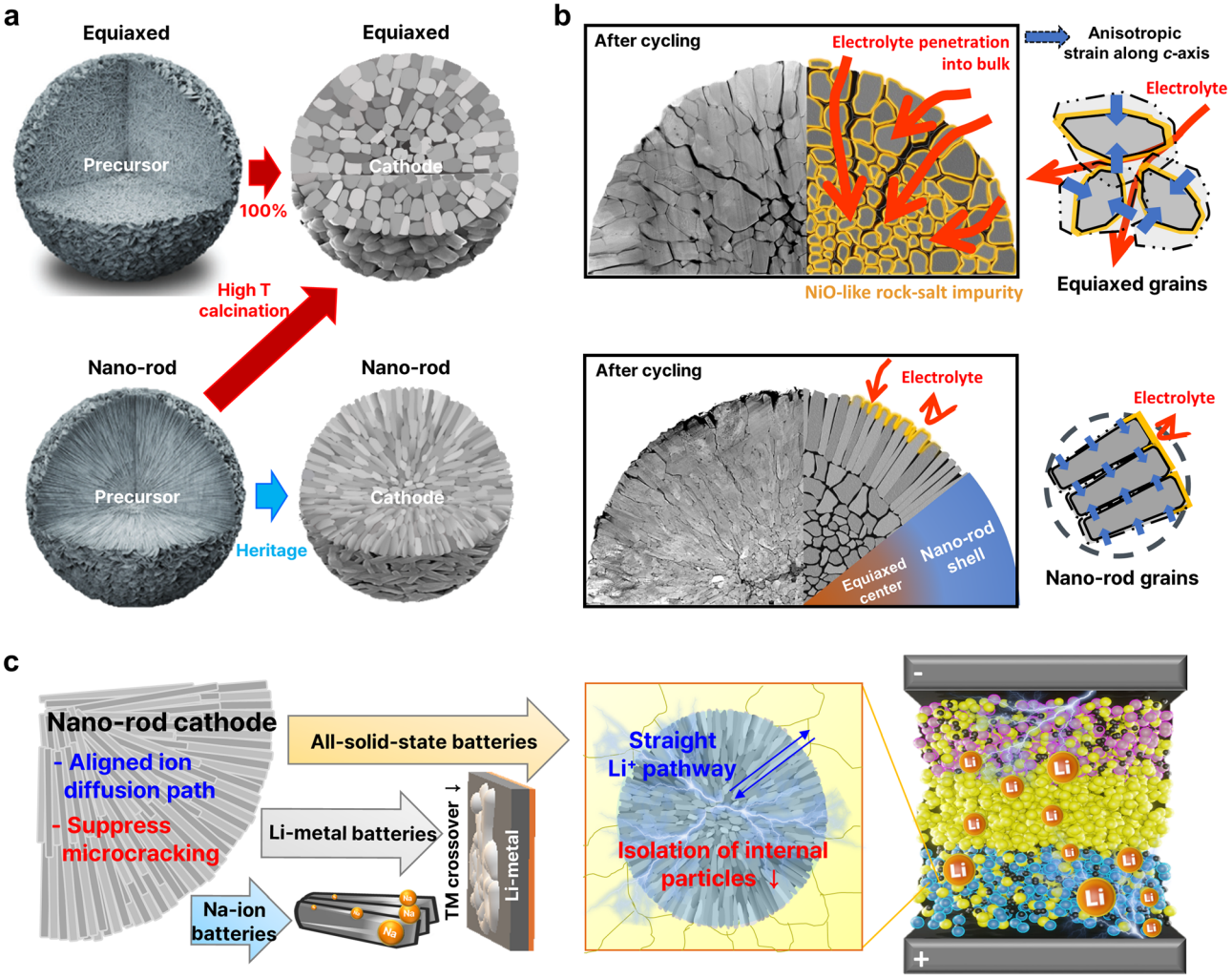

Fig. 31 (a) Schematic illustration showing inheritance of the precursor microstructure by the cathode material. (b) Schematic illustration showing the cycled cathode particles featuring equiaxed and nano-rod grains, respectively. In a nano-rod cathode, the radially textured columnar grains in the shell prevent microcrack nucleation and propagation, while in conventional cathode, microcracks propagate and allow the electrolyte to penetrate. (c) Schematic illustration of the application of nano-rod cathodes in various next-generation batteries (ASSBs, LMBs and SIBs). (a) is reproduced with permission,[68] Copyright 2021, Royal Society of Chemistry. (b) is reproduced with permission,[49] Copyright 2019, John Wiley and Sons.

recognized.[46] In a concentration gradient precursor, the presence of the twin MnOOH and $Ni(OH)_2$ phases mitigates the thermally-induced crystallographic distortion by maintaining the layered planes parallel along the radial direction, while also retarding sintering of the adjacent primary particles.[160] The nano-rod structures are mostly observed in Ni-rich (Ni $\geq$ 60%) cathodes.[46,55,58,78,122,188] However, because the twin MnOOH plays a role in mitigating grain coarsening, cathodes featuring high Mn concentration favor the formation of nano-rod grains.

(2) For conventional cathodes without a concentration gradient, nano-rod structure can be achieved through controlled precursor synthesis and doping processes. Doping with elements such as B facilitates the formation of nano-rods by reducing the formation energy of the (003) facet during lithiation.[51,52,69,100]

(3) Doping with high-valent elements, such as Nb, Ta, W, Sb, and Mo, tends to lead to their segregation at the grain boundaries, which prevents the coarsening of the primary particles and maintains the nano-rod microstructure of the precursor.[53,57,76,79,80,129,153]

(4) Similarly, even when easily incorporated elements, *e.g.*, Al and Mn, are introduced into the lattice in excess doping amounts, segregation at the grain boundaries was still observed, and a rod-shaped cathode material was obtained.[68,72,106]

Although various dopants have been investigated, it is essential to comprehend the principles behind their mechanisms of action and categorize the dopants accordingly. This understanding will ultimately facilitate the rational design of cathode materials.

The unique geometric characteristics of nano-rod-grained cathodes greatly influence layered oxide cathodes' physicochemical and electrochemical properties. Recently, the use of nano-rod-grained cathodes in EV batteries has become a feasible choice due to their practical advantages in high-performance and long-term applications.[298–301] The characteristics arising from constructing radially aligned nano-rod grains are summarized as follow:

(1) One of the main benefits of constructing radially aligned nano-rod grains is the resulting enhanced mechanical durability. The nano-rod grains effectively suppress microcrack formation and propagation by mitigating stress inside the cathode particle, which is induced by lattice volume contraction upon charging.[36,51,52,122] Protection of the cathode particle interior from direct contact with the electrolyte offers additional sturdiness in terms of both the chemical and structural stabilities, thereby enhancing the electrochemical performance of the cathode (Fig. 31b).[50,66,75]

(2) The construction of a strong crystallographic texture in the nano-rod-grained cathode provides direct Li^+ diffusion paths, thereby improving the rate performance of the cathode.[98,101,206]

(3) The generated nano-rod grains sometimes contain different local domains, such as rock-salt, disordered spinel, cation-ordered, and twinned crystal structures.[57,116,138,146,148,150] These modified crystal structures contribute to delaying the electrochemical cycle-induced irreversible structural degradation, thereby improving the cycle life of the cathode.

(4) Nano-rod grains feature more abundant lateral facets and fewer frontal facets than equiaxed-shaped grains.[69,101] Because the structural degradation along the lateral side of the grains is insignificant, nano-rod grains can attenuate parasitic chemical reactions along the surfaces in contact with the electrolyte solution.[66,231]

(5) Cathode particles constructed of nano-rod grains feature outstanding thermal stability. This is attributed to the chemo-mechanical protection offered by the tightly packed radially oriented grains, which mitigate microcrack propagation and protect internal particle surfaces from direct contact with the electrolyte.[129,188]

Though rarely reported, formation of nano-rod can adversely accelerate oxidative reactions between the highly reactive Ni^{4+} and electrolytes.[120,272] Nano-rod grains can increase specific surface area of the cathode, thereby providing more risks for cathode-electrolyte reactions and gas evolutions along the secondary particle surfaces.[54] Thus, it is important to understand the altered surface properties resulting from these nano-rod structures. Viable solutions to resolve such chemical degradation issue in nano-rod cathode are shown below:

(1) Formation of concentration gradient in nano-rod cathode can significantly attenuate surface reactivity of the cathode active material.[36,49,98] The compositional and spatial configurations offered by concentration gradient provide the greatest benefit when the Ni content of the gradient cathode increases dramatically toward 100%. By reducing the Ni contents of the nano-rod primary particles on the outer surfaces, gradient cathode materials can delay surface degradation.

(2) Optimization of the washing and coating processes can enhance the surface chemical stability of the cathode. For instance, F-coating has been demonstrated to inhibit gas generation and electrolyte decomposition, while Co-washing prevents degradation of the surface structure.[172,240,272]

(3) Dopant-gradient approaches have demonstrated successful cathode surface shielding, with dopants preferentially locating to the surface and interparticle boundaries to protect active material from irreversible structural degradation and oxidative decomposition of the electrolyte.[93,252,262,263]

(4) Careful selection of electrolyte solution is also an option to greatly mitigate deleterious side reactions between electrolyte solution and cathodes.[42,358,359] Since the surface degradation arises from the existence of highly-reactive Ni^{4+}, which is a dominant ionic species comprising the delithiated Ni-rich cathodes, the aforementioned methods, *e.g.*, coating and doping, *etc.*, does not solely overcome the intrinsic surface degradation issue of the Ni-rich cathode.[139,142] One example of mitigating surface reactivity *via* modification of electrolyte is the use of fluoroethlyene carbonate (FEC). FEC is a well-known electrolyte additive to improve the performance of anodes (Si, MoS_2, Li metal).[360–363] However, recent studies suggested that use of FEC can significantly improve the long-term cycling performance of the nano-rod cathodes.[58,78] FEC promotes formation of a stable LiF-rich layer on the cathode surface, thereby protecting cathode active material from side reactions.[328,364,365] Additionally, various additives, such as Li_3PO_4, LiDFOB, and *etc.* those are compatible with Ni-rich cathodes are also suggested.[366–369] Nevertheless, the feasibility of adopting new electrolyte solutions in nano-rod cathodes for practical batteries needs further investigation.[370] Comprehensive studies regarding the formation mechanism of CEI, degree of TM dissolution, gas evolution extent, aging characteristics, and *etc.* should be verified before adoption in practical batteries.[371] The use of advanced electrolytes that are stable at high potentials and long-term cycling will allow high-energy-density and long range batteries. Therefore, both the nano-rod cathode and advanced electrolyte should be considered in tandem for developing high-performance LIBs.

Next-generation batteries such as all-solid-state batteries (ASSBs), Li-metal batteries (LMBs), and Na-ion batteries (SIBs) are at the forefront of current research and development to address key energy storage, safety, and performance challenges. Among the critical components of these advanced battery systems, cathode materials with nano-rod structures have emerged as pivotal elements contributing to their advancement. For example, nano-rod cathode structures have been demonstrated to facilitate ion diffusion and suppress the mechanical failures induced by volume changes; these characteristics are crucial for achieving high energy densities and long cycle lives in ASSBs and LMBs.[314,315,327,328] Similarly, nano-rod cathode materials exhibit superior mechanical stabilities, suppressing microcrack formation and improving the electrochemical activities of SIBs.[346,347] Overall, it is clear that cathode materials possessing the nano-rod structure will play a pivotal role in advancing next-generation battery technologies, offering solutions to key challenges and paving the way for safer, more efficient, and longer-lasting energy storage systems (Fig. 31c).

Nano-rod-based cathode materials, therefore, hold immense promise in revolutionizing batteries across various applications, from LIBs to next-generation systems (ASSBs, LMBs, and SIBs). These cathodes exhibit remarkable physicochemical and electrochemical properties, enhancing the battery's performances in multiple aspects. Continued research and development are therefore crucial to unlocking the full potential of

nano-rod cathode materials and accelerating the adoption of advanced battery technologies in various applications, from portable electronics to electric vehicles and grid-scale energy storage.

Data availability

No primary research results, software or code have been included and no new data were generated or analysed as part of this review.

Conflicts of interest

There are no conflicts to declare.

Acknowledgements

The authors would like to thank Tae-Yeon Yu, Hun Kim for help in discussions, and Jae-Ho Kim, Min-Soo Kim for preparation of parts of the figures. This work was supported by the Human Resources Development Program (No. 20214000000320) and ESS Big Data-Based O&M and Asset Management Technical Manpower Training (RS-2024-00398346) of the Korea Institute of Energy Technology Evaluation and Planning (KETEP), funded by the Ministry of Trade, Industry, and Energy of the Korean government.

Notes and references

1 A. Yoshino, *Angew. Chem., Int. Ed.*, 2012, **51**, 5798.
2 M. Li, J. Lu, Z. Chen and K. Amine, *Adv. Mater.*, 2018, **30**, 1800561.
3 J. B. Goodenough and Y. Kim, *Chem. Mater.*, 2010, **22**, 587.
4 J. B. Goodenough and K.-S. Park, *J. Am. Chem. Soc.*, 2013, **135**, 1167.
5 R. Schmuch, R. Wagner, G. Hörpel, T. Placke and M. Winter, *Nat. Energy*, 2018, **3**, 267.
6 S.-T. Myung, F. Maglia, K.-J. Park, C. S. Yoon, P. Lamp, S.-J. Kim and Y.-K. Sun, *ACS Energy Lett.*, 2016, **2**, 196.
7 M. Wentker, M. Greenwood and J. Leker, *Energies*, 2019, **12**, 504.
8 K. Mizushima, P. C. Jones, P. J. Wiseman and J. B. Goodenough, *Mater. Res. Bull.*, 1980, **15**, 783.
9 M. S. Whittingham, *Chem. Rev.*, 2004, **104**, 4271.
10 Q. Zhong, A. Bonakdarpour, M. Zhang, Y. Gao and J. R. Dahn, *J. Electrochem. Soc.*, 1997, **144**, 205.
11 Z. Lu, D. D. MacNeil and J. R. Dahn, *Electrochem. Solid-State Lett.*, 2001, **4**, A191.
12 J. R. Dahn, U. von Sacken and C. A. Michal, *Solid State Ionics*, 1990, **44**, 87.
13 D. Aurbach, Z. Lu, A. Schechter, Y. Gofer, H. Gizbar, R. Turgeman, Y. Cohen, M. Moshkovich and E. Levi, *Nature*, 2000, **407**, 724.
14 Z. Lu, D. D. MacNeil and J. R. Dahn, *Electrochem. Solid-State Lett.*, 2001, **4**, A200.
15 A. Nytén, A. Abouimrane, M. Armand, T. Gustafsson and J. O. Thomas, *Electrochem. Commun.*, 2005, **7**, 156.
16 R. Dominko, M. Bele, A. Kokalj, M. Gaberscek and J. Jamnik, *J. Power Sources*, 2007, **174**, 457.
17 C. Delmas, J.-J. Braconnier, C. Fouassier and P. Hagenmuller, *Solid State Ionics*, 1981, **3–4**, 165.
18 A. Manthiram, *Nat. Commun.*, 2020, **11**, 1550.
19 T. Ohzuku, A. Ueda, M. Nagayama, Y. Iwakoshi and H. Komori, *Electrochim. Acta*, 1993, **38**, 1159–1167.
20 D. Andre, S.-J. Kim, P. Lamp, S. F. Lux, F. Maglia, O. Paschos and B. Stiaszny, *J. Mater. Chem. A*, 2015, **3**, 6709.
21 W. Li, E. M. Erickson and A. Manthiram, *Nat. Energy*, 2020, **5**, 26.
22 C. Daniel, D. Mohanty, J. Li and D. L. Wood, *AIP Conf. Proc.*, 2014, **1597**, 26.
23 P. Rozier and J. M. Tarascon, *J. Electrochem. Soc.*, 2015, **162**, A2490.
24 R. J. Clément, Z. Lun and G. Ceder, *Energy Environ. Sci.*, 2020, **13**, 345.
25 A. O. Kondrakov, H. Geßwein, K. Galdina, L. de Biasi, V. Meded, E. O. Filatova, G. Schumacher, W. Wenzel, P. Hartmann, T. Brezesinski and J. Janek, *J. Phys. Chem. C*, 2017, **121**, 24381.
26 T. Liu, L. Yu, J. Liu, J. Lu, X. Bi, A. Dai, M. Li, M. Li, Z. Hu, L. Ma, D. Luo, J. Zheng, T. Wu, Y. Ren, J. Wen, F. Pan and K. Amine, *Nat. Energy*, 2021, **6**, 277.
27 K. M. Shaju, G. V. Subba Rao and B. V. R. Chowdari, *Electrochim. Acta*, 2002, **48**, 145.
28 M. H. Lee, Y. J. Kang, S. T. Myung and Y. K. Sun, *Electrochim. Acta*, 2004, **50**, 939.
29 LG Energy Solution's Automotive Batteries for Commercial Vehicles, **https://www.lgensol.com/assets/file/202312_LGES_Commercial_EV_Catalog_en.pdf**, (accessed June 2024).
30 LG Energy Solution expanding R&D for battery leadership, **https://www.koreatimes.co.kr/www/tech/2024/05/129_306276.html**, (accessed June 2024).
31 H.-J. Noh, S. Youn, C. S. Yoon and Y.-K. Sun, *J. Power Sources*, 2013, **233**, 121.
32 Y.-K. Sun, D.-J. Lee, Y. J. Lee, Z. Chen and S.-T. Myung, *ACS Appl. Mater. Interfaces*, 2013, **5**, 11434.
33 J. Jiang, K. W. Eberman, L. J. Krause and J. R. Dahn, *J. Electrochem. Soc.*, 2005, **152**, A566.
34 W. Zhang, C. Yuan, J. Zhu, T. Jin, C. Shen and K. Xie, *Adv. Energy Mater.*, 2023, **13**, 2202993.
35 J. Kim, H. Lee, H. Cha, M. Yoon, M. Park and J. Cho, *Adv. Energy Mater.*, 2018, **8**, 1702028.
36 H.-H. Ryu, K.-J. Park, C. S. Yoon and Y.-K. Sun, *Chem. Mater.*, 2018, **30**, 1155.
37 R. Jung, M. Metzger, F. Maglia, C. Stinner and H. A. Gasteiger, *J. Electrochem. Soc.*, 2017, **164**, A1361.
38 H. Li, A. Liu, N. Zhang, Y. Wang, S. Yin, H. Wu and J. R. Dahn, *Chem. Mater.*, 2019, **31**, 7574.
39 G. W. Nam, N.-Y. Park, K.-J. Park, J. Yang, J. Liu, C. S. Yoon and Y.-K. Sun, *ACS Energy Lett.*, 2019, **4**, 2995.
40 E. Trevisanello, R. Ruess, G. Conforto, F. H. Richter and J. Janek, *Adv. Energy Mater.*, 2021, **11**, 2003400.

41 H.-H. Ryu, B. Namkoong, J.-H. Kim, I. Belharouak, C. S. Yoon and Y.-K. Sun, *ACS Energy Lett.*, 2021, **6**, 2726.
42 D. Aurbach, B. Markovsky, G. Salitra, E. Markevich, Y. Talyossef, M. Koltypin, L. Nazar, B. Ellis and D. Kovacheva, *J. Power Sources*, 2007, **165**, 491.
43 B. L. D. Rinkel, J. P. Vivek, N. Garcia-Araez and C. P. Grey, *Energy Environ. Sci.*, 2022, **15**, 3416.
44 J. Li, L. E. Downie, L. Ma, W. Qiu and J. R. Dahn, *J. Electrochem. Soc.*, 2015, **162**, A1401.
45 EcoProBM, SK On and Ford to invest C$1.2B to build NCM cathode manufacturing facility in Bécancour, Québec, **https://www.greencarcongress.com/2023/08/20230818-ford.html**, (accessed June 2024).
46 Y.-K. Sun, Z. Chen, H.-J. Noh, D.-J. Lee, H.-G. Jung, Y. Ren, S. Wang, C. S. Yoon, S.-T. Myung and K. Amine, *Nat. Mater.*, 2012, **11**, 942.
47 Y.-K. Sun, S.-T. Myung, B.-C. Park, J. Prakash, I. Belharouak and K. Amine, *Nat. Mater.*, 2009, **8**, 320.
48 H.-J. Noh, Z. Chen, C. S. Yoon, J. Lu, K. Amine and Y.-K. Sun, *Chem. Mater.*, 2013, **25**, 2109.
49 U.-H. Kim, H.-H. Ryu, J.-H. Kim, R. Mücke, P. Kaghazchi, C. S. Yoon and Y.-K. Sun, *Adv. Energy Mater.*, 2019, **9**, 1803902.
50 C. S. Yoon, K.-J. Park, U.-H. Kim, K. H. Kang, H.-H. Ryu and Y.-K. Sun, *Chem. Mater.*, 2017, **29**, 10436.
51 K.-J. Park, H.-G. Jung, L.-Y. Kuo, P. Kaghazchi, C. S. Yoon and Y.-K. Sun, *Adv. Energy Mater.*, 2018, **8**, 1801202.
52 H.-H. Ryu, N.-Y. Park, J. H. Seo, Y.-S. Yu, M. Sharma, R. Mücke, P. Kaghazchi, C. S. Yoon and Y.-K. Sun, *Mater. Today*, 2020, **36**, 73.
53 U.-H. Kim, G.-T. Park, B.-K. Son, G. W. Nam, J. Liu, L.-Y. Kuo, P. Kaghazchi, C. S. Yoon and Y.-K. Sun, *Nat. Energy*, 2020, **5**, 860.
54 H.-H. Ryu, N.-Y. Park, D. R. Yoon, U.-H. Kim, C. S. Yoon and Y.-K. Sun, *Adv. Energy Mater.*, 2020, **10**, 2000495.
55 P. Ju, L. Ben, Y. Li, H. Yu, W. Zhao, Y. Chen, Y. Zhu and X. Huang, *ACS Energy Lett.*, 2023, **8**, 3800.
56 J.-H. Shim, Y.-H. Kim, H.-S. Yoon, H.-A. Kim, J.-S. Kim, J. Kim, N.-H. Cho, Y.-M. Kim and S. Lee, *ACS Appl. Mater. Interfaces*, 2019, **11**, 4017.
57 H. H. Sun, U.-H. Kim, J.-H. Park, S.-W. Park, D.-H. Seo, A. Heller, C. B. Mullins, C. S. Yoon and Y.-K. Sun, *Nat. Commun.*, 2021, **12**, 6552.
58 G.-T. Park, S.-B. Kim, B. Namkoong, N.-Y. Park, H. Kim, C. S. Yoon and Y.-K. Sun, *Mater. Today*, 2023, **71**, 38.
59 M. Dalkilic, A. Schmidt, T. D. Schladt, P. Axmann, M. Wohlfahrt-Mehrens and M. Lindén, *J. Electrochem. Soc.*, 2022, **169**, 120501.
60 C. T. Rueden, J. Schindelin, M. C. Hiner, B. E. DeZonia, A. E. Walter, E. T. Arena and K. W. Eliceiri, *BMC Bioinf.*, 2017, **18**, 529.
61 T. R. Jones, I. H. Kang, D. B. Wheeler, R. A. Lindquist, A. Papallo, D. M. Sabatini, P. Golland and A. E. Carpenter, *BMC Bioinf.*, 2008, **9**, 482.
62 J. M. Sosa, D. E. Huber, B. Welk and H. L. Fraser, *Integr. Mater. Manuf. Innov.*, 2014, **3**, 123.
63 D. Hou, Z. Xu, Z. Yang, C. Kuai, Z. Du, C.-J. Sun, Y. Ren, J. Liu, X. Xiao and F. Lin, *Nat. Commun.*, 2022, **13**, 3437.
64 W. Li, J. Zhang, Y. Zhou, W. Huang, X. Liu, Z. Li, M. Gao, Z. Chang, N. Li, J. Wang, S. Lu, X. Li, W. Wen, D. Zhu, Y. Lu and W. Zhuang, *ACS Appl. Mater. Interfaces*, 2020, **12**, 47513.
65 C. Zhu, M. Cao, H. Zhang, G. Lv, J. Zhang, Y. Meng, C. Shu, W. Fan, M. Zuo, W. Xiang and X. Guo, *ACS Appl. Mater. Interfaces*, 2021, **13**, 48720.
66 N.-Y. Park, H.-H. Ryu, G.-T. Park, T.-C. Noh and Y.-K. Sun, *Adv. Energy Mater.*, 2021, **11**, 2003767.
67 W. Huang, W. Li, L. Wang, H. Zhu, M. Gao, H. Zhao, J. Zhao, X. Shen, X. Wang, Z. Wang, C. Qi, W. Xiao, L. Yao, J. Wang, W. Zhuang and X. Sun, *Small*, 2021, **17**, 2104282.
68 G.-T. Park, N.-Y. Park, T.-C. Noh, B. Namkoong, H.-H. Ryu, J.-Y. Shin, T. Beierling, C. S. Yoon and Y.-K. Sun, *Energy Environ. Sci.*, 2021, **14**, 5084.
69 C.-H. Jung, D.-H. Kim, D. Eum, K.-H. Kim, J. Choi, J. Lee, H.-H. Kim, K. Kang and S.-H. Hong, *Adv. Funct. Mater.*, 2021, **31**, 2010095.
70 W. Yang, H. Li, D. Wang, C. Xu, W. Xiang, Y. Song, F. He, J. Zhang, B. Zheng, B. Zhong, Z. Wu and X. Guo, *Nano Energy*, 2022, **104**, 107880.
71 L. Wang, B. Zhu, D. Xiao, X. Zhang, B. Wang, H. Li, T. Wu, S. Liu and H. Yu, *Adv. Funct. Mater.*, 2023, **33**, 2212849.
72 G.-T. Park, S.-B. Kim, J.-I. Yoon, N.-Y. Park, M.-C. Kim, S.-M. Han, D.-H. Kim, M.-S. Kim and Y.-K. Sun, *Adv. Energy Mater.*, 2024, **14**, 2400130.
73 R. Wang, J. Chen, Y. Zhang, Z. Li, S. Cao, X. Liu, H. Hu, L. Wu, Y. Shen and X. Wang, *Chem. Eng. J.*, 2024, **485**, 149827.
74 T. Thien Nguyen, U.-H. Kim, C. S. Yoon and Y.-K. Sun, *Chem. Eng. J.*, 2021, **405**, 126887.
75 H. H. Sun, A. Dolocan, J. A. Weeks, A. Heller and C. B. Mullins, *ACS Nano*, 2020, **14**, 17142.
76 U.-H. Kim, J.-H. Park, A. Aishova, R. M. Ribas, R. S. Monteiro, K. J. Griffith, C. S. Yoon and Y.-K. Sun, *Adv. Energy Mater.*, 2021, **11**, 2100884.
77 C. S. Yoon, M.-J. Choi, D.-W. Jun, Q. Zhang, P. Kaghazchi, K.-H. Kim and Y.-K. Sun, *Chem. Mater.*, 2018, **30**, 1808.
78 G.-T. Park, B. Namkoong, S.-B. Kim, J. Liu, C. S. Yoon and Y.-K. Sun, *Nat. Energy*, 2022, **7**, 946.
79 G.-T. Park, D. R. Yoon, U.-H. Kim, B. Namkoong, J. Lee, M. M. Wang, A. C. Lee, X. W. Gu, W. C. Chueh, C. S. Yoon and Y.-K. Sun, *Energy Environ. Sci.*, 2021, **14**, 6616.
80 H.-H. Ryu, H.-W. Lim, S. G. Lee and Y.-K. Sun, *Energy Storage Mater.*, 2023, **59**, 102771.
81 D. Goonetilleke, A. Mazilkin, D. Weber, Y. Ma, F. Fauth, J. Janek, T. Brezesinski and M. Bianchini, *J. Mater. Chem. A*, 2022, **10**, 7841.
82 X. Li, W. Ge, K. Zhang, G. Peng, Y. Fu and X. Ma, *Electrochim. Acta*, 2022, **403**, 139653.
83 Y. Kim, H. Kim, W. Shin, E. Jo and A. Manthiram, *Adv. Energy Mater.*, 2023, **13**, 2204054.
84 L. Yao, Y. Li, X. Gao, M. Cai, J. Jin, J. Yang, T. Xiu, Z. Song, M. E. Badding and Z. Wen, *Energy Storage Mater.*, 2021, **36**, 179.
85 J. Wang, C. Liu, G. Xu, C. Miao, M. Wen, M. Xu, C. Wang and W. Xiao, *Chem. Eng. J.*, 2022, **438**, 135537.

86 S. Hashigami, Y. Kato, K. Yoshimi, A. Fukumoto, Z. Cao, H. Yoshida, T. Inagaki, M. Hashinokuchi, M. Haruta, T. Doi and M. Inaba, *ACS Appl. Mater. Interfaces*, 2019, **11**, 39910.
87 Y. Mo, L. Guo, H. Jin, B. Du, B. Cao, Y. Chen, D. Li and Y. Chen, *J. Power Sources*, 2020, **448**, 227439.
88 L. Li, L. Fu, M. Li, C. Wang, Z. Zhao, S. Xie, H. Lin, X. Wu, H. Liu, L. Zhang, Q. Zhang and L. Tan, *J. Energy Chem.*, 2022, **71**, 588.
89 S. F. Amalraj, R. Raman, A. Chakraborty, N. Leifer, R. Nanda, S. Kunnikuruvan, T. Kravchuk, J. Grinblat, V. Ezersky, R. Sun, F. L. Deepak, C. Erk, X. Wu, S. Maiti, H. Sclar, G. Goobes, D. T. Major, M. Talianker, B. Markovsky and D. Aurbach, *Energy Storage Mater.*, 2021, **42**, 594.
90 L. Cai, Q. Han, H. Zhu, H. Yu, Y. Hu and H. Jiang, *J. Mater. Chem. A*, 2023, **11**, 8352.
91 Y. B. Hendri, L.-Y. Kuo, M. Seenivasan, Y.-S. Wu, S.-H. Wu, J.-K. Chang, R. Jose, M. Ihrig, P. Kaghazchi and C.-C. Yang, *J. Colloid Interface Sci.*, 2024, **661**, 289.
92 J. Wang, Z. Yi, C. Liu, M. He, C. Miao, J. Li, G. Xu and W. Xiao, *J. Colloid Interface Sci.*, 2023, **635**, 295.
93 J. Cheng, L. Mu, C. Wang, Z. Yang, H. L. Xin, F. Lin and K. A. Persson, *J. Mater. Chem. A*, 2020, **8**, 23293.
94 Y. Lv, S. Huang, J. Zhang, G. Kang, Y. Liu, N. Li, Y. Liang, X. Zhong, T. Jia, Y. Ouyang, P. Qin, F. Kang, J. Zhang and Y. Cao, *Adv. Funct. Mater.*, 2024, **34**, 2312284.
95 Z.-C. Liu, S. Hao and X.-P. Gao, *ACS Appl. Mater. Interfaces*, 2023, **15**, 52552.
96 K. Huang, X. Mu, Y. Ding, J. Li, M. Sui and P. Yan, *ACS Appl. Energy Mater.*, 2024, **7**, 4856–4865.
97 U.-H. Kim, N.-Y. Park, G.-T. Park, H. Kim, C. S. Yoon and Y.-K. Sun, *Energy Storage Mater.*, 2020, **33**, 399.
98 G.-T. Park, H.-H. Ryu, T.-C. Noh, G.-C. Kang and Y.-K. Sun, *Mater. Today*, 2022, **52**, 9.
99 H.-H. Ryu, N.-Y. Park, T.-C. Noh, G.-C. Kang, F. Maglia, S.-J. Kim, C. S. Yoon and Y.-K. Sun, *ACS Energy Lett.*, 2021, **6**, 216.
100 I. A. Skvortsova, E. D. Orlova, A. O. Boev, D. A. Aksyonov, I. Moiseev, E. M. Pazhetnov, A. A. Savina and A. M. Abakumov, *J. Power Sources*, 2023, **583**, 233571.
101 L. Romano Brandt, J.-J. Marie, T. Moxham, D. P. Förstermann, E. Salvati, C. Besnard, C. Papadaki, Z. Wang, P. G. Bruce and A. M. Korsunsky, *Energy Environ. Sci.*, 2020, **13**, 3556.
102 T. Chen, C. Wen, C. Wu, L. Qiu, Z. Wu, J. Li, Y. Zhu, H. Li, Q. Kong, Y. Song, F. Wan, M. Chen, I. Saadoune, B. Zhong, S. Dou, Y. Xiao and X. Guo, *Chem. Sci.*, 2023, **14**, 13924.
103 D. Ren, E. Padgett, Y. Yang, L. Shen, Y. Shen, B. D. A. Levin, Y. Yu, F. J. DiSalvo, D. A. Muller and H. D. Abruña, *ACS Appl. Mater. Interfaces*, 2019, **11**, 41178.
104 J. M. Dake, J. Oddershede, H. O. Sørensen, T. Werz, J. C. Shatto, K. Uesugi, S. Schmidt and C. E. Krill, *Proc. Natl. Acad. Sci. U. S. A.*, 2016, **113**, E5998.
105 H. Sharma, R. M. Huizenga, A. Bytchkov, J. Sietsma and S. E. Offerman, *Acta Mater.*, 2012, **60**, 229.
106 U.-H. Kim, S.-B. Lee, J.-H. Ryu, C. S. Yoon and Y.-K. Sun, *J. Power Sources*, 2023, **564**, 232850.
107 X. He, S. Su, B. Zhang, Z. Xiao, Z. Zhang and X. Ou, *J. Energy Chem.*, 2024, **88**, 213.
108 X. Wang, C. Zhu, L. Ren, S. Wang, M. Zuo, W. Xing, W. Fan, B. Zhang, Z. Zheng, C. Shu and W. Xiang, *Energy Technol.*, 2023, **11**, 2300133.
109 Z. Wang, W. Wei, Q. Han, H. Zhu, L. Chen, Y. Hu, H. Jiang and C. Li, *ACS Nano*, 2023, **17**, 17095.
110 J. E. Burke and D. Turnbull, *Prog. Met. Phys.*, 1952, **3**, 220.
111 J. E. Burke, *J. Am. Chem. Soc.*, 1957, **40**, 80.
112 S. L. Dai, J. P. Delplanque and E. J. Lavernia, *J. Mater. Res.*, 1999, **14**, 2814.
113 S. H. Brodhag and M. Herwegh, *Contrib. Mineral. Petrol.*, 2010, **160**, 219.
114 Y. Lv, S. Huang, S. Lu, T. Jia, Y. Liu, W. Ding, X. Yu, F. Kang, J. Zhang and Y. Cao, *Chem. Eng. J.*, 2023, **455**, 140652.
115 T.-P. Gao, K. W. Wong and K. M. Ng, *Nano Energy*, 2020, **73**, 104798.
116 Y. S. Kim, J. H. Kim, Y.-K. Sun and C. S. Yoon, *ACS Appl. Mater. Interfaces*, 2022, **14**, 17500.
117 F. Fu, G.-L. Xu, Q. Wang, Y.-P. Deng, X. Li, J.-T. Li, L. Huang and S.-G. Sun, *J. Mater. Chem. A*, 2013, **1**, 3860.
118 A. O. Kondrakov, A. Schmidt, J. Xu, H. Geßwein, R. Mönig, P. Hartmann, H. Sommer, T. Brezesinski and J. Janek, *J. Phys. Chem. C*, 2017, **121**, 3286.
119 N.-Y. Park, G.-T. Park, S.-B. Kim, W. Jung, B.-C. Park and Y.-K. Sun, *ACS Energy Lett.*, 2022, **7**, 2362.
120 Y.-K. Hou, C. Li, D. Ren, F. He, K. Zhuang, S. Yin, G. Yuan, Y. Wang, Y. Guo, S. Liu, P. Sun, Z. Zhang, T. Tan, G. Zhu, L. Lu, X. Liu and M. Ouyang, *Adv. Sci.*, 2023, **10**, 2306347.
121 Z. Gao, C. Zhao, K. Zhou, J. Wu, Y. Tian, X. Deng, L. Zhang, K. Lin, F. Kang, L. Peng, M. Wagemaker and B. Li, *Nat. Commun.*, 2024, **15**, 1503.
122 Z. Xu, Z. Jiang, C. Kuai, R. Xu, C. Qin, Y. Zhang, M. M. Rahman, C. Wei, D. Nordlund, C.-J. Sun, X. Xiao, X.-W. Du, K. Zhao, P. Yan, Y. Liu and F. Lin, *Nat. Commun.*, 2020, **11**, 83.
123 S. Daubner, M. Weichel, P. W. Hoffrogge, D. Schneider and B. Nestler, *Batteries*, 2023, **9**, 310.
124 B.-B. Lim, S.-T. Myung, C. S. Yoon and Y.-K. Sun, *ACS Energy Lett.*, 2016, **1**, 283.
125 J. Hu, L. Li, E. Hu, S. Chae, H. Jia, T. Liu, B. Wu, Y. Bi, K. Amine, C. Wang, J. Zhang, J. Tao and J. Xiao, *Nano Energy*, 2021, **79**, 105420.
126 J. Kim, I. Lee, Y.-H. Kim, J. Ho Bae, K. Hwang, H. Kang, J.-H. Shim, J.-S. Kim, C. Wan Park, Y.-M. Kim and S. Yoon, *Chem. Eng. J.*, 2023, **455**, 140578.
127 H.-H. Sun, J. A. Weeks, A. Heller and C. B. Mullins, *ACS Appl. Energy Mater.*, 2019, **2**, 6002.
128 F. Tian, L. Ben, H. Yu, H. Ji, W. Zhao, Z. liu, R. Monteiro, R. M. Ribas, Y. Zhu and X. Huang, *Nano Energy*, 2022, **98**, 107222.
129 H.-H. Ryu, K.-J. Park, D. R. Yoon, A. Aishova, C. S. Yoon and Y.-K. Sun, *Adv. Energy Mater.*, 2019, **9**, 1902698.
130 X. Xu, H. Huo, J. Jian, L. Wang, H. Zhu, S. Xu, X. He, G. Yin, C. Du and X. Sun, *Adv. Energy Mater.*, 2019, **9**, 1803963.
131 S. Xia, L. Mu, Z. Xu, J. Wang, C. Wei, L. Liu, P. Pianetta, K. Zhao, X. Yu, F. Lin and Y. Liu, *Nano Energy*, 2018, **53**, 753.

132 G.-T. Park, H. H. Sun, T.-C. Noh, F. Maglia, S.-J. Kim, P. Lamp and Y.-K. Sun, *Adv. Energy Mater.*, 2022, **12**, 2202719.
133 C. Tian, Y. Xu, D. Nordlund, F. Lin, J. Liu, Z. Sun, Y. Liu and M. Doeff, *Joule*, 2018, **2**, 464.
134 J. Li, J. Huang, H. Li, X. Kong, X. Li and J. Zhao, *ACS Appl. Mater. Interfaces*, 2021, **13**, 27074.
135 L. Mu, J. Zhang, Y. Xu, C. Wei, M. M. Rahman, D. Nordlund, Y. Liu and F. Lin, *Nano Lett.*, 2022, **22**, 1278.
136 H. Liu, M. Wolfman, K. Karki, Y.-S. Yu, E. A. Stach, J. Cabana, K. W. Chapman and P. J. Chupas, *Nano Lett.*, 2017, **17**, 3452.
137 D.-S. Ko, J.-H. Park, S. Park, Y. N. Ham, S. J. Ahn, J.-H. Park, H. N. Han, E. Lee, W. S. Jeon and C. Jung, *Nano Energy*, 2019, **56**, 434.
138 U. H. Kim, D. W. Jun, K. J. Park, Q. Zhang, P. Kaghazchi, D. Aurbach, D. T. Major, G. Goobes, M. Dixit, N. Leifer, C. M. Wang, P. Yan, D. Ahn, K. H. Kim, C. S. Yoon and Y. K. Sun, *Energy Environ. Sci.*, 2018, **11**, 1271.
139 S. Watanabe, M. Kinoshita, T. Hosokawa, K. Morigaki and K. Nakura, *J. Power Sources*, 2014, **258**, 210.
140 S. S. Zhang, *Energy Storage Mater.*, 2020, **24**, 247.
141 M. Jiang, D. L. Danilov, R.-A. Eichel and P. H. L. Notten, *Adv. Energy Mater.*, 2021, **11**, 2103005.
142 S.-K. Jung, H. Gwon, J. Hong, K.-Y. Park, D.-H. Seo, H. Kim, J. Hyun, W. Yang and K. Kang, *Adv. Energy Mater.*, 2014, **4**, 1300787.
143 C. Xu, K. Märker, J. Lee, A. Mahadevegowda, P. J. Reeves, S. J. Day, M. F. Groh, S. P. Emge, C. Ducati, B. Layla Mehdi, C. C. Tang and C. P. Grey, *Nat. Mater.*, 2021, **20**, 84.
144 P. Yan, J. Zheng, Z.-K. Tang, A. Devaraj, G. Chen, K. Amine, J.-G. Zhang, L.-M. Liu and C. Wang, *Nat. Nanotechnol.*, 2019, **14**, 602.
145 P. Yan, J. Zheng, T. Chen, L. Luo, Y. Jiang, K. Wang, M. Sui, J.-G. Zhang, S. Zhang and C. Wang, *Nat. Commun.*, 2018, **9**, 2437.
146 G.-T. Park, H.-H. Ryu, N.-Y. Park, C. S. Yoon and Y.-K. Sun, *J. Power Sources*, 2019, **442**, 227242.
147 Z. Guo, X. Shi, L. Cao, J. Zhang, X. Zhang, J. Yao, Y.-J. Cheng and Y. Xia, *ACS Appl. Mater. Interfaces*, 2024, **16**, 731.
148 K. Chen, P. Barai, O. Kahvecioglu, L. Wu, K. Z. Pupek, M. Ge, L. Ma, S. N. Ehrlich, H. Zhong, Y. Zhu, V. Srinivasan, J. Bai and F. Wang, *Nat. Commun.*, 2024, **15**, 430.
149 P. Kurzhals, F. Riewald, M. Bianchini, H. Sommer, H. A. Gasteiger and J. Janek, *J. Electrochem. Soc.*, 2021, **168**, 110518.
150 L. Yu, H. Zhao, J. Sun, Q. Han, J. Zhu and J. Lu, *Adv. Funct. Mater.*, 2022, **32**, 2204931.
151 U.-H. Kim, J.-H. Kim, J.-Y. Hwang, H.-H. Ryu, C. S. Yoon and Y.-K. Sun, *Mater. Today*, 2019, **23**, 26.
152 F. Fan, R. Zheng, T. Zeng, H. Xu, X. Wen, X. Wang, G. Tian, S. Wang, C. Zeng, W. Xiang and C. Shu, *Chem. Eng. J.*, 2023, **477**, 147181.
153 N.-Y. Park, G. Cho, S.-B. Kim and Y.-K. Sun, *Adv. Energy Mater.*, 2023, **13**, 2204291.
154 U.-H. Kim, G.-T. Park, P. Conlin, N. Ashburn, K. Cho, Y.-S. Yu, D. A. Shapiro, F. Maglia, S.-J. Kim, P. Lamp, C. S. Yoon and Y.-K. Sun, *Energy Environ. Sci.*, 2021, **14**, 1573.
155 X. Mu, X. Hui, M. Wang, K. Wang, Y. Li, Y. Zhang, M. Sui and P. Yan, *ACS Appl. Energy Mater.*, 2023, **6**, 5018.
156 J. Oh, S.-Y. Lee, H. Kim, J. Ryu, B. Gil, J. Lee and M. Kim, *Adv. Sci.*, 2022, **9**, 2203639.
157 Q. Lin, W. Guan, J. Zhou, J. Meng, W. Huang, T. Chen, Q. Gao, X. Wei, Y. Zeng, J. Li and Z. Zhang, *Nano Energy*, 2020, **76**, 105021.
158 Y. Jiang, P. Yan, M. Yu, J. Li, H. Jiao, B. Zhou and M. Sui, *Nano Energy*, 2020, **78**, 105364.
159 H. Chung, Y. Li, M. Zhang, A. Grenier, C. Mejia, D. Cheng, B. Sayahpour, C. Song, M. H. Shen, R. Huang, E. A. Wu, K. W. Chapman, S. J. Kim and Y. S. Meng, *Chem. Mater.*, 2022, **34**, 7302.
160 C. S. Yoon, S. J. Kim, U.-H. Kim, K.-J. Park, H.-H. Ryu, H.-S. Kim and Y.-K. Sun, *Adv. Funct. Mater.*, 2018, **28**, 1802090.
161 M. Legros, G. Dehm, E. Arzt and T. J. Balk, *Science*, 2008, **319**, 1646.
162 L. de Biasi, B. Schwarz, T. Brezesinski, P. Hartmann, J. Janek and H. Ehrenberg, *Adv. Mater.*, 2019, **31**, 1900985.
163 L. Liang, W. Zhang, F. Zhao, D. K. Denis, F. U. Zaman, L. Hou and C. Yuan, *Adv. Mater. Interfaces*, 2020, **7**, 1901749.
164 C. Yang, R. Shao, Q. Wang, T. Zhou, J. Lu, N. Jiang, P. Gao, W. Liu, Y. Yu and H. Zhou, *Energy Storage Mater.*, 2021, **35**, 62.
165 S. Y. Park, W. J. Baek, S. Y. Lee, J. A. Seo, Y.-S. Kang, M. Koh and S. H. Kim, *Nano Energy*, 2018, **49**, 1.
166 S. E. Renfrew and B. D. McCloskey, *J. Am. Chem. Soc.*, 2017, **139**, 17853.
167 A. T. S. Freiberg, J. Sicklinger, S. Solchenbach and H. A. Gasteiger, *Electrochim. Acta*, 2020, **346**, 136271.
168 W. M. Dose, I. Temprano, J. P. Allen, E. Björklund, C. A. O'Keefe, W. Li, B. L. Mehdi, R. S. Weatherup, M. F. L. De Volder and C. P. Grey, *ACS Appl. Mater. Interfaces*, 2022, **14**, 13206.
169 J. Hu, L. Li, Y. Bi, J. Tao, J. Lochala, D. Liu, B. Wu, X. Cao, S. Chae, C. Wang and J. Xiao, *Energy Storage Mater.*, 2022, **47**, 195.
170 L. Ni, H. Chen, J. Gao, Y. Mei, H. Wang, W. Deng, G. Zou, H. Hou and X. Ji, *ACS Nano*, 2023, **17**, 12759.
171 J. Kim, H. Ma, H. Cha, H. Lee, J. Sung, M. Seo, P. Oh, M. Park and J. Cho, *Energy Environ. Sci.*, 2018, **11**, 1449.
172 H.-H. Ryu, H.-W. Lim, G.-C. Kang, N.-Y. Park and Y.-K. Sun, *ACS Energy Lett.*, 2023, **8**, 1354.
173 B. Namkoong, N.-Y. Park, G.-T. Park, J.-Y. Shin, T. Beierling, C. S. Yoon and Y.-K. Sun, *Adv. Energy Mater.*, 2022, **12**, 2200615.
174 C. F. Lopez, J. A. Jeevarajan and P. P. Mukherjee, *J. Electrochem. Soc.*, 2015, **162**, A1905.
175 P. Lyu, X. Liu, J. Qu, J. Zhao, Y. Huo, Z. Qu and Z. Rao, *Energy Storage Mater.*, 2020, **31**, 195.
176 S. Mallick and D. Gayen, *J. Energy Storage*, 2023, **62**, 106894.
177 P. T. Coman, E. C. Darcy, C. T. Veje and R. E. White, *Appl. Energy*, 2017, **203**, 189.

178 Y. Li, X. Liu, L. Wang, X. Feng, D. Ren, Y. Wu, G. Xu, L. Lu, J. Hou, W. Zhang, Y. Wang, W. Xu, Y. Ren, Z. Wang, J. Huang, X. Meng, X. Han, H. Wang, X. He, Z. Chen, K. Amine and M. Ouyang, *Nano Energy*, 2021, **85**, 105878.
179 P. V. Chombo and Y. Laoonual, *J. Power Sources*, 2020, **478**, 228649.
180 F. Kong, C. Liang, L. Wang, Y. Zheng, S. Perananthan, R. C. Longo, J. P. Ferraris, M. Kim and K. Cho, *Adv. Energy Mater.*, 2019, **9**, 1802586.
181 S. Sharifi-Asl, J. Lu, K. Amine and R. Shahbazian-Yassar, *Adv. Energy Mater.*, 2019, **9**, 1900551.
182 S. Yoon, H. G. Park, S. Koo, J. Hwang, Y. Lee, K. Park and D. Kim, *J. Alloys Compd.*, 2023, **939**, 168531.
183 P. Hou, F. Li, Y. Sun, H. Li, X. Xu and T. Zhai, *ACS Appl. Mater. Interfaces*, 2018, **10**, 24508.
184 D. Song, P. Hou, X. Wang, X. Shi and L. Zhang, *ACS Appl. Mater. Interfaces*, 2015, **7**, 12864.
185 P. Y. Hou, L. Q. Zhang and X. P. Gao, *J. Mater. Chem. A*, 2014, **2**, 17130.
186 J.-Y. Liao and A. Manthiram, *J. Power Sources*, 2015, **282**, 429.
187 J.-L. Shi, R. Qi, X.-D. Zhang, P.-F. Wang, W.-G. Fu, Y.-X. Yin, J. Xu, L.-J. Wan and Y.-G. Guo, *ACS Appl. Mater. Interfaces*, 2017, **9**, 42829.
188 S.-J. Yoon, S.-T. Myung, H.-J. Noh, J. Lu, K. Amine and Y.-K. Sun, *ChemSusChem*, 2014, **7**, 3295.
189 U.-H. Kim, S.-B. Lee, N.-Y. Park, S. J. Kim, C. S. Yoon and Y.-K. Sun, *ACS Energy Lett.*, 2022, **7**, 3880.
190 B. Wang, F. Cai, C. Chu, B. Fu, K. Świerczek, L. Li and H. Zhao, *ACS Appl. Mater. Interfaces*, 2024, **16**, 12599.
191 A. Schilling, J. Schmitt, F. Dietrich and K. Dröder, *Energy Technol.*, 2016, **4**, 1502.
192 H.-Y. Tran, A. Lindner, W. Menesklou and W. Braunwarth, *Energy Technol.*, 2023, **11**, 2201092.
193 J. C. Stallard, L. Wheatcroft, S. G. Booth, R. Boston, S. A. Corr, M. F. L. De Volder, B. J. Inkson and N. A. Fleck, *Joule*, 2022, **6**, 984.
194 M. Müller, L. Schneider, N. Bohn, J. R. Binder and W. Bauer, *ACS Appl. Energy Mater.*, 2021, **4**, 1993.
195 R. Xu, H. Sun, L. S. de Vasconcelos and K. Zhao, *J. Electrochem. Soc.*, 2017, **164**, A3333.
196 H.-R. Kim, S.-G. Woo, J.-H. Kim, W. Cho and Y.-J. Kim, *J. Electroanal. Chem.*, 2016, **782**, 168.
197 J. Moon, J. Y. Jung, T. D. Hoang, D. Y. Rhee, H. B. Lee, M.-S. Park and J.-S. Yu, *J. Power Sources*, 2021, **486**, 229359.
198 S. Maeng, Y. Chung, S. Min and Y. Shin, *J. Power Sources*, 2020, **448**, 227395.
199 Z. Huang, J. Yan, Z. Liu, W. Wang, Y. Tang, Z. Zhang, T. Yang, X. Wang, X. Li, Q. Kong, S. Lan, H. Zhu, Y. Ren and Q. Liu, *Adv. Funct. Mater.*, 2024, **34**, 2400956.
200 T. Karthik and S. Asthana, *Mater. Lett.*, 2017, **190**, 273.
201 J. Poetschke, V. Richter and R. Holke, *Int. J. Refract. Met. Hard Mater.*, 2012, **31**, 218.
202 I. A. Ovid'ko and A. G. Sheinerman, *Acta Mater.*, 2004, **52**, 1201.
203 I. A. Ovid'ko, *Philos. Trans. R. Soc., A*, 2015, **373**, 20140129.
204 G.-T. Park, S.-M. Han, J.-H. Ryu, M.-C. Kim, D.-H. Kim, M.-S. Kim and Y.-K. Sun, *ACS Energy Lett.*, 2023, **8**, 3784.
205 S.-B. Lee, N.-Y. Park, G.-T. Park, U.-H. Kim, S.-J. Sohn, M.-S. Kang, R. M. Ribas, R. S. Monteiro and Y.-K. Sun, *ACS Energy Lett.*, 2024, **9**, 740.
206 S.-H. Lee, B.-S. Jin and H.-S. Kim, *Sci. Rep.*, 2019, **9**, 17541.
207 Z. Li, X. Huang, J. Liang, J. Qin, R. Wang, J. Cheng and D. Wang, *J. Energy Chem.*, 2023, **77**, 461.
208 X. Chen, X. Jia, Y. Qu, D. Li, D. Chen and Y. Chen, *New J. Chem.*, 2018, **42**, 5868.
209 L. Chang, Y. Lu, D. Lei, H. Liu, L. He, Y. Ni and Y. Li, *J. Power Sources*, 2021, **494**, 229777.
210 W. Hua, Z. Wu, M. Chen, M. Knapp, X. Guo, S. Indris, J. R. Binder, N. N. Bramnik, B. Zhong, H. Guo, S. Chou, Y.-M. Kang and H. Ehrenberg, *J. Mater. Chem. A*, 2017, **5**, 25391.
211 J. Zheng, P. Yan, L. Estevez, C. Wang and J.-G. Zhang, *Nano Energy*, 2018, **49**, 538.
212 S. Yang, B. Yan, L. Lu and K. Zeng, *RSC Adv.*, 2016, **6**, 94000.
213 C. Schwab, A. Höweling, A. Windmüller, J. Gonzalez-Julian, S. Möller, J. R. Binder, S. Uhlenbruck, O. Guillon and M. Martin, *Phys. Chem. Chem. Phys.*, 2019, **21**, 26066.
214 Y. Liu, Y. Zhu and Y. Cui, *Nat. Energy*, 2019, **4**, 540.
215 C. Mao, R. E. Ruther, J. Li, Z. Du and I. Belharouak, *Electrochem. Commun.*, 2018, **97**, 37.
216 M. Weiss, R. Ruess, J. Kasnatscheew, Y. Levartovsky, N. R. Levy, P. Minnmann, L. Stolz, T. Waldmann, M. Wohlfahrt-Mehrens, D. Aurbach, M. Winter, Y. Ein-Eli and J. Janek, *Adv. Energy Mater.*, 2021, **11**, 2101126.
217 Z. Yang, H. Charalambous, Y. Lin, S. E. Trask, L. Yu, J. Wen, A. Jansen, Y. Tsai, K. M. Wiaderek, Y. Ren and I. Bloom, *J. Power Sources*, 2022, **521**, 230961.
218 L. Zou, W. Zhao, Z. Liu, H. Jia, J. Zheng, G. Wang, Y. Yang, J.-G. Zhang and C. Wang, *ACS Energy Lett.*, 2018, **3**, 2433.
219 J. Hu, B. Wu, X. Cao, Y. Bi, S. Chae, C. Niu, B. Xiao, J. Tao, J. Zhang and J. Xiao, *J. Power Sources*, 2020, **454**, 227966.
220 S. Ma, X. Zhang, S. Wu, E. Fan, J. Lin, R. Chen, F. Wu and L. Li, *Energy Storage Mater.*, 2023, **55**, 556.
221 J.-M. Lim, T. Hwang, D. Kim, M.-S. Park, K. Cho and M. Cho, *Sci. Rep.*, 2017, **7**, 39669.
222 Y. Zhang, Z. Yang and C. Tian, *J. Mater. Chem. A*, 2019, **7**, 23628.
223 Y. Yang, R. Xu, K. Zhang, S.-J. Lee, L. Mu, P. Liu, C. K. Waters, S. Spence, Z. Xu, C. Wei, D. J. Kautz, Q. Yuan, Y. Dong, Y.-S. Yu, X. Xiao, H.-K. Lee, P. Pianetta, P. Cloetens, J.-S. Lee, K. Zhao, F. Lin and Y. Liu, *Adv. Energy Mater.*, 2019, **9**, 1900674.
224 T. Liu, L. Yu, J. Lu, T. Zhou, X. Huang, Z. Cai, A. Dai, J. Gim, Y. Ren, X. Xiao, M. V. Holt, Y. S. Chu, I. Arslan, J. Wen and K. Amine, *Nat. Commun.*, 2021, **12**, 6024.
225 Y. Xia, A. Chen, K. Wang, Z. Xiao, Q. Mao, X. Lu, G. Wang, C. Lu, J. Zhang, H. Huang, Y. Gan, X. He, X. Xia and W. Zhang, *Mater. Today Energy*, 2023, **34**, 101292.
226 X. Cheng, Y. Li, G. Zhao, W. Qiang and B. Huang, *Ceram. Int.*, 2022, **48**, 27849.

227 L. A. Sitnikova, A. A. Savina, A. V. Morozov, A. A. Golubnichiy, E. A. Dolzhikova, I. A. Moiseev, S. Y. Luchkin and A. M. Abakumov, *J. Power Sources*, 2024, **602**, 234302.
228 Y. Mo, L. Guo, H. Jin, B. Du, B. Cao, Y. Chen, D. Li and Y. Chen, *J. Power Sources*, 2020, **468**, 228405.
229 R. Yang, Z. Wang, L. Dai and L. Chen, *Mater. Chem. Phys.*, 2005, **93**, 149.
230 Z. Li, H. Bao, X. Miao and X. Chen, *J. Colloid Interface Sci.*, 2011, **357**, 286.
231 N.-Y. Park, H.-H. Ryu, L.-Y. Kuo, P. Kaghazchi, C. S. Yoon and Y.-K. Sun, *ACS Energy Lett.*, 2021, **6**, 4195.
232 Y.-K. Sun, S.-T. Myung, M.-H. Kim, J. Prakash and K. Amine, *J. Am. Chem. Soc.*, 2005, **127**, 13411.
233 Y.-K. Sun, S.-T. Myung, H.-S. Shin, Y. C. Bae and C. S. Yoon, *J. Phys. Chem. B*, 2006, **110**, 6810.
234 Y.-K. Sun, D.-H. Kim, C. S. Yoon, S.-T. Myung, J. Prakash and K. Amine, *Adv. Funct. Mater.*, 2010, **20**, 485.
235 L. de Biasi, A. O. Kondrakov, H. Geßwein, T. Brezesinski, P. Hartmann and J. Janek, *J. Phys. Chem. C*, 2017, **121**, 26163.
236 W. Li, H. Y. Asl, Q. Xie and A. Manthiram, *J. Am. Chem. Soc.*, 2019, **141**, 5097.
237 B.-B. Lim, S.-J. Yoon, K.-J. Park, C. S. Yoon, S.-J. Kim, J. J. Lee and Y.-K. Sun, *Adv. Funct. Mater.*, 2015, **25**, 4673.
238 J. H. Lee, C. S. Yoon, J.-Y. Hwang, S.-J. Kim, F. Maglia, P. Lamp, S.-T. Myung and Y.-K. Sun, *Energy Environ. Sci.*, 2016, **9**, 2152.
239 H. Wu, X. Zhou, C. Yang, D. Xu, Y.-H. Zhu, T. Zhou, S. Xin and Y. You, *ACS Appl. Mater. Interfaces*, 2023, **15**, 18828.
240 H.-H. Ryu, H.-W. Lim, S. G. Lee and Y.-K. Sun, *Nat. Energy*, 2024, **9**, 47.
241 N.-Y. Park, S.-B. Kim, M.-C. Kim, S.-M. Han, D.-H. Kim, M.-S. Kim and Y.-K. Sun, *Adv. Energy Mater.*, 2023, **13**, 2301530.
242 C. Geng, D. Rathore, D. Heino, N. Zhang, I. Hamam, N. Zaker, G. A. Botton, R. Omessi, N. Phattharasupakun, T. Bond, C. Yang and J. R. Dahn, *Adv. Energy Mater.*, 2021, **12**, 2103067.
243 F. Lv, Y. Zhang, M. Wu and Y. Gu, *Appl. Phys. Lett.*, 2021, **119**, 023903.
244 S. Lee, H. W. Park, J. P. Hong, S.-C. Nam, D. H. Jeon and J.-H. Song, *Solid State Ionics*, 2022, **386**, 116042.
245 X. Yang, Y. Tang, J. Zheng, G. Shang, J. Wu, Y. Lai, J. Li and Z. Zhang, *Electrochim. Acta*, 2019, **320**, 134587.
246 C.-K. Yang, L.-Y. Qi, Z. Zuo, R.-N. Wang, M. Ye, J. Lu and H.-H. Zhou, *J. Power Sources*, 2016, **331**, 487.
247 B. Du, Y. Mo, H. Jin, X. Li, Y. Qu, D. Li, B. Cao, X. Jia, Y. Lu and Y. Chen, *ACS Appl. Energy Mater.*, 2020, **3**, 6657.
248 D. Han, J. Zhang, M. Yang, K. Xie, J. Peng, O. Dolotko, C. Huang, Y. Wu, L. Shao, W. Hua and W. Tang, *Energy Mater.*, 2024, **4**, 400001.
249 B. Ying, J. R. Fitzpatrick, Z. Teng, T. Chen, T. W. B. Lo, V. Siozios, C. A. Murray, H. E. A. Brand, S. Day, C. C. Tang, R. S. Weatherup, M. Merz, P. Nagel, S. Schuppler, M. Winter and K. Kleiner, *Chem. Mater.*, 2023, **35**, 1514.
250 J. Guo and W. Li, *ACS Appl. Energy Mater.*, 2022, **5**, 397.
251 Z. Zhang, D. Chen and C. Chang, *RSC Adv.*, 2017, **7**, 51721.
252 D. Rathore, C. Geng, N. Zaker, I. Hamam, Y. Liu, P. Xiao, G. A. Botton, J. Dahn and C. Yang, *J. Electrochem. Soc.*, 2021, **168**, 120514.
253 B. Huang, L. Cheng, X. Li, Z. Zhao, J. Yang, Y. Li, Y. Pang and G. Cao, *Small*, 2022, **18**, 2107697.
254 S. Lee, C. Li and A. Manthiram, *Adv. Energy Mater.*, 2024, **14**, 2400662.
255 D. Wang, C. Xin, M. Zhang, J. Bai, J. Zheng, R. Kou, J. Y. Peter Ko, A. Huq, G. Zhong, C.-J. Sun, Y. Yang, Z. Chen, Y. Xiao, K. Amine, F. Pan and F. Wang, *Chem. Mater.*, 2019, **31**, 2731.
256 M. J. Zhang, G. Teng, Y. K. Chen-Wiegart, Y. Duan, J. Y. P. Ko, J. Zheng, J. Thieme, E. Dooryhee, Z. Chen, J. Bai, K. Amine, F. Pan and F. Wang, *J. Am. Chem. Soc.*, 2018, **140**, 12484.
257 H.-H. Ryu, G.-T. Park, C. S. Yoon and Y.-K. Sun, *J. Mater. Chem. A*, 2019, **7**, 18580.
258 M. Bianchini, M. Roca-Ayats, P. Hartmann, T. Brezesinski and J. Janek, *Angew. Chem., Int. Ed.*, 2019, **58**, 10434.
259 F. Xin, H. Zhou, Y. Zong, M. Zuba, Y. Chen, N. A. Chernova, J. Bai, B. Pei, A. Goel, J. Rana, F. Wang, K. An, L. F. J. Piper, G. Zhou and M. S. Whittingham, *ACS Energy Lett.*, 2021, **6**, 1377.
260 C. Liang, F. Kong, R. C. Longo, C. Zhang, Y. Nie, Y. Zheng and K. Cho, *J. Mater. Chem. A*, 2017, **5**, 25303.
261 F. Xin, A. Goel, X. Chen, H. Zhou, J. Bai, S. Liu, F. Wang, G. Zhou and M. S. Whittingham, *Chem. Mater.*, 2022, **34**, 7858.
262 L. Mu, R. Zhang, W. H. Kan, Y. Zhang, L. Li, C. Kuai, B. Zydlewski, M. M. Rahman, C.-J. Sun, S. Sainio, M. Avdeev, D. Nordlund, H. L. Xin and F. Lin, *Chem. Mater.*, 2019, **31**, 9769.
263 Y. Zhang, J. Liu, W. Xu, Y. Lu, H. Ma, F. Cheng and J. Chen, *J. Power Sources*, 2022, **535**, 231445.
264 Y. Y. Wang, M. Y. Gao, S. Liu, G. R. Li and X. P. Gao, *ACS Appl. Mater. Interfaces*, 2021, **13**, 7343.
265 H.-H. Ryu, H. H. Sun, S.-T. Myung, C. S. Yoon and Y.-K. Sun, *Energy Environ. Sci.*, 2021, **14**, 844.
266 J. L. Matthew Li, *Science*, 2020, **367**, 979.
267 H.-H. Ryu, G.-C. Kang, R. Ismoyojati, G.-T. Park, F. Maglia and Y.-K. Sun, *Mater. Today*, 2022, **56**, 8–15.
268 F. Tian, Y. Zhang, Z. Liu, R. de Souza Monteiro, R. M. Ribas, P. Gao, Y. Zhu, H. Yu, L. Ben and X. Huang, *Solid State Ionics*, 2021, **359**, 115520.
269 F. Du, Q. Zhou, H. Cao, H. Dai, D. Hu, P. Sun, J. Adkins and J. Zheng, *J. Power Sources*, 2020, **478**, 228737.
270 K. Zou, M. Jiang, Z. Zhao, S. Xie, T. Ning, L. Tan, H. Li, Y. Zhou, W. Wang, X. Wu and L. Li, *Chem. Eng. J.*, 2023, **476**, 146793.
271 P. Yan, J. Zheng, J. Liu, B. Wang, X. Cheng, Y. Zhang, X. Sun, C. Wang and J.-G. Zhang, *Nat. Energy*, 2018, **3**, 600.
272 G.-T. Park, S.-B. Kim, B. Namkoong, J.-H. Ryu, J.-I. Yoon, N.-Y. Park, M.-C. Kim, S.-M. Han, F. Maglia and Y.-K. Sun, *Angew. Chem., Int. Ed.*, 2023, **62**, e202314480.
273 J. G. Chen, B. D. De Vries, J. T. Lewandowski and R. B. Hall, *Catal. Lett.*, 1994, **23**, 25.
274 T. Nohma, H. Kurokawa, M. Uehara, M. Takahashi, K. Nishio and T. Saito, *J. Power Sources*, 1995, **54**, 522.

275 R. Jung, R. Morasch, P. Karayaylali, K. Phillips, F. Maglia, C. Stinner, Y. Shao-Horn and H. A. Gasteiger, *J. Electrochem. Soc.*, 2018, **165**, A132.
276 H. S. Liu, Z. R. Zhang, Z. L. Gong and Y. Yang, *Electrochem. Solid-State Lett.*, 2004, **7**, A190.
277 Y. Bi, Q. Li, R. Yi and J. Xiao, *J. Electrochem. Soc.*, 2022, **169**, 020521.
278 W. M. Seong, K.-H. Cho, J.-W. Park, H. Park, D. Eum, M. H. Lee, I.-S. S. Kim, J. Lim and K. Kang, *Angew. Chem., Int. Ed.*, 2020, **59**, 18662.
279 Z. Fan, F. Du, Q. Zhou, D. Hu, P. Sun, C. Mei, Q. Hao, T. Xu and J. Zheng, *J. Power Sources*, 2022, **523**, 231044.
280 N. V. Faenza, L. Bruce, Z. W. Lebens-Higgins, I. Plitz, N. Pereira, L. F. J. Piper and G. G. Amatucci, *J. Electrochem. Soc.*, 2017, **164**, A3727.
281 J. Kim, Y. Hong, K. S. Ryu, M. G. Kim and J. Cho, *Electrochem. Solid-State Lett.*, 2006, **9**, A19.
282 X. Xiong, Z. Wang, P. Yue, H. Guo, F. Wu, J. Wang and X. Li, *J. Power Sources*, 2013, **222**, 318.
283 J.-H. Park, B. Choi, Y.-S. Kang, S. Y. Park, D. J. Yun, I. Park, J. H. Shim, J.-H. Park, H. N. Han and K. Park, *Energy Technol.*, 2018, **6**, 1361.
284 K. Park and B. Choi, *J. Alloys Compd.*, 2018, **766**, 470.
285 I. A. Shkrob, J. A. Gilbert, P. J. Phillips, R. Klie, R. T. Haasch, J. Bareño and D. P. Abraham, *J. Electrochem. Soc.*, 2017, **164**, A1489.
286 L. Hartmann, D. Pritzl, H. Beyer and H. A. Gasteiger, *J. Electrochem. Soc.*, 2021, **168**, 070507.
287 W. Lee, S. Lee, E. Lee, M. Choi, R. Thangavel, Y. Lee and W.-S. Yoon, *Energy Storage Mater.*, 2022, **44**, 441.
288 J. Pan, Y. Sun, P. Wan, Z. Wang and X. Liu, *Electrochem. Commun.*, 2005, **7**, 857.
289 Y. Gao, R. Jiang, Z. Dai, Z. Du, Y. Jin, G. Li and S. Hou, *ACS Appl. Energy Mater.*, 2022, **5**, 15069.
290 D. Weber, Đ. Tripković, K. Kretschmer, M. Bianchini and T. Brezesinski, *Eur. J. Inorg. Chem.*, 2020, 3117.
291 W. Wang, L. Wu, Z. Li, K. Huang, J. Jiang, Z. Chen, X. Qi, H. Dou and X. Zhang, *ACS Appl. Energy Mater.*, 2020, **3**, 12423.
292 T. Sattar, S.-J. Sim, B.-S. Jin and H.-S. Kim, *Sci. Rep.*, 2021, **11**, 18590.
293 J. Park, Y. Kim, Y. Kim, J. Park, D. G. Lee, Y. Lee, J. Hwang, K.-Y. Park and D. Lee, *Chem. Eng. J.*, 2023, **467**, 143335.
294 J. Li, J. Xiang, G. Yi, Y. Tang, H. Shao, X. Liu, B. Shan and R. Chen, *Coatings*, 2022, **12**, 84.
295 Y.-H. Du, H. Sheng, X.-H. Meng, X.-D. Zhang, Y.-G. Zou, J.-Y. Liang, M. Fan, F. Wang, J. Tang, F.-F. Cao, J.-L. Shi, X.-F. Cao and Y.-G. Guo, *Nano Energy*, 2022, **94**, 106901.
296 Y. Xie, J. Li, M. Li, J. Cai, X. Huang, H. Nguyen, L. Yu, D. Huo, Z. Yang, N. Karami, B. A. S. Sulaiman, N. A. Chernova, S. Upreti, B. Prevel, Y. Liu, F. Wang and Z. Chen, *Adv. Funct. Mater.*, 2024, **34**, 2311551.
297 Y. Xie, M. Li, J. Li, X. Huang, J. Cai, Z. Yang, H. Nguyen, B. A. Shaik Sulaiman, N. Karami, N. A. Chernova, S. Upreti, B. Prevel, F. Wang and Z. Chen, *Batteries*, 2023, **9**, 485.
298 South Korea's Battery Industry Speeding up the Process of Transitioning to the ''Cobalt Zero'' Era, **https://english.etnews.com/20200828200001**, (accessed July 2024).
299 Kona EV Fires Underline Safety of SK Innovation's Batteries, **https://www.businesskorea.co.kr/news/articleView.html?idxno=53563#google_vignette**, (accessed July 2024).
300 SK On to jointly invest in cathode material production facility with Ford and EcoPro BM, **https://skinnonews.com/global/archives/10835**, (accessed July 2024).
301 ECOPROBM, SK ON, FORD INVESTING IN QUÉBEC; BUILDING CATHODE PLANT TO SOLIDIFY EV SUPPLY CHAIN IN NORTH AMERICA, **https://media.ford.com/content/fordmedia/fna/us/en/news/2023/08/17/ecoprobm--sk-on--ford-investing-in-quebec--building-cathode-plan.html**, (accessed July 2024).
302 U.-H. Kim, E.-J. Lee, C. S. Yoon, S.-T. Myung and Y.-K. Sun, *Adv. Energy Mater.*, 2016, **6**, 1601417.
303 N.-Y. Park, M.-C. Kim, S.-M. Han, G.-T. Park, D.-H. Kim, M.-S. Kim and Y.-K. Sun, *Angew. Chem., Int. Ed.*, 2024, **63**, e202319707.
304 K.-J. Park, J.-Y. Hwang, H.-H. Ryu, F. Maglia, S.-J. Kim, P. Lamp, C. S. Yoon and Y.-K. Sun, *ACS Energy Lett.*, 2019, **4**, 1394.
305 C. Wang, J. T. Kim, C. Wang and X. Sun, *Adv. Mater.*, 2023, **35**, e2209074.
306 Z. Zhang, W. Jia, Y. Feng, R. Ai, J. Yu, X. Bie, X. Zhai, T. Jiang, S. Yao and F. Du, *Energy Environ. Sci.*, 2023, **16**, 4453.
307 A. Banerjee, X. Wang, C. Fang, E. A. Wu and Y. S. Meng, *Chem. Rev.*, 2020, **120**, 6878.
308 T.-Y. Yu, H.-U. Lee, J. W. Lee, S.-M. Park, I.-S. Lee, H.-G. Jung and Y.-K. Sun, *J. Mater. Chem. A*, 2023, **11**, 24629.
309 S. Schweidler, L. de Biasi, G. Garcia, A. Mazilkin, P. Hartmann, T. Brezesinski and J. Janek, *ACS Appl. Energy Mater.*, 2019, **2**, 7375.
310 Y. Zhu, X. He and Y. Mo, *ACS Appl. Mater. Interfaces*, 2015, **7**, 23685.
311 Y. Nomura, K. Yamamoto, T. Hirayama, E. Igaki and K. Saitoh, *ACS Energy Lett.*, 2020, **5**, 2098.
312 J. Kim, W. Lee, J. Seok, E. Lee, W. Choi, H. Park, S. Yun, M. Kim, J. Lim and W.-S. Yoon, *J. Energy Chem.*, 2022, **66**, 226.
313 R. Koerver, W. Zhang, L. de Biasi, S. Schweidler, A. O. Kondrakov, S. Kolling, T. Brezesinski, P. Hartmann, W. G. Zeier and J. Janek, *Energy Environ. Sci.*, 2018, **11**, 2142.
314 S. H. Jung, U. H. Kim, J. H. Kim, S. Jun, C. S. Yoon, Y. S. Jung and Y. K. Sun, *Adv. Energy Mater.*, 2019, **10**, 1903360.
315 U.-H. Kim, T.-Y. Yu, J. W. Lee, H. U. Lee, I. Belharouak, C. S. Yoon and Y.-K. Sun, *ACS Energy Lett.*, 2023, **8**, 809.
316 S. Kim, H. Cha, R. Kostecki and G. Chen, *ACS Energy Lett.*, 2023, **8**, 521.
317 X. Liu, B. Zheng, J. Zhao, W. Zhao, Z. Liang, Y. Su, C. Xie, K. Zhou, Y. Xiang, J. Zhu, H. Wang, G. Zhong, Z. Gong, J. Huang and Y. Yang, *Adv. Energy Mater.*, 2021, **11**, 2003583.
318 H. Zhu, Z. Wang, L. Chen, Y. Hu, H. Jiang and C. Li, *Adv. Mater.*, 2023, **35**, 2209357.

319 H. Kim, Y. Kong, W. M. Seong and A. Manthiram, *ACS Appl. Mater. Interfaces*, 2023, **15**, 26585.
320 K. Yang, Y. Sun, Q. Su, Y. Lu, K. Liu, Z. Li, H. Liu and L. Zhang, *Chem. Eng. J.*, 2023, **471**, 144405.
321 C. Zhan, T. Wu, J. Lu and K. Amine, *Energy Environ. Sci.*, 2018, **11**, 243.
322 W. Li, U.-H. Kim, A. Dolocan, Y.-K. Sun and A. Manthiram, *ACS Nano*, 2017, **11**, 5853.
323 W. Li, Y. Jie, Y. Chen, M. Yang, Y. Chen, X. Li, Y. Guo, X. Meng, R. Cao and S. Jiao, *Nano Res.*, 2023, **16**, 8417.
324 M. Evertz, F. Horsthemke, J. Kasnatscheew, M. Börner, M. Winter and S. Nowak, *J. Power Sources*, 2016, **329**, 364.
325 W. Xue, M. Huang, Y. Li, Y. G. Zhu, R. Gao, X. Xiao, W. Zhang, S. Li, G. Xu, Y. Yu, P. Li, J. Lopez, D. Yu, Y. Dong, W. Fan, Z. Shi, R. Xiong, C.-J. Sun, I. Hwang, W.-K. Lee, Y. Shao-Horn, J. A. Johnson and J. Li, *Nat. Energy*, 2021, **6**, 495.
326 J. Langdon and A. Manthiram, *Adv. Mater.*, 2022, **34**, 2205188.
327 J.-Y. Hwang, S.-J. Park, C. S. Yoon and Y.-K. Sun, *Energy Environ. Sci.*, 2019, **12**, 2174.
328 H. Kim, S.-H. Lee, J.-M. Kim, C. S. Yoon and Y.-K. Sun, *ACS Energy Lett.*, 2023, **8**, 2970.
329 J. Zheng, M. H. Engelhard, D. Mei, S. Jiao, B. J. Polzin, J.-G. Zhang and W. Xu, *Nat. Energy*, 2017, **2**, 17012.
330 S. Chen, J. Zheng, L. Yu, X. Ren, M. H. Engelhard, C. Niu, H. Lee, W. Xu, J. Xiao, J. Liu and J.-G. Zhang, *Joule*, 2018, **2**, 1548.
331 X. Ren, L. Zou, X. Cao, M. H. Engelhard, W. Liu, S. D. Burton , H. Lee, C. Niu, B. E. Matthews, Z. Zhu, C. Wang, B. W. Arey, J. Xiao, J. Liu, J.-G. Zhang and W. Xu, *Joule*, 2019, **3**, 1662.
332 R. Weber, M. Genovese, A. J. Louli, S. Hames, C. Martin, I. G. Hill and J. R. Dahn, *Nat. Energy*, 2019, **4**, 683.
333 C. Niu, H. Lee, S. Chen, Q. Li, J. Du, W. Xu, J.-G. Zhang, M. S. Whittingham, J. Xiao and J. Liu, *Nat. Energy*, 2019, **4**, 551.
334 J. Liu, Z. Bao, Y. Cui, E. J. Dufek, J. B. Goodenough, P. Khalifah, Q. Li, B. Y. Liaw, P. Liu, A. Manthiram, Y. S. Meng, V. R. Subramanian, M. F. Toney, V. V. Viswanathan, M. S. Whittingham, J. Xiao, W. Xu, J. Yang, X.-Q. Yang and J.-G. Zhang, *Nat. Energy*, 2019, **4**, 180.
335 C. Fang, B. Lu, G. Pawar, M. Zhang, D. Cheng, S. Chen, M. Ceja, J.-M. Doux, H. Musrock, M. Cai, B. Liaw and Y. S. Meng, *Nat. Energy*, 2021, **6**, 987.
336 D. T. Boyle, W. Huang, H. Wang, Y. Li, H. Chen, Z. Yu, W. Zhang, Z. Bao and Y. Cui, *Nat. Energy*, 2021, **6**, 487.
337 H. Kwon, H. Kim, J. Hwang, W. Oh, Y. Roh, D. Shin and H.-T. Kim, *Nat. Energy*, 2024, **9**, 57.
338 S. C. Kim, J. Wang, R. Xu, P. Zhang, Y. Chen, Z. Huang, Y. Yang, Z. Yu, S. T. Oyakhire, W. Zhang, L. C. Greenburg, M. S. Kim, D. T. Boyle, P. Sayavong, Y. Ye, J. Qin, Z. Bao and Y. Cui, *Nat. Energy*, 2023, **8**, 814.
339 Z. Huang, J.-C. Lai, S.-L. Liao, Z. Yu, Y. Chen, W. Yu, H. Gong, X. Gao, Y. Yang, J. Qin, Y. Cui and Z. Bao, *Nat. Energy*, 2023, **8**, 577.
340 J.-Y. Hwang, S.-T. Myung, J. U. Choi, C. S. Yoon, H. Yashiro and Y.-K. Sun, *J. Mater. Chem. A*, 2017, **5**, 23671.
341 X. Liang and Y.-K. Sun, *Adv. Funct. Mater.*, 2022, **32**, 2206154.
342 T.-Y. Yu, H.-H. Ryu, G. Han and Y.-K. Sun, *Adv. Energy Mater.*, 2020, **10**, 2001609.
343 M. Sathiya, Q. Jacquet, M.-L. Doublet, O. M. Karakulina, J. Hadermann and J.-M. Tarascon, *Adv. Energy Mater.*, 2018, **8**, 1702599.
344 H.-R. Yao, W.-J. Lv, Y.-X. Yin, H. Ye, X.-W. Wu, Y. Wang, Y. Gong, Q. Li, X. Yu, L. Gu, Z. Huang and Y.-G. Guo, *ACS Appl. Mater. Interfaces*, 2019, **11**, 22067.
345 C. Xu, P. J. Reeves, Q. Jacquet and C. P. Grey, *Adv. Energy Mater.*, 2021, **11**, 2003404.
346 J.-Y. Hwang, S.-T. Myung, C. S. Yoon, S.-S. Kim, D. Aurbach and Y.-K. Sun, *Adv. Funct. Mater.*, 2016, **26**, 8083.
347 J.-Y. Hwang, S.-M. Oh, S.-T. Myung, K. Y. Chung, I. Belharouak and Y.-K. Sun, *Nat. Commun.*, 2015, **6**, 6865.
348 L. Lin, L. Zhang, S. Wang, F. Kang and B. Li, *J. Mater. Chem. A*, 2023, **11**, 7867.
349 J. Xie, A. D. Sendek, E. D. Cubuk, X. Zhang, Z. Lu, Y. Gong, T. Wu, F. Shi, W. Liu, E. J. Reed and Y. Cui, *ACS Nano*, 2017, **11**, 7019.
350 C. Delmas and I. Saadoune, *Solid State Ionics*, 1992, **53**, 370.
351 X. Liang, J.-Y. Hwang and Y.-K. Sun, *Adv. Energy Mater.*, 2023, **13**, 2301975.
352 S.-T. Myung, K. Izumi, S. Komaba, Y.-K. Sun, H. Yashiro and N. Kumagai, *Chem. Mater.*, 2005, **17**, 3695.
353 S. Jang, S.-H. Kang, K. Amine, Y. Bae and Y.-K. Sun, *Electrochim. Acta*, 2005, **50**, 4168.
354 Y. Sun, J. Han, S. Myung, S. Lee and K. Amine, *Electrochem. Commun.*, 2006, **8**, 821.
355 H.-H. Sun, J.-Y. Hwang, C. S. Yoon, A. Heller and C. B. Mullins, *ACS Nano*, 2018, **12**, 12912.
356 Y. K. Sun, M. J. Lee, C. S. Yoon, J. Hassoun, K. Amine and B. Scrosati, *Adv. Mater.*, 2012, **24**, 1192.
357 X. Liang, T.-Y. Yu, H.-H. Ryu and Y.-K. Sun, *Energy Storage Mater.*, 2022, **47**, 515.
358 Y. Wu, X. Liu, L. Wang, X. Feng, D. Ren, Y. Li, X. Rui, Y. Wang, X. Han, G.-L. Xu, H. Wang, L. Lu, X. He, K. Amine and M. Ouyang, *Energy Storage Mater.*, 2021, **37**, 77.
359 K. Edström, T. Gustafsson and J. O. Thomas, *Electrochim. Acta*, 2004, **50**, 397.
360 V. Etacheri, O. Haik, Y. Goffer, G. A. Roberts, I. C. Stefan, R. Fasching and D. Aurbach, *Langmuir*, 2012, **28**, 965.
361 Z. Zhu, Y. Tang, Z. Lv, J. Wei, Y. Zhang, R. Wang, W. Zhang, H. Xia, M. Ge and X. Chen, *Angew. Chem., Int. Ed.*, 2018, **57**, 3656.
362 J. Chen, X. Fan, Q. Li, H. Yang, M. R. Khoshi, Y. Xu, S. Hwang, L. Chen, X. Ji, C. Yang, H. He, C. Wang, E. Garfunkel, D. Su, O. Borodin and C. Wang, *Nat. Energy*, 2020, **5**, 386.
363 S.-J. Park, J.-Y. Hwang, C. S. Yoon, H.-G. Jung and Y.-K. Sun, *ACS Appl. Mater. Interfaces*, 2018, **10**, 17985.
364 Y. Lee, T. K. Lee, S. Kim, J. Lee, Y. Ahn, K. Kim, H. Ma, G. Park, S.-M. Lee, S. K. Kwak and N.-S. Choi, *Nano Energy*, 2020, **67**, 104309.
365 X. Fan, L. Chen, O. Borodin, X. Ji, J. Chen, S. Hou, T. Deng, J. Zheng, C. Yang, S.-C. Liou, K. Amine, K. Xu and C. Wang, *Nat. Nanotechnol.*, 2018, **13**, 715.

366 S. Tan, Z. Shadike, J. Li, X. Wang, Y. Yang, R. Lin, A. Cresce, J. Hu, A. Hunt, I. Waluyo, L. Ma, F. Monaco, P. Cloetens, J. Xiao, Y. Liu, X.-Q. Yang, K. Xu and E. Hu, *Nat. Energy*, 2022, **7**, 484.
367 T. Deng, X. Fan, L. Cao, J. Chen, S. Hou, X. Ji, L. Chen, S. Li, X. Zhou, E. Hu, D. Su, X.-Q. Yang and C. Wang, *Joule*, 2019, **3**, 2550.
368 B. S. Parimalam and B. L. Lucht, *J. Electrochem. Soc.*, 2018, **165**, A251.
369 J. Cha, J.-G. Han, J. Hwang, J. Cho and N.-S. Choi, *J. Power Sources*, 2017, **357**, 97.
370 J. Xiao, F. Shi, T. Glossmann, C. Burnett and Z. Liu, *Nat. Energy*, 2023, **8**, 329.
371 Y. S. Meng, V. Srinivasan and K. Xu, *Science*, 2022, **378**, 1065.